Performance relations in Capacitive Deionization systems

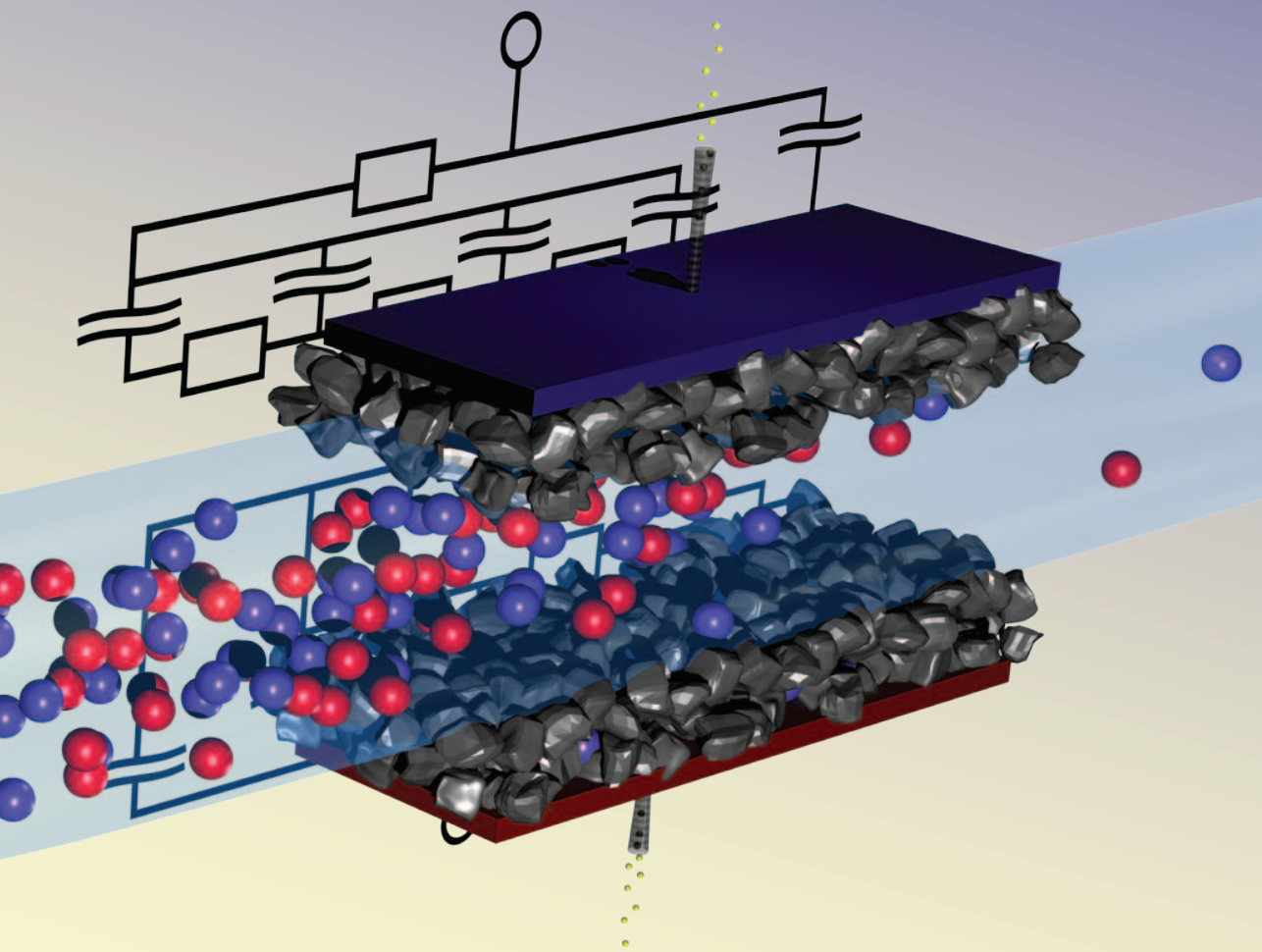

Bart van Limpt

Performance relations in Capacitive Deionization systems

Bart van Limpt

Thesis committee

Thesis supervisor
Prof. dr. ir. W.H. Rulkens
Professor of Environmental Technology
Wageningen University

Thesis co-supervisor
Dr. ir. H. Bruning
Assistant professor at the Sub-Department of Environmental Technology
Wageningen University

Other members
Prof. dr. ir. G. van Straten, Wageningen University
Prof. dr. M.A. Cohen Stuart, Wageningen University
Dr. ir. M. Saakes, Wetsus, Leeuwarden
Prof. dr. M.A. Anderson, University of Wisconsin-Madison, USA
This research was conducted under the auspices of the Graduate School SENSE (Socio-Economic and Natural Sciences of the Environment)

Performance relations in Capacitive Deionization systems

Bart van Limpt

Thesis
Submitted in fulfilment of the requirements for the degree of doctor
at Wageningen University
by the authority of the Rector Magnificus,
Prof. dr. M.J. Kropff,
in the presence of the
Thesis Committee appointed by the Academic Board
to be defended in public
on Tuesday 2 November 2010
at 4 pm in the Frisian Museum, Leeuwarden

Bart van Limpt
Performance relations in Capacitive Deionization systems
200 pages

Thesis Wageningen University, Wageningen, NL (2010)
With references, with summaries in Dutch and English

ISBN 978-90-8585-716-7

Abstract

Capacitive Deionization (CDI) is a relatively new deionization technology based on the temporary storage of ions on an electrically charged surface. By directing a flow between two oppositely charged surfaces, negatively charged ions will adsorb onto the positively charged surface, and positively charged ions will adsorb onto the negatively charged surface. To optimize CDI design for various applications, performance relations in CDI systems have to be understood. CDI performance is determined by two factors, adsorption capacity and adsorption rate. The adsorption capacity is important for performance because only a limited amount of ions can be adsorbed onto an electrically charged surface; after the total adsorption capacity is reached the surface has to be discharged. The adsorption rate is important for performance because a higher adsorption rate results in faster removal of ions from a certain stream.

The objective of this thesis is to relate the performance of a CDI unit to the specifications of the influent stream and the design aspects of the unit, such as the used electrode materials in the CDI unit. To obtain these relations, the focus in this thesis is on using electrochemical characterization techniques to obtain CDI performance in terms of charge transport, and furthermore linking this charge performance to desalination performance.

By using this approach, we found that the total adsorption capacity of a CDI unit is determined by the double-layer area present in the used electrodes, where a higher double-layer area gives a higher adsorption capacity. The adsorption capacity of the double-layer area is in turn dependent on the applied potential and the chemical and physical properties of the treated water. This analysis can be used to screen for activated carbons with a high amount of double-layer area. We found that materials with a high amount of pores with a size around 1.6 nm have a high double-layer area.

The adsorption rate of a CDI unit is mainly determined by the absolute conductivity of the influent stream. This relation can be used to optimize spacer and electrode thickness for various influent streams. The charge efficiency, i.e. the amount of ions adsorbed per amount of charge adsorbed, is limited by counter ion expulsion. It could be improved by placing ion-exchange membranes in front of the electrodes.

By integrating all obtained relations in a mathematical model, deionization performance could be predicted for CDI systems with and without ion-exchange membranes. This model can be used to predict deionization performance for any operational condition, as well as to identify and resolve bottlenecks in the operation of the CDI system.

Contents

Chapter 1

Introduction

1.1 Scope

This thesis focuses on an emerging desalination technology, called Capacitive Deionization (CDI). Capacitive Deionization is based on the temporary storage of anions (negative ions) and cations (positive ions) onto two oppositely charged surfaces, thereby removing ions from a solution.

Desalination of water is becoming more and more important as fresh water sources are becoming scarce. This was already recognized in the beginning of the 60's by the former US president John F. Kennedy:

"If we could ever competitively, at a cheap rate, get fresh water from salt water, that would be in the long-range interests of humanity and would dwarf any other scientific accomplishments"

It is now almost fifty years later, and still getting fresh water from salt water is problematic. Several examples of why dissolved salts are so problematic are described below.

Irrigation

When irrigating crops with salty irrigation water, salts build up in the soil (salination). The high salt concentration in the soil causes a reduction in the rate and amount of water that the plant roots can take up from the soil due to the difference in osmotic pressure in the plant roots and the soil. Also, some salts (especially metal salts) are toxic to plants when present in high concentrations [1].

Another negative effect of salts during irrigation is waterlogging. This condition results from an accumulation of adsorbed (exchangeable) sodium ions on exchange sites of soil minerals and organic matter, which causes the soil to disperse and become impermeable to water. This is usually caused by an excess sodium content in the irrigation water with respect to calcium and magnesium content [2].

For irrigation, a total removal of salts is not desirable; nitrate, sulfate, phosphate, and potassium are, in moderate amounts, essential for the growth of plants.

---

van Limpt, B., Bruning, H., Rulkens, W.H.

Drinking water

The total amount of salt acceptable in water for human consumption is about 500 ppm [3]. However, human tolerance is not equal for all ions. For example the human tolerance for metal ions such as cadmium, arsenic and lead is practically zero. The tolerance for ions such as fluoride, nitrate and nitrite is also limited [3].

For drinking water use, a total removal of salt is not desirable; water with a too low salt content is not healthy. When drinking this water essential salts are leached from the body, causing electrolyte imbalance.

Industry / appliances

For industry and for appliances, dissolved salts can present several problems:

- **Scaling** Under influence of pH, temperature and concentration, ions will precipitate from the solution. An example of this process is the formation of calcium carbonate deposits in washing machines and cooling towers. Scaling is also a significant problem with present deionization technologies; in most cases the produced waste streams contain calcium and magnesium above the precipitation point [4]. To prevent scaling, usually anti-scalants are added, which in turn present an additional waste problem [5].

- **Corrosion** The presence of salt in solution promotes corrosion, for example by introducing a conductive path between two types of metals (galvanic corrosion). Corrosion also occurs under a high concentration of halogen ions such as chlorine, which can penetrate passivation layers on for example stainless steel.

- **Waste water** High concentrations of salts (especially metal salts) are toxic for bacteria. Since most waste water treatment plants are based on biological processes [4], it is not allowed to discharge waste waters containing a high salt concentration into the sewer.

1.1.1 Desalination technologies

To remove salts, and in some cases specific ions, from the water, a wide range of technologies can be used. The main desalination technologies are distillation, reverse osmosis, electrodialysis and ion exchange. In a literal sense, distillation and reverse osmosis are not desalination technologies, but are “dewatering” technologies; the water is removed from a saline stream.

Distillation

With distillation, water is removed from a saline stream by evaporation. Energy is used to evaporate the water, leaving the dissolved salts behind. The evaporated water is then condensed to yield pure water, and the condensation energy can be re-used to reduce overall energy use. Commercial technologies include multi stage flash (MSF) and multi effect (ME) distillation. Distillation is relatively old and proven technology, and is used extensively in the past and in the present for large scale, high salt concentration applications, such as the production of potable water from sea water [6]. Because of the high energy use of distillation, other desalination technologies such as reverse osmosis are becoming more competitive.

Reverse osmosis

Reverse osmosis (RO) is a pressure-driven membrane separation process. High pressure is used to force a saline stream through a membrane only permeable for water, resulting in a concentrated waste stream and a very pure product stream. For separation to occur, the applied pressure has to be higher than the osmotic pressure of the saline stream. By employing pressure exchange between the influent and effluent, energy can be re-used to reduce overall energy use. RO is widely used for deionization of sea water and brackish water [5, 7].

Electrodialysis

Electrodialysis (ED) is a membrane-based separation process in which ions are driven through an ion-selective membrane under the influence of an electric field. This principle is shown in figure 1.1.

As shown in this figure, two types of membranes are used; one type only permeable for anions (anion exchange membrane), and one type only permeable for cations (cation exchange membrane). These membranes are arranged in an alternating fashion in an ED setup, and on the outside of the membrane arrangement two electrodes are placed. By applying a high potential difference over these electrodes an electric field is generated over the membranes, and charge is transported from cathode to anode. Since the ion-exchange membranes are semi-permeable, charge transport through the cation exchange membranes is due to cation transport toward the cathode, and charge transport through the anion exchange membranes is due to anion transport toward the anode. To complete the charge transport, water splitting occurs at the anode and cathode. At the anode this results in production of oxygen and H^+, and at the cathode this results in production of hydrogen and OH^-.

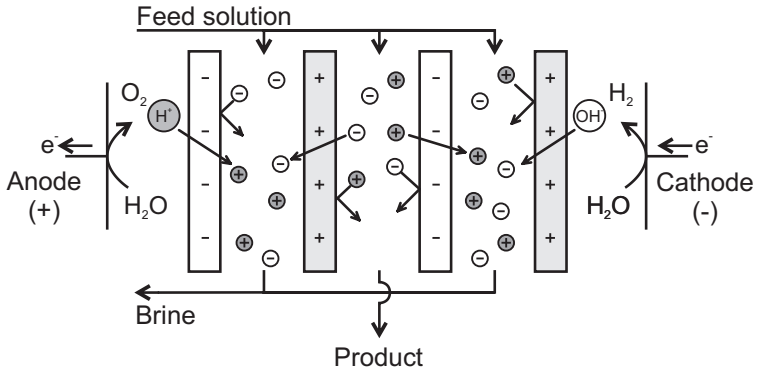

Figure 1.1: Electrodialysis principle, where a feed solution flows between alternating cation exchange (-) and anion exchange (+) membranes. Ion transport exists due to the electric field between anode and cathode. At anode and cathode, water splitting occurs to complete the transport.

Due to the alternate arrangement of the ion-exchange membranes, one compartment concentrates ions while the other compartment dilutes ions, resulting in a highly concentrated brine stream and a pure product stream.

An important application of electrodialysis is desalination of solutions with a low salt content, such as desalination of brackish ground water for use as drinking water [8]. Furthermore, electrodialysis can be integrated with other chemical processes to produce high-purity compounds [9].

Ion exchange

Ion exchange is based on the replacement of specific ions in a solution by use of an ion-exchange material. An example of this principle is shown in figure 1.2.

As shown in this figure, ion-exchange materials contain charged functional groups, in this example negative groups (shown as light circle with one negative charge) with high affinity for bivalent cations. As a counter charge to these negative groups, monovalent cations are present (shown as a dark circles with one positive charge). Due to the high affinity of the surface for bivalent cations (shown as circles with two positive charges), the monovalent cations near the surface are exchanged for bivalent cations. When all monovalent cations near the surface are exchanged for bivalent cations, the ion-exchange process stops and the ion-exchange material has to be regenerated. This regeneration can be done by immersion in a concentrated solution of monovalent cations, heat treatment, or any other method that changes the affinity of the ion-exchange material for the adsorbed ions.

Ion exchange is used to selective remove a broad range of ions from a solution,

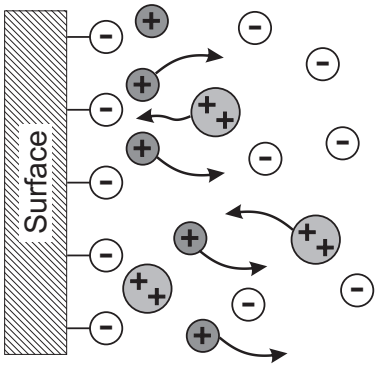

Figure 1.2: Example of the ion-exchange principle showing the surface of an ion-exchange material with fixed negative charge groups. This surface has high affinity for bivalent cations (shown as circles with two positive charges), and therefore the monovalent cations near the surface are exchanged for bivalent cations in the bulk solution

where the selectivity depends on the type of ion-exchange material, and the mode of operation. Ion exchange is mainly suitable to remove a low concentration of specific ions from a solution, and therefore used for water softening and removal of metal ions, for example in mining industry [10].

1.1.2 Technology gap

Current deionization technologies are capable of producing fresh water from salt water. Especially for large scale sea water deionization, existing RO and distillation technologies are very suitable. However, for many applications current deionization technologies are not able to produce fresh water competitively, at a cheap rate.

The main problem with current technologies is that they are only cost-effective when applied on large scale, and on water with a high salt content. However, many applications require a decentral, small scale approach where only a limited amount of salt has to be removed. One example of this approach is producing softened water for washing machines; deionization units with a small footprint are needed, since only a limited amount of space is available. Another example is producing deionized water from river water for agricultural use; to prevent transportation costs water has to be produced on site, where usually no electricity is available. This also accounts for producing drinking water from brackish ground water in rural area's.

In general, there is demand for a deionization technology with a small footprint that can cope with water with a relatively low salt content (brackish water) and can be applied in a decentral way. Capacitive Deionization is a technology that meets these demands.

1.2 Capacitive Deionization

1.2.1 Technology

Capacitive Deionization (CDI) is a desalination technology based on the temporary storage of ions onto a charged surface. This storage process takes place when two oppositely charged surfaces are inserted into a salty solution, as shown in figure 1.3. Due to the potential difference between the two surfaces, an electric field is present over the salty solution. Because of this electric field, ions are transported; cations to the negative surface (negative electrode), and anions to the positive surface (positive electrode). On the surface of the electrodes, ions are stored in a electrical double-layer. A schematic of the electrical double-layer of the negatively charged surface is shown in figure 1.4. As can be seen, due to the negative surface charge, counter-ions (in this case cations) remain close to the surface. Two layers can be distinguished (hence double-layer); cations which are present near the surface, and cations that are present together with some anions some distance away from the surface. It must be noted that the whole interface region (surface plus double-layer) remains electrically neutral.

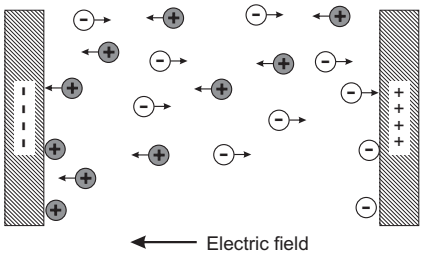

Figure 1.3: Capacitive Deionization principle showing transport of ions due to an electric field, which results from a potential difference between two oppositely charged electrodes

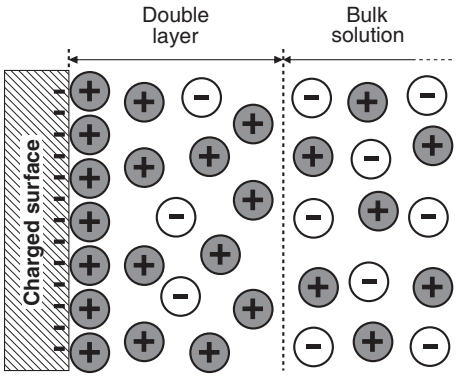

Figure 1.4: Schematic double layer showing a negatively charged surface; due to this negative surface charge, anions remain close to the surface, forming a double-layer

The storage of ions in the double-layer is reversible; when setting the potential difference between the two electrodes to zero, the surface charge is reduced due to the electrons flowing from the negative electrode to the positive electrode. Since the whole interface region has to remain electrically neutral, the stored counter-ions will migrate back into the bulk solution.

The amount of stored counter-ions in the double-layer is determined by three factors; the capacity of the double-layer, the potential drop over the double-layer, and the relation between electrical capacity and ionic capacity. Typically, the capacity of the double-layer is about 20 micro Farad per square centimeter double-layer area [11]. This means that when the potential drop over the double-layer is 1 V, 20 micro Coulombs of electrical charge can be stored per square centimeter double-layer area. The relation between charge and the amount of adsorbed counter-ions is defined by the constant of Faraday ($F = 96485\, C\ mol^{-1}$), assuming all charge is used to adsorb counter-ions. In practice, not all electrical charge is used to adsorb counter ions, for example due to electrochemical side reactions and expulsion of co-ions [12].

To maximize the amount of ions that can be stored, activated carbon electrodes are used. These electrodes are highly porous, and can contain up to 3000 m^2 surface area per gram material [11]. A significant part of this surface area can be used to generate the electrical double-layer [13, 14], and therefore to store ions. The total potential difference between the electrodes that can be used depends on the redox chemistry of the solution. When transition metal ions are present in the solution, electroplating reactions can occur where solid metal is formed on one of the electrodes. This process is commonly used for the removal of heavy metals, for example when treating waste water from a mining operation [15–18]. However, these electroplating reactions are not easily reversible and therefore deemed unwanted for CDI.

Other sources of redox reactions include carbon surface functional groups, which mostly are oxide groups [19]. These surface functional groups promote water splitting, and therefore limit the usable cell voltage to approximately 1.4 V, which means the maximal potential drop over each double-layer is 0.7 V.

The kinetics of the adsorption process is shown in figure 1.5. In the initial situation a potential difference is applied over the electrodes, but no ions have yet been adsorbed. Consequently the potential drop over the double-layers is zero, and the applied potential difference is entirely present over the solution. This results in a high electric field over the bulk solution and therefore a high adsorption rate. The adsorption of ions increases the potential drop over the double-layers, reducing the potential drop over the solution, and therefore reducing the electric field. This means that as more ions are adsorbed into the double-layers, the rate of adsorption decreases. When all potential drop is over the double-layer, the electric field becomes zero and

adsorption stops.

The kinetics of the desorption process is shown in figure 1.6. In the initial situation no potential difference is applied over the electrodes, but ions are adsorbed onto the electrodes. Consequently there exists an equal potential drop over each of the electrodes. This results in a high electric field over the solution and therefore to a high desorption rate. The desorption of ions decreases the potential drop over the double-layers, reducing the potential drop over the solution, and therefore reducing the electric field. This means that as more ions are desorbed from the double-layers, the rate of desorption decreases. When the potential drop over the double-layer becomes zero, the electric field becomes zero and desorption stops.

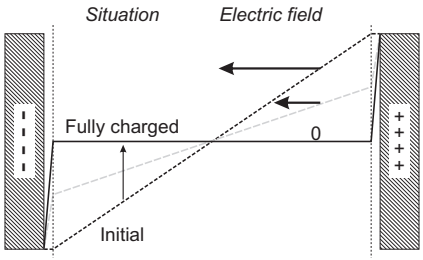

Figure 1.5: Capacitive Deionization charging kinetics showing the potential distribution as function of time on the surface of the electrodes during charging. The slope of the distribution is equal to the electric field, and the thin lines close to the electrodes depict the double-layer.

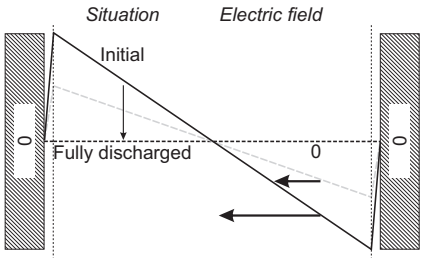

Figure 1.6: Capacitive Deionization discharging kinetics showing the potential distribution as function of time on the surface of the electrodes during charging. The slope of the distribution is equal to the electric field, and the thin lines close to the electrodes depict the double-layer.

In a practical CDI system, as shown in figure 1.7, the solution that is deionized flows between two electrodes through a spacer compartment. By charging the electrodes on each side of the spacer compartment, the saline influent is transformed into a deionized effluent. When the electrodes are fully saturated, the electrodes can be regenerated by short-circuiting the electrodes. Thereby the charge used to adsorb the ions is released, and the ions go back into the solution. The release of charge can be used to recover some of the energy put into the system, and the cycle is complete. Each cycle of the CDI process will produce a certain amount of clean water during the deionization step, and will produce a certain amount of concentrated waste stream during the regeneration step. The ratio between both streams is dependent on the capacity of the used carbon materials, and on the salt concentration in the influent.

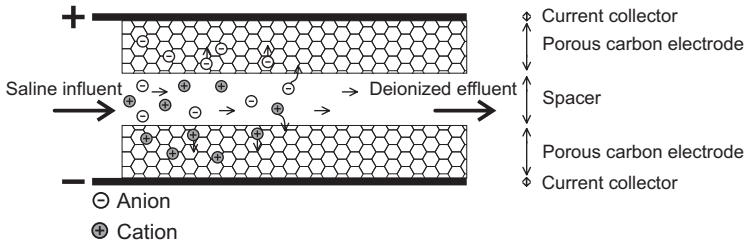

Figure 1.7: Schematic practical implementation of CDI principle, where a saline solution passes through a spacer. During transition, the ions in the solution are adsorbed onto the electrodes and a deionized effluent is obtained. Current collectors connect the electrodes to a power supply.

1.2.2 Development

CDI technology has its roots in supercapacitor technology. A supercapacitor is based on the same principle as CDI; two high surface area carbon electrodes are separated by a thin spacer, and immersed in an electrolyte solution [20]. The difference between CDI and supercapacitors is that for supercapacitors the amount of charge stored on the electrodes is of importance, not the amount of removed ions. Therefore with supercapacitors a stationary electrolyte is used, while with CDI the electrolyte flows between the electrodes. Supercapacitors are capable of storing large amounts of energy, which can be retrieved at a high rate during discharge. An application of supercapacitors is in (electric) cars to re-use braking energy, for example in the kinetic energy recovery system (KERS) in Formula 1 cars. Other applications include mobile phones, toys and flash devices in digital camera's.

There are many parallels between the development of supercapacitors and CDI. The first supercapacitors [21] used electrodes constructed from carbon powder. A very similar construction was used in the initial demonstrations of CDI in the 60's through 80's, then called "electrochemical parametric pumping" [22–26]. In these initial demonstrations, desalination was performed by passing a saline solution through two packed beds of carbon powder. By applying a potential difference over the two packed beds the saline solution could be deionized. Although the design of packed beds was highly successful for supercapacitors, it did not work well for CDI. The reason is that with CDI the electrolyte has to flow through the packed beds. This means that compression of these packed beds has to be low to allow for the flow of electrolyte, resulting in high contact resistance between the carbon particles, and consequently a slow deionization process. Another problem was that carbon was depleted from the packed bed electrodes due to the flow of solution through the electrodes.

To overcome the problems of packed bed electrodes, the attention moved to al-

ternate designs of the CDI system, and to the use of different electrode materials, mostly done in response to materials developed for supercapacitors. In the early 90's supercapacitors were developed at the Lawrence Livermore National Laboratory based on carbon aerogel, called "aerocapacitors" [13, 27]. Carbon aerogel is a solid porous carbon material, which exhibits low electrical resistance, and is produced by impregnating a carbon paper support with resorcinol and formaldehyde, which is polymerized. The resulting structure is heat treated to carbonize the structure, and to generate microporosity [28]. Due to the low electrical resistance and high microporosity carbon aerogel is ideal to use as an electrode for CDI.

In the late 90's researchers at Lawrence Livermore National Laboratory [17, 29, 30] applied carbon aerogel electrodes to deionize water. The carbon aerogel electrodes solved the problems of carbon depletion and electrical contact due to their high strength and low internal resistance. These electrodes were glued to titanium supports to form parallel electrodes, as shown figure 1.8. Several groups picked up this technology and applied the electrodes on various waste waters [31–36].

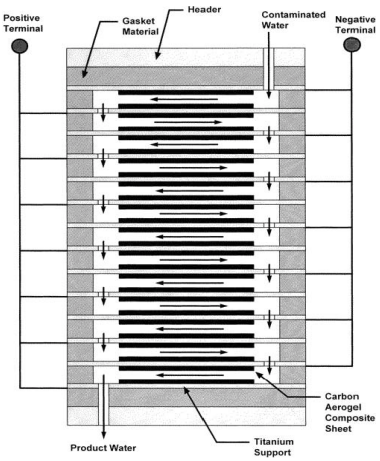

Figure 1.8: Schematic representation of carbon aerogel CDI setup, reprinted from [29]

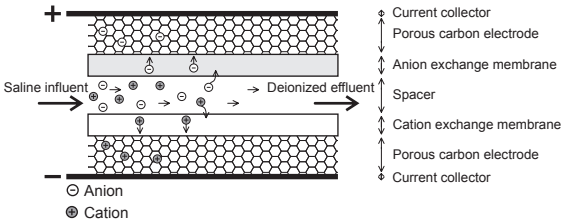

Figure 1.9: Schematic representation of membrane-assisted CDI (MCDI)

The disadvantage of the use of carbon aerogel is its costs, the precursor resorcinol and formaldehyde are expensive as compared to normal activated carbons, which are generally made from cheap materials such as coconut shells [11]. Furthermore, the used titanium supports are very costly.

In response of the development of new materials for use in supercapacitors [37, 38], these materials were also used in the application of CDI. These include the use of carbon powders in a polymer matrix [39–42], the use of carbon fiber materials [43–

45], and carbon nanotubes and nanofibers [46, 47].

Besides development of the electrode material, there has also been much attention on changing the design of CDI. One of the most recent developments is to use ion-exchange membranes to improve the performance of CDI [48], called membrane-assisted CDI (MCDI). Figure 1.9 shows the principle of MCDI. Ion-exchange membranes are placed in front of the electrodes; an anion-selective membrane in front of the positive electrode, and a cation-selective membrane in front of the negative electrode. The use of ion-exchange membranes enhances performance of the deionization process [47, 49] and prevents carbon depletion, since the flow no longer goes through or near the electrodes. Other implementations of ion-exchange membranes enable continuous deionization [50]. It is interesting to note that in one of the very first demonstrations of CDI already ion-exchange membranes were used [22]. One disadvantage of MCDI over normal CDI is the costs of the ion-exchange membranes. However, this can be compensated by the fact that cheaper, powder based electrodes can be used; the membranes physically isolate the electrodes, therefore electrode depletion is no longer an issue.

Applications of CDI that have been studied were mainly on the deionization of sodium chloride solutions, however research has also been done on the removal of other ions with CDI, such as removal of nitrates [30, 43], sulfur containing ions [51], and various other ions [29–31, 40, 52]. Other research applications of CDI include RO brine recovery [49] and treatment of brackish water [34, 53].

1.3 Comparison CDI to Reverse Osmosis and Electrodialysis

1.3.1 Energy use

The energy use of CDI can be split in two contributing terms. The first term is the thermodynamic energy difference between the ingoing stream and the outgoing concentrate and diluate stream, which is equal to the Gibbs free energy of mixing ΔG [54] [a]. When the solution consists of a binary salt dissolved in water, it can be written as in equation (1.1).

$$\Delta G = 2\left[c_w V_w RT \ln\left(\gamma_w x_w\right) + c_{eff} V_{eff} RT \ln\left(\gamma_{eff} x_{eff}\right) - c_{in} V_{in} RT \ln\left(\gamma_{in} x_{in}\right)\right] \tag{1.1}$$

[a] The mixing energy between sweet and saline water is the energy source for reversed electrodialysis, an energy generation technology

In this equation, the subscripts w, eff and in refer to respectively waste, deionized effluent and influent solution, c is the concentration of the binary salt in mol L^{-1}, V is the volume of the respective solution in L, x is the mole fraction of the binary salt in the respective solution, and γ is the activity of the binary salt in the respective solution.

When producing potable water (assuming 0.005 M NaCl) from sea water (assuming 0.5 M NaCl), where the waste stream has a concentration of 5 M NaCl (close to the maximum solubility of NaCl), ΔG is 1.66 kWh per m^{-3} produced water at $T = 293.15\ K$.

The second term contributing to the energy use is due to the charging of the double-layer. In this case, the energy use is related to the amount of electrons needed to remove a certain amount of ions. When considering the double-layers on the electrodes as one single capacitor [55], the charge Q, in C, needed to remove a certain amount of salt is expressed according to equation (1.2)[b].

$$Q = (c_{in} - c_{eff})\, V_{in} F \tag{1.2}$$

Assuming no leak processes such as redox reactions take place, and that all applied charge is used to store ions, the energy needed to deionize the solution $U_{in,max}$ is expressed as equation (1.3).

$$U_{in,max} = Q E_{cell} \tag{1.3}$$

In this equation, E_{cell} is the applied voltage over the electrodes in V (the cell voltage). When deionizing sea water (again assuming 0.5 M NaCl), $U_{in,max}$ is equal to 16.1 $kWh\ m^{-3}$ produced potable water at a cell voltage of 1.4 V.

When discharging the electrodes, part of the applied energy can be recovered. However, not all energy can be recovered, due to the Gibbs energy of mixing ΔG, and because part of the applied energy is dissipated to heat.

The amount of applied energy dissipated to heat depends on the way the electrodes are charged. Usually a constant cell voltage is used to charge the electrodes, since this way a maximum electric field is generated that results in fast deionization kinetics. When using a constant cell voltage, the amount of dissipated heat can be obtained by considering the energy stored on the electrodes during charging at constant cell voltage, according to equation (1.4).

$$dU_s = E_C dq = \frac{q}{C} dq \tag{1.4}$$

[b]The capacity of the double-layer is not constant but dependent on potential, salt concentration and temperature

In this equation, dU_s is the change in stored energy on the electrodes in J, E_C is the potential over the electrodes, dq is the change in charge of the electrodes in C, and C is the capacity of the electrodes in F. When assuming C to remain constant with increasing cell voltage, the stored energy can be obtained when integrating equation (1.4), as shown in equation (1.5).

$$dU_s = \int_0^Q \frac{q}{C} dq = \frac{1}{2} \frac{Q^2}{C} = \frac{1}{2} Q E_{cell} \tag{1.5}$$

As results from equation (1.5), when applying a constant cell voltage E_{cell}, the stored energy in the electrodes is half of the applied energy. Therefore during regeneration, in the most optimal situation, only half of the applied energy can be re-used. This makes the minimum energy use, at constant cell voltage, according to equation (1.6).

$$U_{in,min} = \frac{1}{2} Q E_{cell} + \Delta G \tag{1.6}$$

When deionizing sea water (again assuming 0.5 M NaCl), $U_{in,min}$ is 9 $kWh\ m^{-3}$ produced potable water at a cell voltage of 1.4 V.

To reduce the energy use, the electrodes can be charged by very slowly increasing the applied cell voltage. This way, the voltage over the capacitor is always close to the applied voltage, resulting in an average applied cell voltage of 0.5 E_{cell}. This means no energy is dissipated to heat, but the charging process is infinitely slow. In general applications, this is not desirable. Therefore $U_{in,min}$ is considered as the minimum energy needed.

Figure 1.10 shows the comparison of the theoretical energy use for CDI with the energy use of ED and RO. In this figure, data are from state-of-the-art results of ED, RO, and CDI systems [4, 5, 7, 8, 34, 56–59]. In the graph, ΔG is obtained by assuming production of 1 m^3 potable water with a concentration of 0.005 M NaCl, where the waste stream contains 5 M NaCl. The line labeled "No energy reuse" relates to $U_{in,max}$, and the line labeled "Energy reuse" relates to $U_{in,min}$. Both lines were calculated at a cell voltage E_{cell} of 1.4 V. The RO systems in the light gray area are large scale systems and employ energy recovery systems such as pressure exchangers. These are only fully applicable for large scale RO systems; the dark gray area shows the energy use for small scale RO systems which show a significantly higher energy use [7, 58].

As shown in figure 1.10, for concentrations below 0.1 M the energy use of CDI is equal or lower to RO and ED systems. For bulk sea water desalination ($c \approx 0.5\ M$), CDI does not seem a viable alternative to RO due to the high energy use. As shown in the graph, little literature data is present on actual energy use of CDI, the included

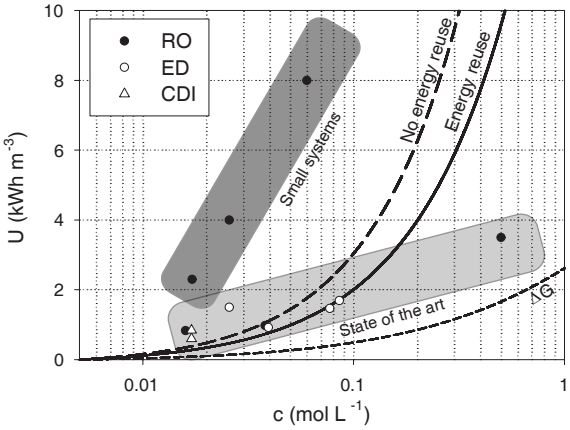

Figure 1.10: Comparison CDI to RO and ED in terms of energy use U per cubic meter produced clean water, based on water with a certain NaCl concentration c. Light gray area relates to large RO systems, dark gray area relates to small RO systems. Dots correspond to reported values from literature, lines correspond to theoretical energy use for CDI for three scenario's

points are two estimates for treating a concentration of 0.017 M NaCl [34, 59]. In both cases, no energy reuse was employed, and the obtained energy results are close to the theoretical values.

1.3.2 Other advantages of CDI over current technologies

Besides having a favorable energy use for small scale brackish water deionization, there are several other advantages for CDI over RO and ED technology. Below are some disadvantages on present deionization technologies [4, 5, 7, 9, 60] that are not an issue or less of an issue for CDI.

Biofouling and scaling

RO is very susceptible to both biofouling (biological growth) and scaling (precipitation of salts). For ED, biofouling is less of an issue, but calcium scaling is a serious problem and most ED systems cannot handle streams with a high calcium content, due to local high pH values. To prevent biofouling and scaling in RO and ED, chemicals are added that in turn end up in the waste stream.

CDI is less susceptible for scaling, since during regeneration the ions are recombined in the spacer compartment. By flushing the spacer compartment during regeneration precipitation can be prevented. Biofouling is also less of a problem, the surface charge on the electrodes will inhibit biological growth [61]. Furthermore, since

regeneration is performed in the same channel as deionization, biology will experience a significant osmotic shock when regenerating. If biofouling does occur, an overpotential can be applied on the electrodes to produce hypochloride, that will eliminate most of the bacteria [62, 63].

Effluent and waste quality

With RO, the salt content of the deionized effluent generally is extremely low, making it corrosive, unpalatable and unhealthy. Therefore the effluent has to be hardened. With CDI and ED this is not the case, the deionized effluent quality can be controlled.

A feature of both CDI and ED is that both technologies do not remove uncharged compounds, these are retained in the deionized effluent. This means that it might be necessary to include an additional pre- or post-treatment to remove these compounds. This also relates to scaling, with CDI crystallization nuclei that are formed due to supersaturation will not be removed from the water. Therefore scaling will not occur in the reactor, but in the waste solution that leaves the system. When including a settling tank, part of the waste could potentially be removed as solids.

Water recovery

Water recovery relates to the percentage of influent that is deionized. RO has a relatively low water recovery, which is 75-80 % for brackish water treatment and 35-60 % for sea water treatment. Higher recovery is possible, but at a much higher energy use. The water recovery for ED can reach up to 90 % [64] for brackish water treatment. For CDI, water recoveries for brackish water treatment were relatively low (< 70 %) in the past [59] but nowadays water recoveries of 90 % are possible [65, 66].

Capital costs

Capital costs for RO and ED are high, RO systems use expensive pressure exchangers and pumps, while for ED expensive membranes and electrodes are used.

With CDI, capital costs are mainly the electrodes costs. Since CDI is moving from the expensive carbon aerogel electrodes to cheaper carbon fiber and carbon powder electrodes, this is expected to be dramatically reduced. Other important capital costs are the electronics, a low potential direct current is needed at a very high amperage. To handle these high amperes without electric loss, expensive low resistance wiring has to be used. The recent use of ion-exchange membranes in CDI, (MCDI) does present an additional capital costs in the form of the ion-exchange membranes.

1.4 Objective and outline of the thesis

To further determine the applicability of CDI for deionization, the performance relations of the process have to be better understood. These performance relations are relatively complex; accumulation of charge on two parallel electrodes is coupled to the removal of ions from the electrolyte between these two electrodes. The focus of present literature has mainly been on the deionization a certain waste stream, and performance only related to electrode properties such as BET [36, 67] and physical salt adsorption capacity [29–31, 33, 40]. Some works exist on the modeling on CDI kinetics [12, 23]. However, these works rely on unvalidated theoretical models.

The objective of this thesis is to relate the performance of a CDI unit to the design of the unit and the specifications of the influent stream. This relationship can be used to define performance parameters for each of the elements in the CDI unit. These performance parameters can in turn be used to optimize the CDI unit for a specific purpose.

Chapter 2 of this thesis discusses the selection of an electrochemical method to characterize materials for use in CDI. The approach used is to regard CDI not in terms of salt removal, but in terms of charge storage. This is done by considering the CDI system as a supercapacitor. The kinetics of a supercapacitor system are determined by the electrical capacity, or the maximum amount of charge that can be built up, plus the electrical resistance, or the rate at which the capacitor can be charged and discharged. For determining these kinetics, electrochemical characterization techniques are used [24, 37, 38, 43, 68, 69] such as electrochemical impedance spectroscopy, cyclic chronopotentiometry, and voltammetry.

The constructed characterization method can then be used to investigate the mechanisms behind the kinetics of charge storage in a CDI unit. This is done by relating characterization results to operational parameters (temperature, electrolyte concentration and cell voltage). Using these relations, in **chapter 3** capacity measurements are linked to a double-layer model describing the adsorption of ions onto a charged surface. This results in a performance parameter that relates to the maximum amount of charge that can be stored on a certain electrode, independent of the operational parameters.

In **chapter 4**, a similar approach is used to link resistance measurements to the design of the cell and the characteristics of the electrolyte. This results in performance parameters that relate to the rate at which the CDI unit can be charged and discharged, independent of the operational and design parameters.

In **chapter 5** the performance parameters in terms of charge are further investigated as function of electrode construction. This is done since in literature many

different types of electrodes are used, and the developed approach has to be as general as possible. Therefore electrodes were investigated of different carbon type, thickness, and surface area characteristics. The obtained relations are also used to validate the results of the previous chapters.

Since electrochemical performance in terms of resistance and capacitance does not necessarily mean that the performance in terms of salt removal and salt capacity is the same, in **chapter 6** the link between salt removal and charge storage is investigated. The link is made by inclusion of efficiency parameters. The dependency of these efficiency parameters on cell voltage is also investigated, as well as the use of ion-exchange membranes to improve these parameters.

To verify that the obtained relations are valid for different kinds of ions, in **chapter 7** the effect of various ion species on performance is investigated. This is done by comparing deionization performance of a broad range of salts to the deionization performance of a standard solution.

To validate the integrated approach developed in chapters 2 through 6, in **chapter 8** all obtained relationships are combined into a mass and charge transport model of CDI. Several experimental CDI runs are compared with the model, to investigate the strengths and weaknesses of the model. Furthermore, the model is used to validate simplifications done throughout the thesis, as well as predicting several aspects in the kinetics of CDI such as transmission line kinetics and dead time.

Finally, in **chapter 9** general conclusions are presented, and the various results found throughout the thesis are discussed.

Bibliography

[1] R. Pichu. World salinization with emphasis on Australia. *Journal of Experimental Botany*, 57(5):1017–1023, 2006.

[2] D. Yaron. *Salinity in irrigation and water resources.* CRC, 1981.

[3] US EPA. National primary drinking water regulations, May 2009.

[4] L. F. Lawler D. F. Freeman B. D. Marrot B. Moulin P. Greenlee. Reverse osmosis desalination: Water sources, technology, and today's challenges. *Water Research*, 43(9):2317–2348, 2009.

[5] C. Löwenberg J. Wintgens T. Melin T. Fritzmann. State-of-the-art of reverse osmosis desalination. *Desalination*, 216(1-3):1–76, 2007.

[6] B. Tleimat and M. Tleimat. Developments in saline water distillation technology. *Desalination*, 93(1-3):15–42, 1993.

[7] M.A. Alghoul, P. Poovanaesvaran, K. Sopian, and M.Y. Sulaiman. Review of brackish water reverse osmosis (BWRO) system designs. *Renewable and Sustainable Energy Reviews*, 13(9):2661–2667, 2009.

[8] J.M. Ortiz, E. Expósito, F. Gallud, V. García-García, V. Montiel, and A. Aldaz. Desalination of underground brackish waters using an electrodialysis system powered directly by photovoltaic energy. *Solar Energy Materials and Solar Cells*, 92(12):1677–1688, 2008.

[9] C. Huang and T. Xu. Electrodialysis-based separation technologies: A critical review. *AIChE Journal*, 54(12):3147–3159, 2008.

[10] A. Zagorodni. *Ion exchange materials: properties and applications.* Elsevier, November 2006.

[11] K. Kinoshita. *Carbon, Electrochemical and physicochemical properties.* Wiley Interscience, New York, 1st edition, 1987.

[12] P. M. Biesheuvel, B. van Limpt, and A. van der Wal. Dynamic adsorption/desorption process model for capacitive deionization. *The Journal of Physical Chemistry C*, 113(14):5636–5640, 2009.

[13] R. Saliger, U. Fischer, and C. Herta. High surface area carbon aerogels for supercapacitors. *Journal of Non-Crystalline Solids*, 225(1):81–85, 1998.

[14] M. Toupin, D. Belanger, and I. R. Hill. Performance of experimental carbon blacks in aqueous supercapacitors. *Journal of Power Sources*, 140(1):203–210, 2005.

[15] A. Afkhami and B. E. Conway. Investigation of removal of Cr(VI), Mo(VI), W(VI), V(IV), and V(V) oxy-ions from industrial waste-waters by adsorption and electrosorption at high-area carbon cloth. *Journal of Colloid And Interface Science*, 251(2):248–255, 2002.

[16] A. Brennsteiner, J. W. Zondlo, A. H. Stiller, P. G. Stansberry, D. C. Tian, and Y. Xu. Environmental pollution control devices based on novel forms of carbon: Heavy metals. *Energy & Fuels*, 11(2):348–353, 1997.

[17] J. C. Farmer, S. M. Bahowick, J. E. Harrar, D. V. Fix, R. E. Martinelli, A. K. Vu, and K. L. Carroll. Electrosorption of chromium ions on carbon aerogel electrodes as a means of remediating ground water. *Energy & Fuels*, 11(2):337–347, 1997.

[18] M. M. Goldin, A. G. Volkov, and D. N. Namychkin. Adsorption of copper, silver, and zinc cations on polarized activated carbons. *Journal of the Electrochemical Society*, 152(5):E167–E171, 2005.

[19] H. P. Boehm. Some aspects of the surface-chemistry of carbon-blacks and other carbons. *Carbon*, 32(5):759–769, 1994.

[20] B. E. Conway. *Electrochemical Supercapacitors, Scientific Funcamentals and Technological Applications.* Kluwer Academic / Plenum Publishers, New York, 1st edition, 1999.

[21] H. E. Becker. U.S. patent 2 800 616, 1957.

[22] B. B. Arnold and G. W. Murphy. Studies on electrochemistry of carbon and chemically modified carbon surfaces. *Journal of Physical Chemistry*, 65(1):135–138, 1961.

[23] A. M. Johnson and J. Newman. Desalting by means of porous carbon electrodes. *Journal of the Electrochemical Society*, 118(3):510–&, 1971.

[24] Y. Oren and A. Soffer. Electrochemical parametric pumping. *Journal of the Electrochemical Society*, 125(6):869–875, 1978.

[25] Y. Oren and A. Soffer. Water desalting by means of electrochemical parametric pumping .1. The equilibrium properties of a batch unit-cell. *Journal of Applied Electrochemistry*, 13(4):473–487, 1983.

[26] Y. Oren and A. Soffer. Water desalting by means of electrochemical parametric pumping .2. Separation properties of a multistage column. *Journal of Applied Electrochemistry*, 13(4):489–505, 1983.

[27] S. T. Mayer, R. W. Pekala, and J. L. Kaschmitter. The aerocapacitor - an electrochemical double-layer energy-storage device. *Journal of the Electrochemical Society*, 140(2):446–451, 1993.

[28] S. W. Hwang and S. H. Hyun. Capacitance control of carbon aerogel electrodes. *Journal of Non-Crystalline Solids*, 347(1-3):238–245, 2004.

[29] J. C. Farmer, D. V. Fix, and G. V. Mack. Capacitive deionization of NaCl and $NaNO_3$ solutions with carbon aerogel electrodes. *Journal of the Electrochemical Society*, 143(1):159–169, 1996.

[30] J. C. Farmer, D. V. Fix, and G. V. Mack. Capacitive deionization of NH_4ClO_4 solutions with carbon aerogel electrodes. *Journal of Applied Electrochemistry*, 26(10):1007–1018, 1996.

[31] C. J. Gabelich, T. D. Tran, and I. H. Suffet. Electrosorption of inorganic salts from aqueous solution using carbon aerogels. *Environmental Science & Technology*, 36(13):3010–3019, 2002.

[32] H. H. Jung, S. W. Hwang, and S. H. Hyun. Capacitive deionization characteristics of nanostructured carbon aerogel electrodes synthesized via ambient drying. *Desalination*, 216(1-3):377, 2007.

[33] P. Rana-Madaria, M. Nagarajan, C. Rajagopal, and B. S. Garg. Removal of chromium from aqueous solutions by treatment with carbon aerogel electrodes using response surface methodology. *Industrial & Engineering Chemistry Research*, 44(17):6549–6559, 2005.

[34] P. Xu, J. E. Drewes, and D. Heil. Treatment of brackish produced water using carbon aerogel-based capacitive deionization technology. *Water Research*, 42(10-11):2605, 2008.

[35] C. M. Yang, W. H. Choi, and B. K. Na. Capacitive deionization of NaCl solution with carbon aerogel-silica gel composite electrodes. *Desalination*, 174(2):125–133, 2005.

[36] T. Y. Ying, K. L. Yang, S. Yiacoumi, and C. Tsouris. Electrosorption of ions from aqueous solutions by nanostructured carbon aerogel. *Journal of Colloid and Interface Science*, 250(1):18–27, 2002.

[37] E. Frackowiak and F. Beguin. Carbon materials for the electrochemical storage of energy in capacitors. *Carbon*, 39(6):937–950, 2001.

[38] C. Kim. Electrochemical characterization of electrospun activated carbon nanofibres as an electrode in supercapacitors. *Journal of Power Sources*, 142(1-2):382–388, 2005.

[39] M. D. Andelman. The flow through capacitor: A new tool in wastewater purification. *Filtration & Separation*, 35(4):345–347, 1998.

[40] H. Oda and Y. Nakagawa. Removal of ionic substances from dilute solution using activated carbon electrodes. *Carbon*, 41(5):1037–1047, 2003.

[41] J. A. Lim, N. S. Park, J. S. Park, and J. H. Choi. Fabrication and characterization of a porous carbon electrode for desalination of brackish water. *Desalination*, 238(1-3):37–42, 2009.

[42] K. K. Park, J. B. Lee, P. Y. Park, S. W. Yoon, J. S. Moon, H. M. Eum, and C. W. Lee. Development of a carbon sheet electrode for electrosorption desalination. *Desalination*, 206(1-3):86, 2007.

[43] A. Afkhami. Adsorption and electrosorption of nitrate and nitrite on high-area carbon cloth: an approach to purification of water and waste-water samples. *Carbon*, 41(6):1320–1322, 2003.

[44] H. J. Oh, J. H. Lee, H. J. Ahn, Y. Jeong, Y. J. Kim, and C. S. Chi. Nanoporous activated carbon cloth for capacitive deionization of aqueous solution. *Thin Solid Films*, 515(1):220–225, 2006.

[45] M. W. Ryoo, J. H. Kim, and G. Seo. Role of titania incorporated on activated carbon cloth for capacitive deionization of NaCl solution. *Journal of Colloid and Interface Science*, 264(2):414–419, 2003.

[46] X. Z. Wang, M. G. Li, Y. W. Chen, R. M. Cheng, S. M. Huang, L. K. Pan, and Z. Sun. Electrosorption of NaCl solutions with carbon nanotubes and nanofibers composite film electrodes. *Electrochemical and Solid-State Letters*, 9(9):E23–E26, 2006.

[47] H. Li, Y. Gao, L. Pan, Y. Zhang, Y. Chen, and Z. Sun. Electrosorptive desalination by carbon nanotubes and nanofibres electrodes and ion-exchange membranes. *Water Research*, 42(20):4923–4928, 2008.

[48] M. D. Andelman. U.S. patent US 2004/0174657 A1, 2004.

[49] J. B. Lee, K. K. Park, H. M. Eum, and C. W. Lee. Desalination of a thermal power plant wastewater by membrane capacitive deionization. *Desalination*, 196(1-3):125–134, 2006.

[50] K. Dermentzis and K. Ouzounis. Continuous capacitive deionization-electrodialysis reversal through electrostatic shielding for desalination and deionization of water. *Electrochimica Acta*, 53(24):7123–7130, 2008.

[51] E. Ayranci and B. E. Conway. Adsorption and electrosorption at high-area carbon-felt electrodes for waste-water purification: Systems evaluation with inorganic, S-containing anions. *Journal of Applied Electrochemistry*, 31(3):257–266, 2001.

[52] A. Ban, A. Schafer, and H. Wendt. Fundamentals of electrosorption on activated carbon for wastewater treatment of industrial effluents. *Journal of Applied Electrochemistry*, 28(3):227–236, 1998.

[53] L. Zou, L. Li, H. Song, and G. Morris. Using mesoporous carbon electrodes for brackish water desalination. *Water Research*, 42(8-9):2340–2348, 2008.

[54] J. W. Post, J. Veerman, H. V. M. Hamelers, G. J. W. Euverink, S. J. Metz, K. Nymeijer, and C. J. N. Buisman. Salinity-gradient power: Evaluation of pressure-retarded osmosis and reverse electrodialysis. *Journal of Membrane Science*, 288(1-2):218–230, 2007.

[55] J. Newman and K. E. Thomas-Alyea. *Electrochemical Systems*. John Wiley & Sons, Hoboken, 3rd edition, 2004.

[56] G.K. Pearce. UF/MF pre-treatment to RO in seawater and wastewater reuse applications: a comparison of energy costs. *Desalination*, 222(1-3):66–73, 2008.

[57] A. Stikker. Desal technology can help quench the world's thirst. *Water Policy*, 4(1):47–55, 2002.

[58] G. Papadakis, E. SH. Mohamed, and D. Manolakos. *Solar Desalination for the 21st Century*, chapter Small Autonomous RO Desalination Systems Powered by Renewable Energies, Technological Advances and Economics, pages 293–303. NATO Security through Science Series. Springer, 2007.

[59] T. J. Welgemoed and C. F. Schutte. Capacitive delonization technology (TM) : An alternative desalination solution. *Desalination*, 183(1-3):327–340, 2005.

[60] M. S. Mohsen and O. R. Al-Jayyousi. Brackish water desalination: an alternative for water supply enhancement in jordan. *Desalination*, 124(1-3):163–174, 1999.

[61] T. Matsunaga, S. Nakasono, Y. Kitajima, and K. Horiguchi. Electrochemical disinfection of bacteria in drinking-water using activated carbon-fibers. *Biotechnology And Bioengineering*, 43(5):429–433, 1994.

[62] G. Patermarakis and E. Fountoukidis. Disinfection of water by electrochemical treatment. *Water Research*, 24(12):1491–1496, 1990.

[63] A. Kraft, M. Stadelmann, M. Blaschke, D. Kreysig, B. Sandt, F. Schroder, and J. Rennau. Electrochemical water disinfection - part i: Hypochlorite production from very dilute chloride solutions. *Journal of Applied Electrochemistry*, 29(7):861–868, 1999.

[64] M. Turek. Dual-purpose desalination-salt production electrodialysis. *Desalination*, 153(1-3):377–381, 2003.

[65] L. Y. Lee, S. L. Ong, G. Tao, B. Viawanath, K. Kekre, W. Lay, H. Y. Ng, and H. Seah. Treatment of RO brine–towards sustainable water reclamation practice. *Water Science & Technology*, 58(4):931–936, 2008.

[66] Y. Oren. Capacitive deionization (CDI) for desalination and water treatment – past, present and future (a review). *Desalination*, 228(1-3):10, 2008.

[67] K. L. Yang, T. Y. Ying, and S. Yiacoumi. Electrosorption of ions from aqueous solutions by carbon aerogel: An electrical double-layer model. *Langmuir*, 17(6):1961–1969, 2001.

[68] J. Gamby, P. L. Taberna, P. Simon, J. F. Fauvarque, and M. Chesneau. Studies and characterisations of various activated carbons used for carbon/carbon supercapacitors. *Journal of Power Sources*, 101(1):109–116, 2001.

[69] K. L. Yang, S. Yiacoumi, and C. Tsouris. Electrosorption capacitance of nanostructured carbon aerogel obtained by cyclic voltammetry. *Journal of Electroanalytical Chemistry*, 540:159–167, 2003.

Chapter 2

Electrode characterization with Electrochemical Impedance Spectroscopy (EIS)

2.1 Summary

Electrochemical impedance spectroscopy (EIS) was investigated as a method to characterize electrode materials for use in Capacitive Deionization (CDI). Three different electrode materials were investigated, carbon powders, carbon fibers and carbon aerogel. Characterization results were validated using potentiometry experiments. The difference between the three electrode materials is the ion transport into the electrodes; for carbon powders electrodes the ion transport is according to ideal linear De Levie transmission line behavior, for carbon aerogel electrodes the ion transport is according to a constant phase angle (CPA) transmission line behavior. For carbon fiber electrodes, the description of ion transport deviated from models in literature. Therefore a new transmission line model was developed based on a power law distribution of resistance over capacitance. This model has an extra parameter that describes the distribution of resistance over capacitance, and was successfully applied to model the ion transport in carbon fiber electrodes.

2.2 Introduction

Capacitive Deionization (CDI) is based on the principle of ion adsorption onto the surface of a porous carbon electrode. A representation of this process is shown in figure 2.1. This figure shows a typical CDI electrode arrangement in an electrolyte solution, consisting of two carbon electrodes separated by a porous spacer, and connected to a potentiostat (power supply) by a current collector. The carbon electrode can be constructed out of different types of carbon, such as powders (mostly a composite with polymers) [1–3], fibers [4–6], nanotubes [7], and aerogel [8–14]. The spacer is electrically insulating to prevent short-circuit, but also porous to enable ion transport.

The ion adsorption process starts by applying a potential difference between the two carbon electrodes, forming an electrical field between the electrodes. Therefore, anions move toward the positive electrode and cations toward the negative electrode,

van Limpt, B., Bruning, H., Saakes, M., Rulkens, W.H.

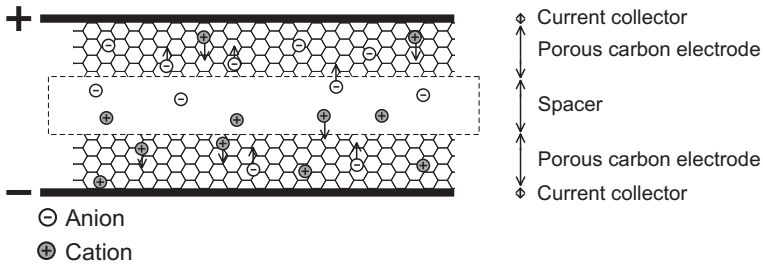

Figure 2.1: Representation of ion adsorption process into a porous carbon electrode

where they are stored onto the carbon surface. The build up of ions on the surface of the electrodes introduces a surface charge that reduces the potential difference between the two carbon electrodes. Eventually, the surface charge fully compensates the potential difference between the two carbon electrodes and adsorption stops.

To select the best carbon electrode material for CDI application, a method is needed to characterize potentially interesting carbon electrode materials. In this characterization, two aspects are of importance, the maximum amount of ions that can be adsorbed per unit carbon electrode, and the rate at which these ions can be adsorbed.

In current literature, characteristics of the carbon electrode materials for CDI application are usually only described in terms of surface area such as BET [14, 15] and in physical salt adsorption capacity [2, 9, 11, 16, 17]. However, these characteristics only relate to the maximum amount of ions that can be adsorbed per unit carbon electrode, and do not give an indication of the rate of adsorption.

Another approach of describing the characteristics of CDI electrodes is investigating the electrical charge that is build up, instead of the salt that is adsorbed. This way, it is considered that a CDI electrode arrangement is equal to a double-layer capacitor, or supercapacitor, arrangement. Supercapacitors are capacitors that can store a relatively high amount of electrical charge in a small volume ($> 10\ F\ cm^{-3}$) and are based on the same principle as CDI, the adsorption of ions into an electric double layer. Furthermore, the same types of activated carbon electrodes [18–20] are used to generate the double layer. However, instead of investigating the amount of ions that are removed from the electrolyte, the amount of charge built up on the system is of importance for supercapacitors, plus the rate at which the capacitor can be charged and discharged. To assess charging rate and maximum charge capacity of a supercapacitor, various techniques are used [3, 4, 18, 19, 21, 22] such as electrochemical impedance spectroscopy, cyclic chronopotentiometry, and voltammetry.

All these methods can return resistance values and capacitance values for a certain electrode arrangement. For supercapacitor application, resistance relates to the rate at which the capacitor can be charged and discharged, and capacitance relates to the maximum amount of charge that can be stored. By relating charge storage to ion adsorption, resistance can be related to deionization rate, and capacitance can be related to the maximum amount of ions that can be removed, and therefore electrochemical characterization techniques can also be used to characterize CDI electrode arrangements.

One of the most extensive techniques available is electrochemical impedance spectroscopy (EIS) [23]. EIS is a resistance measurement for alternating current (AC) instead of for direct current (DC). By varying the frequency of an applied sinusoidal cell voltage and measuring the change in the resulting current, an impedance response of a CDI electrode configuration is obtained. This response is a fingerprint of the processes occurring during the deionization process at different time constants; high frequencies correspond with fast processes and low frequencies correspond with slow processes. With EIS the dependence of resistance and capacitance as function of frequency can be obtained, and thus the dependence of deionization rate and capacity on time.

The biggest obstacle in EIS measurements is interpretation of the obtained impedance response. Interpretation is done by comparing a EIS measurement to a theoretical EIS response described by an equivalent circuit [23]. An equivalent circuit is a circuit comprising of elements such as capacitors and resistors that represent physical and chemical processes. It is usually difficult to identify the correct equivalent circuit, since different equivalent circuits can give an equal EIS response. Since a CDI system closely resembles a supercapacitor system, equivalent circuits to describe the EIS response of supercapacitors are used as a starting point in the investigation. These are then modified to accommodate for differences between CDI and supercapacitor configurations.

The objective of this chapter is to investigate the use of EIS to characterize CDI electrode materials in terms of electrical resistance and capacitance. Representative samples of the three most common electrode materials in CDI are investigated, carbon powder, carbon aerogel and carbon fiber. General and validated equivalent circuits are used to describe the electrode system, and per material the applicability of the equivalent circuit is assessed.

If deviations are found between general and validated equivalent circuits and the obtained EIS response, it will be investigated how the equivalent circuit can be modified to account for the deviations. For validation of these modified equivalent circuits, resistance and capacitance results obtained by EIS are compared with results obtained

using a different electrochemical characterization technique, cyclic chronopotentiometry (further referred to as potentiometry).

Characterization is deemed successful if the impedance response matches the impedance response of a validated equivalent circuit and if all elements in the equivalent circuit can be linked to physical processes occurring during the deionization process.

2.3 Theory

2.3.1 Impedance

General

Impedance describes the opposition encountered when an alternating potential is set onto a certain linear (electrotechnical) element such as a resistor or capacitor. This is analogous to Ohm's law as expressed in equation (2.1).

$$i = \frac{E}{Z} \tag{2.1}$$

In this equation, i is the resulting alternating current density in $A\ cm^{-2}$ from the applied alternating potential E, in V. Z, in $\Omega\ cm^2$, is the impedance of the linear element in question.

Figure 2.2 shows an example of an impedance response of a certain linear element with impedance Z. This figure shows that an alternating potential is applied; the amplitude of the potential changes in time due to the imposed frequency. Furthermore, an alternating current is measured, which has the same shape as the applied potential. This means that the impedance response is linear; the response is proportional over the total period. The impedance Z of the linear element has two effects on the measured alternating current. The first effect is that a phase shift is imposed on the measured current, in this case equal to one fourth of a period, or 0.5 π in radians. The second effect is that the maximum amplitude of the measured current is half that of the applied potential, meaning that the amplitude ratio is equal to 2 $\Omega\ cm^2$.

In a direct current resistance measurement, only the amplitude ratio is measured, which would according to Ohm's law result in a constant resistance in $\Omega\ cm^2$. For EIS measurements, the phase shift has to be accounted for. This is done by applying Euler's formula, according to equation (2.2).

$$e^{jx} = \cos x + j \sin x \tag{2.2}$$

By using this equation, the wave function of the applied alternating potential and the measured alternating current density can be split up into a imaginary and real

part, and consequently applied in equation (2.1). As an example, the impedance response as depicted in figure 2.2 is plotted in figure 2.3 in a so-called Nyquist plot. The horizontal axis represents the real part of the impedance Z' in $\Omega\ cm^{-2}$, and the vertical axis represents the negative imaginary part of the impedance $-Z''$ in $\Omega\ cm^2$. By convention the negative imaginary part is the vertical axis instead of the positive imaginary part [23].

The length of the vector in figure 2.3 represents the amplitude ratio, or absolute impedance $|Z|$ ($2\ \Omega\ cm^2$). The angle ϕ ($45°$) of the vector in figure 2.3 represents the phase shift ($0.25\ \pi$). Using equation (2.2) the absolute impedance and phase shift relate to an impedance Z of $\sqrt{2} + \sqrt{2}j\ \Omega\ cm^2$, as is also shown in figure 2.3.

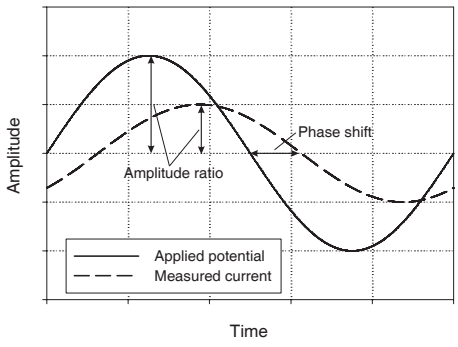

Figure 2.2: Example of an impedance measurement, where amplitude ratio of applied potential over measured current is 2, and the phase shift is $0.25\ \pi$

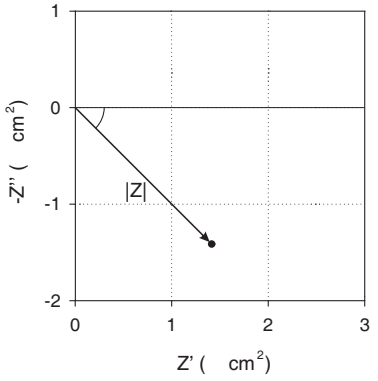

Figure 2.3: Example Nyquist plot showing the absolute impedance $|Z|$ and phase angle ϕ of the impedance of figure 2.2

For many linear electrotechnical elements, such as capacitors and inductors, the impedance Z is dependent on the frequency of the applied potential. By plotting the impedance of a range of frequencies, an impedance response is obtained that is unique for the element under investigation.

When performing an EIS measurement of an unknown system, usually an impedance response is obtained over a wide frequency range. This response is then compared to the impedance response of known linear elements. This way, an equivalent circuit can be constructed for the system under investigation. The electrotechnical elements comprising the equivalent circuit are then related to physical processes in the system under investigation, where each frequency corresponds with the characteristic time of the measured physical process; at high frequency only fast physical processes are measured, at low frequency only slow physical processes are measured.

Equivalent circuit

Figure 2.4 shows the Nyquist plot of a typical EIS measurement of the CDI electrode configuration as described in section 2.4. This response can be split into three distinct sections, where each section shows an impedance response that can be represented by (a combination of) electrotechnical elements, which are also depicted in figure 2.4. Figure 2.5 shows the relation of the electrotechnical elements to physical processes occurring in the CDI electrode configuration. By analyzing the shape of the impedance response from infinite frequency ($\omega \rightarrow \infty$) to zero frequency ($\omega \rightarrow 0$), the impedance response can be linked to the physical processes.

The left hand section of figure 2.4 shows that at $\omega \rightarrow \infty$ the impedance response starts on the real impedance axis Z'. This corresponds with a constant resistance R_s, in $\Omega\ cm^2$ [a].

The middle section of figure 2.4 shows that the impedance response resembles a semi-circle, where the center of the circle is recessed below the real impedance axis Z'. This corresponds with a non-ideal capacitor (referred to as constant phase element, or CPE [23]) Q_d, in parallel with a resistor R_{ct}, in $\Omega\ cm^2$. The unit of Q_d is $F\ cm^{-2}\ s^{n_d-1}$, where n_d is the unitless CPE factor [23] and s is time in seconds. The angle of the semi-circle with the Z'-axis is represented by n_d.

The right hand section of figure 2.4 shows that the impedance initially resembles a line with constant angle α, which at low frequency ($\omega \rightarrow 0$) ends in a vertical line. This corresponds with a transmission line model Z_{tlm}, which is an equivalent circuit used to describe finite diffusion of ions [23].

In summary, a typical impedance response of the CDI electrode configuration as described in section 2.4 is represented by a constant resistance R_s, a non-ideal capacitor Q_d in series with a resistor R_{ct}, and a transmission line model Z_{tlm}. This response is very similar to the response of supercapacitor electrode configurations [23], therefore it is assumed that the characterized electrotechnical elements represent equal physical processes as in supercapacitor electrode configurations.

Figure 2.5 shows that the resistance R_s corresponds to the electrolyte resistance between the two electrodes plus the contact resistance from CDI cell to potentiostat [23]. These two resistances cannot be measured separately, both processes are instantaneous. However, when the contact resistance is relatively small as compared to the electrolyte resistance, R_s can be related to electrolyte conductivity σ in $S\ cm^{-1}$ to obtain the electrochemical spacer thickness, which is expected to be close to the actual spacer thickness.

Figure 2.5 shows that the non-ideal capacitance Q_d in series with the resistance

[a] Due to the cell configuration, also an inductance is measured at $\omega \rightarrow \infty$. This inductance is accounted for, but not considered in the analysis.

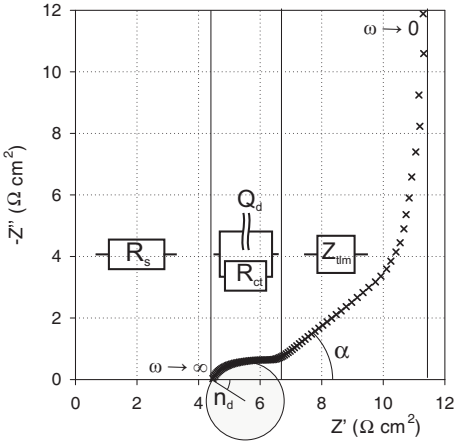

Figure 2.4: Nyquist plot of a typical EIS measurement showing imaginary impedance $-Z''$ versus real impedance Z', where the data is related to (a combination of) electrotechnical elements representing the impedance response. α and n_d relate to the angle of the impedance response with the Z'-axis

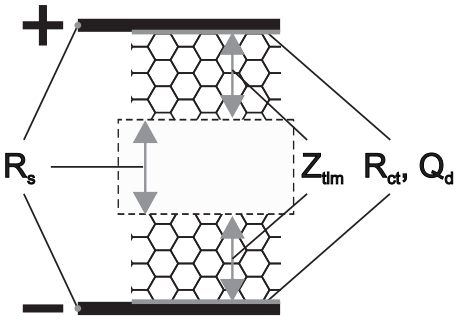

Figure 2.5: Link of the characterized electrotechnical elements as represented in figure 2.4 to the physical processes as represented in figure 2.1

R_{ct} corresponds with a charge-transfer process occurring at the current collector; Q_d corresponds with the geometric capacitance of the current collector surface, and R_{ct} corresponds with the charge-transfer resistance of the interface between current collector and carbon electrode. The used current collector is not ideally flat, and therefore the surface will not act as an ideal capacitor [24]. The impedance of Q_d is shown in equation (2.3) as Z_{Qd} in $\Omega\ cm^2$.

$$Z_{Qd} = \frac{1}{Q_d\,(j\omega)^{n_d}} \tag{2.3}$$

In this equation, j is the imaginary unit and w is the applied radial frequency, in rad s^{-1}. The factor n_d is related to the angle of the semicircle with the real impedance axis Z', as shown in figure 2.5.

Equation (2.4) shows the conversion of Q_d to the equivalent geometric capacitance C_d in $F\ cm^{-2}$ [25].

$$C_d = Q_d\,\omega_{max}^{n_d-1} \tag{2.4}$$

In this equation, ω_{max} is the frequency at the top of the semi circle observed in Nyquist plots in rad s^{-1}.

Since the surface area of the current collectors is very small ($< 0.1\%$) compared to the activated carbon surface area, the effect of C_d on total capacity is negligible. To verify that C_d corresponds to current collector capacitance, C_d should be close to typical double layer capacitance, which is in the range of $2 - 100\ \mu F\ cm^{-2}$ [26].

The other element of the charge-transfer process, the charge-transfer resistance R_{ct} in Ωcm^2, is in literature related to various factors, such as surface groups [27], interface resistance between current collector and carbon [24], structure of carbon pores [28] and polarization resistance of carbon [29, 30]. This implies that R_{ct} is a charge transfer resistance between current collector and carbon electrode, mainly caused by the difference in the electron transport method between current collector and activated carbon. In activated carbon electrons are transported by hopping between electronically coherent domains [31]. This transport is influenced by the natural surface charge of the carbon, which in turn is influenced by electrolyte concentration and surface groups. This explanation would cover most of the hypotheses presented in literature. Therefore R_{ct} is regarded as a charge-transfer resistance, and based on experimental results the exact nature of R_{ct} will be determined.

In figure 2.5 the transmission line model Z_{tlm} corresponds with the diffusion of ions into the porous electrode [23, 24, 27, 32]. No general impedance response for Z_{tlm} exists, this will be further discussed in section 2.3.1.

Figure 2.6 shows the equivalent circuit of the combined elements. Here, Q_d is parallel to both R_{ct} as well as Z_{tlm}. This is since Q_d is in direct contact with the electrolyte, and therefore the current that is used to charge capacitance Q_d does not pass through Z_{tlm}. In literature, setups are used where the current collector is not in direct contact with the electrolyte, therefore all current that is used to charge Q_d then has to pass through Z_{tlm}, meaning that in the subsequent equivalent system Q_d is in series with Z_{tlm} instead of in parallel. Since Q_d is measured at a higher frequency than Z_{tlm}, impedance of Q_d has no significant effect on impedance of Z_{tlm} and therefore the equivalent system used in literature will show very similar impedance behavior to the equivalent system as proposed in this work.

By replacing the elements in figure 2.6 with their respective impedances and when taking into account that series impedances can be simply added together while parallel impedances have to be added reciprocally [23], the total impedance Z in $\Omega\ cm^2$ is obtained as shown in equation (2.5).

$$Z = R_s + \frac{1}{Q_d\,(j\omega)^{n_d} + \frac{1}{R_{ct}+Z_{tlm}}} \tag{2.5}$$

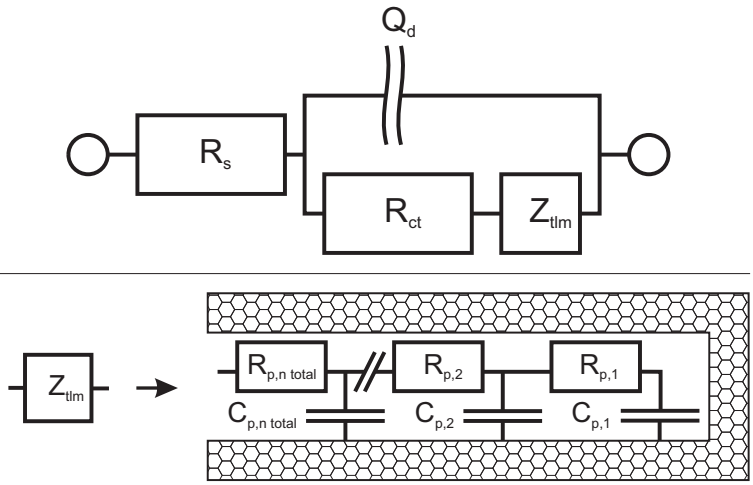

Figure 2.6: Complete equivalent circuit for interpretation of EIS data, bottom section represents the transmission line model Z_{tlm}

Transmission line model

The equivalent circuit used to describe the properties of the carbon electrode is the transmission line model (TLM), with impedance Z_{tlm} in $\Omega\ cm^2$. The TLM is a model for diffusion of ions into the carbon electrode, and is depicted in the bottom section of figure 2.6. This figure shows that the equivalent circuit consists of a finite length transmission line of capacity elements ($C_{p,n}$) and resistance elements ($R_{p,n}$) [28]. In a general situation, capacity and resistance are linearly distributed in the carbon electrode, meaning that the volumetric resistance in $\Omega\ cm$ and volumetric capacitance in $F\ cm^{-3}$ are constant. In this general case, a linear transmission line is obtained (linear TLM), as proposed by De Levie [33].

The analytical expression for the linear TLM, $Z_{tlm,l}$ in $\Omega\ cm^2$, is depicted in equation (2.6) [23].

$$Z_{tlm,l} = \sqrt{\frac{3\,R_c}{j\omega C_c}}\coth\sqrt{j\omega 3 R_c C_c} \tag{2.6}$$

In this equation, R_c in $\Omega\ cm^2$ is the limiting resistance of $Z_{tlm,l}$ at $\omega \rightarrow 0$, corresponding with the resistance of the carbon electrode. C_c in $F\ cm^{-2}$ is the limiting capacitance of $Z_{tlm,l}$ at $\omega \rightarrow 0$, corresponding with the capacitance of the carbon electrode. R_c can be related to the solution conductivity to obtain the effective electrode thickness, and C_c can be related to a double-layer model to obtain the

amount of double-layer area per unit electrode.

The linear TLM is equivalent to diffusion of ions into carbon pores with ideally flat walls. Another common transmission line model is the CPA transmission line model [34], where the walls of the carbon pore are considered rough, and therefore the capacity elements of the transmission line behave as CPA elements. This means that the whole transmission line as described in equation (2.6) is offset by a constant angle versus the Z' axis. The transmission line impedance $Z_{tlm,cpa}$ in $\Omega\ cm^2$ of a TLM consisting of CPA elements is shown in equation (2.7).

$$Z_{tlm,cpa} = \sqrt{\frac{3\,R_c}{(j\omega)^{n_{cpa}}\,Q_c}}\coth\sqrt{(j\omega)^{n_{cpa}}\,R_c Q_c} \tag{2.7}$$

$$Q_c = C_c^{n_{cpa}} R_s^{n_{cpa}-1} \tag{2.8}$$

In this equation, Q_c in $Fcm^{-2}s^{n-1}$ can be transformed to C_c according to equation (2.8) [34]. n_{cpa} is related to the fractal dimension D_f ($2 \leq D_f \leq 3$) according to equation (2.9).

$$D_f = \frac{1}{n_{cpa}} + 1 \tag{2.9}$$

$D_f = 2$ corresponds with carbon pores where the walls are ideally flat (2 dimensional), and $D_f = 3$ corresponds with carbon pores where the walls are fully porous (3 dimensional). Furthermore, n_{cpa} can be related to the angle of the transmission line α, according to equation (2.10).

$$\alpha = 45^\circ\, n_{cpa} \tag{2.10}$$

For each investigated carbon type, the most suitable transmission line element is chosen based on characterization results. If no suitable transmission line is available, an existing transmission line is modified.

Fitting procedure

To obtain values for all characterization parameters (R_c, C_c, n_{cpa}, R_s, R_{ct}, Q_d and n_d), a fitting procedure is used. This procedure changes the values for the characterization parameters in such a way that the difference between the theoretical impedance response (the model, according to equation (2.5)) and the measured impedance response (the data) is minimized. This minimization is performed by a nonlinear minimization routine, which is based on the interior-reflective Newton method [35]. The target function of this routine is shown in equation (2.11).

$$\sum \left[\left(\frac{\log |Z_m| - \log |Z|}{\sigma_{|Z|}} \right)^2 + \left(\frac{\phi_m - \phi}{\sigma_\phi} \right)^2 \right] \tag{2.11}$$

In this equation, $|Z_m|$ and ϕ_m are respectively amplitude ratio and phase angle calculated by the model, $|Z|$ and ϕ are respectively amplitude ratio and phase angle given by the data, $\sigma_{|Z|}$ is relative measurement error of amplitude ratio (0.02 %) and σ_ϕ is absolute measurement error of phase angle (0.01°). The measurement errors σ_ϕ and $\sigma_{|Z|}$ were obtained from the specifications of the potentiostat, and validated by performing an EIS experiment on a 100 Ω resistor.

The fitting procedure returns estimated values, standard deviations and correlation coefficients for the model parameters. Correlation coefficients are needed to correctly calculate standard deviations of parameters that are comprised of multiple model parameters, such as R_{total} and C_d.

2.3.2 Potentiometry

To validate any non-standard transmission line model, EIS results are compared with potentiometry results for various cell voltages. Potentiometry is based on measurement of cell voltage as function of an applied constant current. By reversing the current at a certain cell voltage, capacity and resistance values are obtained at this cell voltage [36]. By choosing a very low constant current, the discharge time of the potentiometry experiments is much longer than the characteristic time of the system, equivalent to measuring impedance at $\omega \rightarrow 0$. Instead of measuring the separate physical and chemical processes in the system as described in section 2.3.1, the total resistance and total capacitance is measured. Figure 2.7 shows the equivalent circuit as measured with potentiometry at very low constant current. The equivalent circuit consists of the total resistance R_{total} (in $\Omega\, cm^2$) in series with total capacitance C_c (in $F\, cm^{-2}$). R_{total} is the linear addition of all resistance elements in the equivalent circuit, so the sum of R_s, R_{ct} and R_c. The geometric capacitance C_d is considered negligible, therefore the total capacitance is equal to the carbon electrode capacitance C_c.

Figure 2.8 illustrates extraction of total resistance and total capacitance from experimental data [36]. In this figure, cell voltage E_{cell} in V is plotted against time t in s during a typical potentiometry experiment.

Point one and two indicate switching of the polarity of the constant current because a predefined value of E_{cell} is reached. Point one is considered as the start of the charging process, and point two as the start of the discharging process. The voltage drop ΔE_v at point two is according to Ohm's law, and given by equation (2.12).

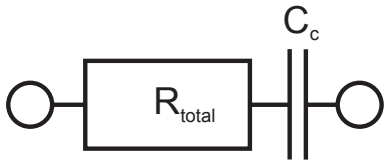

Figure 2.7: Limiting equivalent circuit for interpretation of potentiometry data

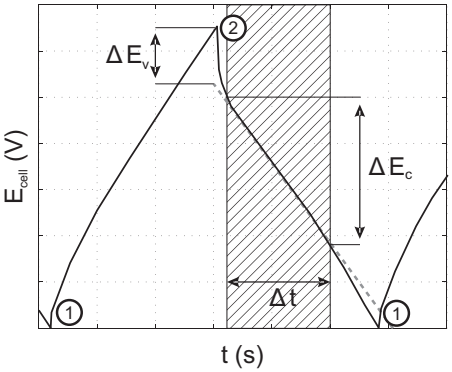

Figure 2.8: Example potentiometry experiment with illustration of voltage drop method; point 1 indicates application of a positive constant current, point 2 indicates application of a negative constant current. ΔE_v is the voltage drop, and evolution of ΔE_c over Δt is a measure for total capacitance

$$\Delta E_v = 2\ iR_{total} \tag{2.12}$$

In this equation i is the constant current in $A\ cm^{-2}$, the factor two exists since the potential drop is due to the difference in charging and discharging current.

To obtain total capacitance C_c, data from the discharging process is used, since the discharging process contains less Faradic current than the charging process [36]. Equation (2.13) shows derivation of the total capacitance C_c in $F\ cm^{-2}$.

$$C_c = i\frac{\Delta t}{\Delta E_c} \tag{2.13}$$

In this equation ΔE_c in V is the change in cell voltage E_{cell} in time period Δt in s. Since capacity changes with cell voltage [36], the slope of the discharge line deviates from linearity at lower cell voltages, especially at lower concentrations. Therefore only the first 50% of the discharge line is considered in obtaining C_c.

2.4 Materials and methods

2.4.1 Experimental setup

The experimental setup consisted of a CDI cell immersed in a vessel containing an electrolyte. This electrolyte consisted of a 0.1 M NaCl (analytical grade, Boom, Meppel,

The Netherlands) solution in MilliQ water (Millipore, Etten-Leur, The Netherlands). Temperature of the entire system was kept constant at $T = 298 \pm 0.2\ K$. A NaCl solution was used as electrolyte since NaCl is the major component in many deionization applications. Electrolyte content of the total system was 2.5 liters. This large volume was chosen to minimize concentration changes that would affect kinetics of the adsorption process [26]. The entire setup was situated in a Faraday cage to minimize electromagnetic interference during measurements.

Figure 2.9 and figure 2.10 depict the CDI cell. Numbers in figure 2.10 correspond to bold numbers in the following lines. To apply current to the electrode material under investigation, a current collector was used. This current collector was a 36 cm^2 platinum coated (20 g Pt m^{-2}) titanium mesh (mesh size 5.9 x 3.5 mm, Magneto Special Anodes BV, Schiedam, The Netherlands) **(1)**. Two layers of electrode material **(2)** of 36 cm^2 were put between the current collectors. These layers were separated by an insulating spacer **(3)** which was bigger than the electrodes to prevent electrical short circuit. The insulating spacer material was a glass fiber filter material (Millipore AP20, 380 μm thick with binder resin). The cell configuration was held together by an external polytetrafluoroethylene (PTFE) frame **(4)** and polyamide screws.

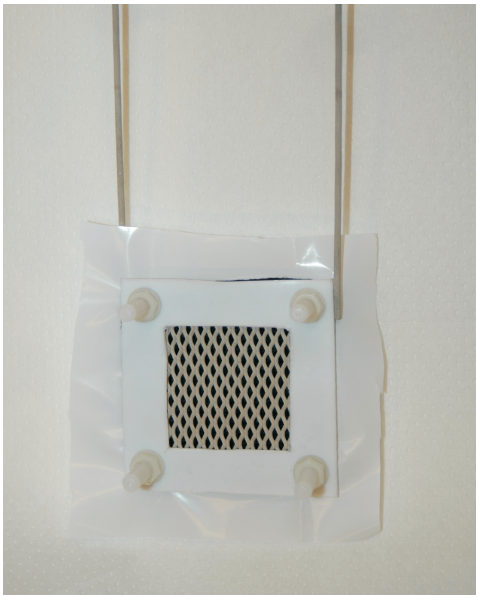

Figure 2.9: Picture cell configuration

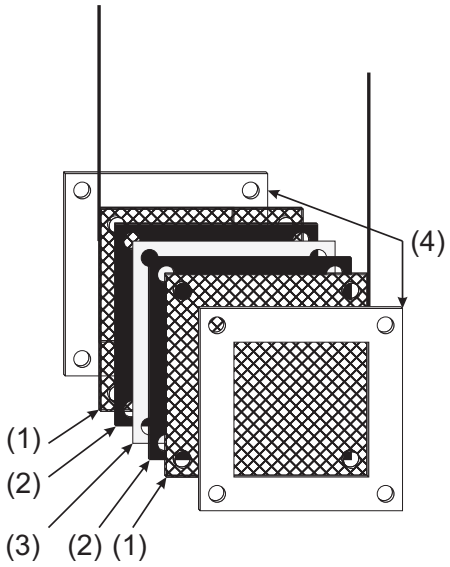

Figure 2.10: Diagram cell configuration showing current collector (1), carbon fiber electrode (2), spacer (3) and PTFE frame (4)

Three different carbon types were tested, carbon fibers (in the form of felt), carbon powders (in a mixture with polyvinylidene fluoride) and carbon aerogel. Characteristics of these materials were obtained as described in chapter 5 and are shown in table 2.1.

Table 2.1: Physical properties of the investigated electrode materials

Material	Type	Surface area (BET) $m^2\ g^{-1}$	Carbon loading $mg\ cm^{-2}$	Thickness μm
Norit A Supra Eur	Powder	1770	25.3	320
CDT Aerogel	Aerogel	280	103	865
Kuraray FT 300-15	Fiber	1270	36.6	1000

All experiments were performed with an Autolab PGSTAT 30 potentiostat (Eco Chemie, Utrecht, The Netherlands). No reference electrode was used, since the used CDI cell is a symmetrical configuration; cathode is identical to anode.

Before the CDI cell was introduced into the vessel, the CDI cell was immersed in the electrolyte solution and vacuum treated (< 5 kPa) for 24 hours to wet all pores of the carbon felt. The electrolyte in the vessel was purged with nitrogen for 30 minutes before each experiment to remove dissolved oxygen and dissolved carbon dioxide.

During experiments, conductivity was continuously measured to assess the extent of evaporation, and pH was continuously measured since pH changes indicate occurrence of redox processes.

2.4.2 Experiments

Transmission line modeling

An EIS experiment was performed at zero volt cell voltage to select the most relevant transmission line model for each of the electrode materials. The alternating voltage had an amplitude of 5 mV and a logarithmically spaced frequency range of 100 kHz - 0.5 mHz. During EIS experiments nitrogen was flushed through the headspace of the reactor to prevent oxygen and carbon dioxide from dissolving into the electrolyte. The electrolyte solution was not stirred during the experiment; since EIS measurements relies on diffusion limitation, convective transport of ions has to be prevented.

Validation

To validate custom equivalent circuits, capacity and resistance results for both EIS as potentiometry were obtained at equal conditions. Cell voltages of 0.3, 0.6, 0.9, 1.2 and 1.4 V were used, at both negative as well as positive cell voltage.

Potentiometry experiments were performed by charging the cell with a positive current until the desired cell voltage was reached, followed by charging the cell with a negative current until the desired negative cell voltage was reached. This was done for at least four cycles, at a current density of $\pm$ 0.625 $mA\ cm^{-2}$. Since each cycle comprises of two discharge curves, one for positive cell voltage and one for negative cell voltage, capacitance and resistance values were obtained for both polarities. Obtained capacity and resistance results from second through fourth scan were averaged to produce the final result. The first cycle was omitted to ensure results from a steady state situation. During potentiometry experiments, the electrolyte solution was stirred to reduce local pH and conductivity changes, and purged with nitrogen to prevent oxygen and carbon dioxide from dissolving into the water. Positive and negative potentiometry results were averaged to result in one capacity and resistance per cell voltage, to correct for any asymmetry between the two electrodes.

EIS experiments were performed at zero volt cell voltage, at positive cell voltage and at negative cell voltage. The superimposed alternating voltage had an amplitude of 5 mV and a logarithmically spaced frequency range of 100 kHz - 0.5 mHz. The experiments performed at zero volt cell voltage were used to confirm that applied cell voltages did not affect the cell.

Positive and negative EIS results were averaged to result in one capacity and resistance per cell voltage, to correct for any asymmetry between the two electrodes. The results for zero volt cell voltage were also averaged, the variability of these results is a measure for reproducibility.

2.5 Results and discussion

2.5.1 Model selection

Powder

Figure 2.11 shows the impedance response of the carbon powder electrode configuration together with the linear TLM fit (equation (2.6)), represented in a Nyquist plot. The figure shows that the linear TLM accurately represents the impedance of a carbon powder electrode, showing a transmission line angle of 45°. Since the linear transmission line model has been validated in literature [37], validation was not deemed necessary.

Aerogel

Figure 2.12 shows the impedance response of the carbon aerogel electrode configuration, together with the constant phase angle TLM fit (equation (2.7)), represented in a Nyquist plot. The figure shows that the the CPA TLM reasonably represents the impedance of a carbon powder electrode, showing a transmission line angle of 40.1°. The fit is not perfect, and therefore validation of the CPA model is necessary.

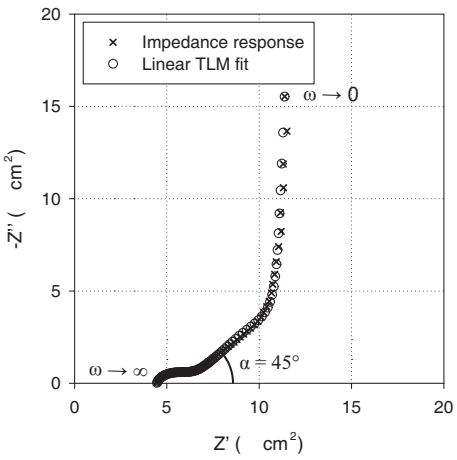

Figure 2.11: Nyquist plot of carbon powder electrode impedance response, fitted with linear transmission line model

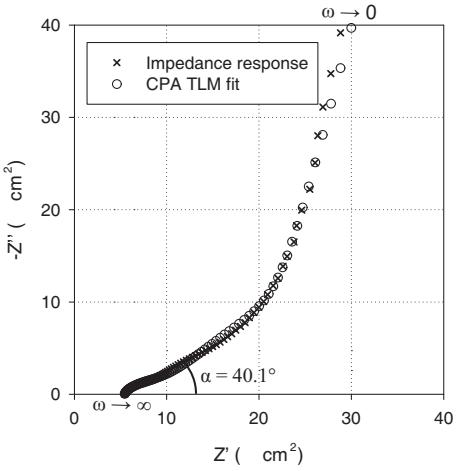

Figure 2.12: Nyquist plot of carbon aerogel electrode impedance response, fitted with CPA transmission line model

Fiber

Figure 2.13 shows the impedance response of the carbon fiber electrode configuration, represented in a Nyquist plot. As shown in this figure, the impedance response does not correspond with any transmission line model, best fit results were obtained with the linear transmission line model (equation (2.6)).

However, the linear TLM does not reproduce the experimental data to a satisfactory level. The measured transmission line angle deviates from the expected 45° angle, while the transmission line does end in the expected 90° angle. The measured transmission line response can be explained by a pore geometry that deviates from ideality [28]. It was found that a power law distribution of resistance in the electrode will result in the observed constant deviation of phase angle, resulting in a power law TLM, as derived in section 2.A. For this power law TLM, an extra parameter

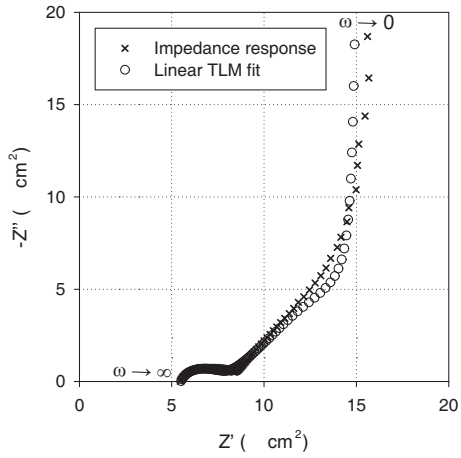

Figure 2.13: Nyquist plot of carbon fiber electrode impedance response, fitted with linear transmission line model

n_c is required, which is the power of the resistance distribution. When $n_c = 1$, the power law TLM is equal to a linear TLM. Since activated carbon is comprised of a distribution of many pores, all with different shapes and sizes [18], the factor n_c in the power law TLM can not only be attributed to a pore shape effect. Therefore, n_c is attributed to the distribution of resistance over capacitance.

Figure 2.14 shows a comparison between distributions with various values for n_c. In this figure, $\int_0^z C_p dz$ is the moving integral of capacitance as function of z, and $\int_0^z R_p dz$ is the moving integral of resistance as function of z, where z in cm is the position in the transmission line. As shown in this figure, in the case of $n_c < 1$ *resistance* is concentrated in the front of the transmission line, and in the case of $n_c > 1$ *capacitance* is concentrated in the front of the transmission line. Therefore, materials with a $n_c > 1$ are more interesting for CDI. A full derivation of the power law TLM is shown in appendix 2.A, together with relation between transmission line angle and power law factor n_c.

Figure 2.15 shows the impedance response of the carbon fiber electrode configuration together with the power law TLM fit, represented in a Nyquist plot. The figure shows that the power law TLM describes the impedance response accurately. The fit resulted in a value for n_c of 1.44, or a transmission line slope α of 53°. Figure 2.14 shows that the physical meaning of a $n_c > 1$ is that capacitance is concentrated in the front of the transmission line, and therefore resistance is concentrated in the back of the transmission line.

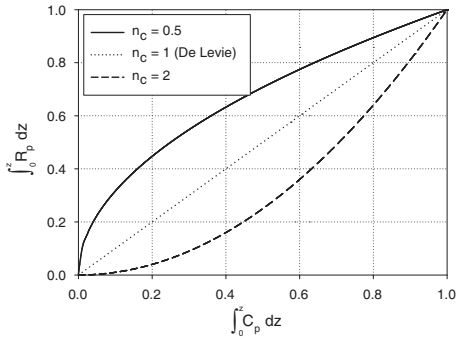

Figure 2.14: Distribution cumulative resistance over cumulative capacitance in the power law transmission line model as function of power factor n_c

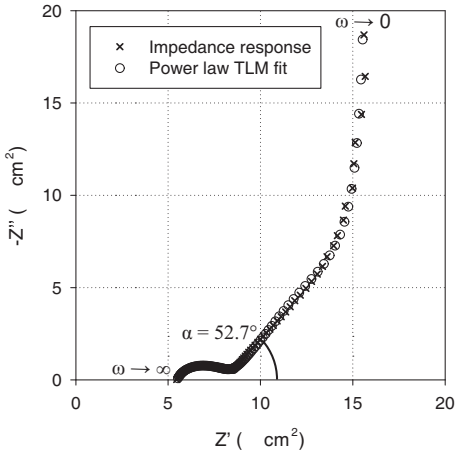

Figure 2.15: Nyquist plot of carbon fiber electrode impedance response, fitted with power law transmission line model

2.5.2 Validation

Redox effects

At cell voltages higher than 0.3 V fluctuations in pH during potentiometry experiments were measured, and a drop in pH during EIS experiments. This was most noticeable at high cell voltage, the pH dropped from approximately 7 to 3.43 during an EIS experiment at -1.4 V. This is attributed to surface redox reactions, which affects interpretation of EIS [27]. Figure 2.16 shows the impedance response of the carbon fiber electrode configuration at a constant cell voltage of -1.4 V, represented in a Nyquist plot.

This figure shows the formation of a semicircle for the experimental data at low frequencies, where the diameter ∅ of this semicircle is the redox resistance [27], and approximately 500 $\Omega\ cm^2$. Since the used equivalent circuits do not include redox effects, the fitting procedure accounts for this effect by modifying the values for n_d and n_c (in case of power law TLM) or n_{cpa} (in case of CPA TLM), as shown in figure 2.16 as the fitted data. This is not correct, since n_c, n_d and n_{cpa} relate to the surface properties of the carbon and the current collector and therefore are independent of cell voltage. Therefore for cell voltages higher than 0.3 V the values of n_d , n_c and n_{cpa} of the measurements at 0 and 0.3 V were used. This forces the fitting routine

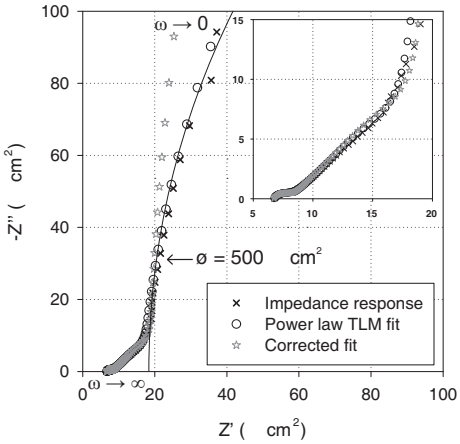

Figure 2.16: Nyquist plot of carbon fiber electrode response at -1.4 V cell voltage, comparison of different fits. Inset shows magnification of the data comprising the transmission line. Solid line is a section of the circle with diameter $\varnothing = 500\ \Omega\ cm^2$, representing redox reactions.

to neglect the effect of redox reactions on impedance. The corrected fit is also shown in figure 2.16, where it can be seen that the formation of a semi circle is much less pronounced, while the inset shows that the fit still represents the transmission line response accurately.

Aerogel

Figure 2.17 shows the comparison of aerogel EIS results with potentiometry results. As shown in this figure, capacity C_c increases with cell voltage E_{cell}, in accordance with double-layer theory [26]. For all values of E_{cell}, EIS data is in close agreement with potentiometry data. All EIS resistance values were stable for all cell voltages; for R_{total} an average value of $17.4 \pm 0.2\ \Omega\ cm^{-2}$ was found. For potentiometry, for R_{total} an average value of $18 \pm 2\ \Omega\ cm^{-2}$ was found.

Fiber

Comparison of fiber EIS results with potentiometry results is shown in figure 2.18. As shown in this figure, capacity C_c increases with cell voltage E_{cell}, in accordance with double-layer theory [26]. However, the extent of this increase is much less than with carbon aerogel. For all values of E_{cell}, EIS data is in close agreement with potentiometry data.

All EIS resistance values were stable for all cell voltages; for R_{total} an average value of $24.3 \pm 0.7\,\Omega\ cm^{-2}$ was found. For potentiometry, for R_{total} an average value of $25 \pm 4\,\Omega\ cm^{-2}$ was found.

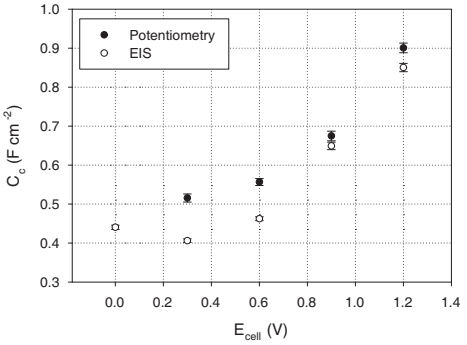

Figure 2.17: Capacity versus cell voltage for carbon aerogel electrode configuration, obtained using potentiometry and EIS

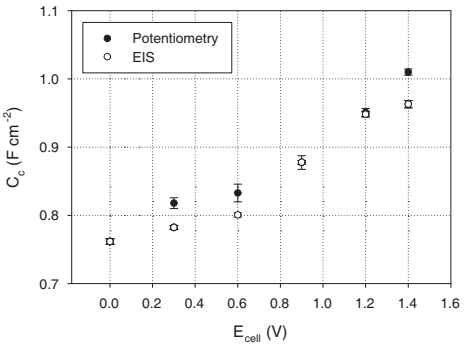

Figure 2.18: Capacity versus cell voltage for carbon fiber electrode configuration, obtained using potentiometry and EIS

Comparison material characteristics

Table 2.2 summarizes the results of the characterization. For fiber data, an average of six experiments is taken; for powder data, an average of two experiments is taken; for aerogel data an average of four experiments is taken. The reported standard deviation is determined over the subsequent number of experiments performed, while taking into account the standard deviations and correlation coefficients of the separate experiments. All experiments were performed at $E_{cell} = 0\ V$.

Table 2.2 shows for most measurements a low standard deviation, and therefore a high accuracy. Capacity C_c is obtained with an accuracy of $\pm 5\%$, and total resistance is obtained with an accuracy of $\pm 1\%$. Accuracy in obtaining R_{total} is in some cases better than accuracy of obtaining separate resistance elements. This is due to correlation between two parameters, and can clearly be seen in determining R_{ct} and R_c of carbon aerogel. In this case the algorithm has difficulties discerning R_{ct} and R_c separately, but still it can obtain an accurate value for R_{total}.

Geometric capacitance C_d for fiber and powder data correspond to literature values of $2 - 100\ \mu F$. Furthermore, C_d remained constant when performing experiments where only the carbon electrode size was varied and not the current collector size. This confirms that C_d is only related to the size of the current collector, and not to the size of the sample.

Table 2.2: Obtained parameters from impedance characterization for all investigated carbon electrodes

Parameter	Fiber	Powder	Aerogel	Unit
TLM	Power law	Linear	CPA	
R_c	8.5 ± 0.5	4.74 ± 0.2	13.7 ± 0.5	$\Omega\ cm^2$
C_c	0.762 ± 0.004	0.42 ± 0.01	0.34 ± 0.01	$F\ cm^{-2}$
n_c / n_{cpa}	1.17 ± 0.01	–	0.900 ± 0.003	–
R_s	5.9 ± 0.1	4.08 ± 0.01	5.2 ± 0.06	$\Omega\ cm^2$
R_{ct}	3.2 ± 0.2	2.7 ± 0.2	5.5 ± 0.5	$\Omega\ cm^2$
R_{total}	17.6 ± 0.4	11.47 ± 0.02	24.4 ± 0.1	$\Omega\ cm^2$
C_d	56 ± 3	88 ± 4	480 ± 50	$\mu F\ cm^{-2}$
n_d	0.442 ± 0.005	0.534 ± 0.004	0.535 ± 0.005	–

2.6 Conclusion

In the analysis of materials for use in CDI cells, EIS is a valuable method to obtain information on characteristics of the cells. For EIS analysis of carbon powder and carbon aerogel existing transmission line models for the diffusion of ions into the carbon can be used, for EIS analysis of carbon fibers a new transmission line model is developed, the power law transmission line model. The power law transmission line model contains an extra characteristic, the power of the resistance distribution n_c, which describes the distribution of resistance over capacitance. If $n_c > 1$, capacitance is concentrated in the front of the transmission line and if $n_c < 1$, resistance is concentrated in the front of the transmission line. Therefore, a higher value for n_c is advantageous, since it is desirable to have capacity concentrated in the front of the transmission line since then capacity can be accessed faster.

When using the transmission line models as presented in this work, EIS gives reproducible and reliable information on several important material properties. These properties include capacitance and resistance distribution in the carbon pores, charge transfer resistance between carbon electrode and current collector, and resistance of the electrolyte and spacer compartment between the carbon electrodes.

When only total resistance and total capacitance are of importance, cyclic chronopotentiometry is a good alternative characterization method; the obtained results are equal to EIS results. However, with EIS the accuracy of the obtained parameters are significantly higher.

2.A Appendix 1: Derivation of power law transmission line model

This appendix describes the derivation of the power law transmission line model (power law TLM). First, the linear TLM is described, which is used as a basis for the power law TLM as proposed in this work. To obtain the impedance as well as the limiting capacitance and limiting resistance of the power law TLM, a continuous analytical solution is used.

2.A.1 Transmission line model

General

A transmission line model (TLM) is a model for diffusion of ions into a carbon electrode. The most general model is the linear TLM developed by De Levie [37], where work was done on a collection of parallel platinum wires, forming the equivalent of a single linear pore. Of course in a porous carbon electrode there is more than one pore, and in general these pores are not parallel and not linear [38]. However, since they can behave like they are parallel and in some cases linear, as shown in this chapter, we will consider the carbon electrodes as a single carbon pore.

Figure 2.19 shows the linear TLM represented as a single carbon pore. As shown in this figure, the linear TLM is the distribution of resistance elements R_p in $\Omega\ cm$ and capacitance elements C_p in $F\ cm^{-3}$ in a carbon pore as function of penetration depth z, which runs from 0 through the total length of the pore l, in cm.

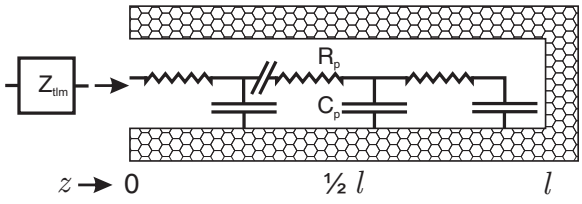

Figure 2.19: Diagram linear transmission line model

When performing EIS, impedance is measured as function of frequency. At very high frequency, ions have no time to penetrate into the carbon pore. Therefore z equals 0 and no resistance nor capacitance is included in the measured impedance. At lower frequencies, ions move into the carbon pore, and capacity and resistance is included in the measured impedance. At very low frequencies, the entire carbon pore is measured, z equals l and the total amount of resistance and capacitance of the

TLM is included in the measured impedance. This means that the integral of C_p and R_p with respect to z is of importance when performing EIS measurements.

The integral $\int_0^z C_p\,dz$ in $F\ cm^{-2}$ is the integral of capacity in a carbon pore, and the integral $\int_0^z R_p\,dz$ in $\Omega\ cm^2$ is the integral of resistance in a carbon pore. When the end of the carbon pore is reached, the total integral of capacity $\int_0^l C_p\,dz = C_{p,total}$ in $F\ cm^{-2}$ and total integral of resistance $\int_0^l R_p\,dz = R_{p,total}$ in $\Omega\ cm^2$ is measured.

In case of the linear TLM [37], $\int_0^z R_p\,dz$ and $\int_0^z C_p\,dz$ increase linearly with z, and therefore C_p and R_p are constant with respect to z. These relations are shown in equations (2.14) and (2.15) for capacity.

$$\int_0^z C_p\,dz = Cz \tag{2.14}$$

$$C_p(z) = C \tag{2.15}$$

In these equations, C is the volumetric capacity in $F\ cm^{-3}$. This means that lC is equal to total transmission line capacity $C_{p,total}$ in $F\ cm^{-2}$.

In equations (2.16) and (2.17) the relation between R_p and z is shown.

$$\int_0^z R_p\,dz = K\frac{z}{l} \tag{2.16}$$

$$R_p(z) = \frac{K}{l} \tag{2.17}$$

In these equations, K/l is the volumetric resistance in $\Omega\ cm$. This means that K is equal to total transmission line resistance, $R_{p,total}$ in $\Omega\ cm^2$.

Impedance of the linear TLM [23] is shown in equation (2.18).

$$Z_{tlm} = \sqrt{\frac{K}{lj\omega C}}\coth\sqrt{Klj\omega C} \tag{2.18}$$

$$K = 3R_c \tag{2.19}$$

$$lC = C_c \tag{2.20}$$

In these equations, ω is the radial frequency of applied AC voltage in rad s^{-1}, j is the imaginary unit ($j = \sqrt{-1}$), K is related to R_c, the limiting resistance at $\omega \to 0$ in $\Omega\ cm^2$ and lC is equal to C_c, the limiting capacitance at $\omega \to 0$ in $F\ cm^{-2}$. For CDI application, the limiting capacitance and resistance are the parameters that directly relate to ion adsorption and deionization rate.

Power law TLM

The *difference* between power law TLM and linear TLM is that with power law TLM the resistance elements R_p are not constant with respect to z, but are a function of z. Still a constant C_p in the power law TLM is used. For net pore impedance it is irrelevant whether C_p or R_p is a function of z, both can return an equal TLM. Therefore, TLM results have to be interpreted as distribution of resistance $\int_0^z R_p\, dz$ versus distribution of capacitance $\int_0^z C_p\, dz$.

The power law relation between $\int_0^z R_p\, dz$ and z is shown in equation (2.21).

$$\int_0^z R_p\, dz = K \left(\frac{z}{l}\right)^{n_c} \tag{2.21}$$

In this equation, n_c is the dimensionless power law factor. When differentiating equation (2.21), R_p as function of z is obtained, as is shown in equation (2.22).

$$R_p(z) = n_c K \left(\frac{z}{l}\right)^{n_c - 1} \tag{2.22}$$

For capacitance, the original linear distribution of equation (2.14) is used. In figure 2.20 a comparison of both distributions is shown for $K = lC = 1$ and various values for n_c.

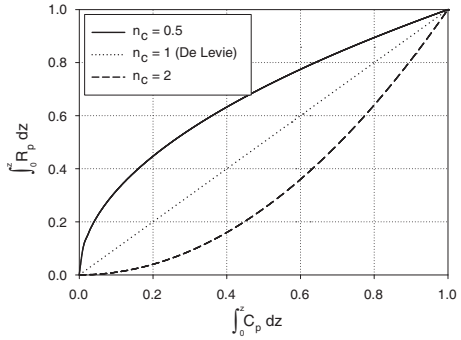

Figure 2.20: Distribution cumulative resistance over cumulative capacitance in the power law transmission line model as function of power factor n_c

This figure shows that if n_c equals 1 the linear TLM is obtained, and therefore resistance increases linearly with capacitance. If $n_c < 1$, resistance is concentrated in the front of the transmission line, and if $n_c > 1$, capacitance is concentrated in the front of the transmission line.

Derivation TLM impedance

To obtain the impedance of the power law TLM, a similar derivation procedure as followed by De Levie is used. Figure 2.21 shows an infinitesimally small section dz of the transmission line, reprinted from De Levie [37]

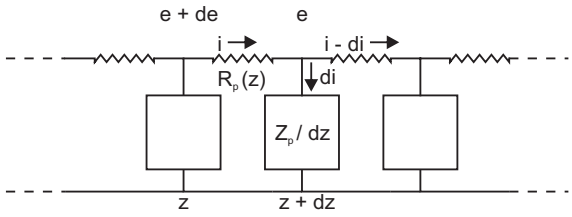

Figure 2.21: Infinitesimally small section dz of the transmission line, reprinted from De Levie [37]

In this figure, $R_p(z)$ in $\Omega\ cm$ is the distribution of resistance elements as function of position z in cm in the carbon pore. This resistance distribution is defined according to equation (2.22). The carbon pore starts at $z = 0$, the boundary between carbon pore and bulk solution, and ends at $z = l$, the end of the carbon pore. The element Z_p in $\Omega\ cm$ represents the impedance of the surface of the pore. This impedance is related to the volumetric capacitance C in $F\ cm^{-3}$ which is considered constant in both the linear TLM as well as in the power law TLM.

When applying a certain potential $e+de$ in V over the transmission line, a current i in $A\ cm^{-2}$ flows through $R_p(z)$, therefore potential e decreases by de. Furthermore, due to the impedance Z_p/dz, current i decreases by di since charge is stored on the surface of the pore. These relations are summarized in equation (2.23) through (2.25).

$$\frac{de}{dz} + iR_p(z) = 0 \tag{2.23}$$

$$\frac{di}{dz} + \frac{e}{Z_p} = 0 \tag{2.24}$$

$$Z_p = \frac{1}{j\omega C} \tag{2.25}$$

By substituting equations (2.24), (2.25) and (2.22) in equation (2.23), a second order differential equation is obtained, as shown in equation (2.26).

$$\frac{d^2i}{dz^2} - j\omega CKn_c \left(\frac{z}{l}\right)^{n_c-1} i = 0 \tag{2.26}$$

To solve equation (2.26), two boundary conditions are defined. At $z = l$ the transmission line ends, and therefore at this point the current is zero. Furthermore,

at $z = 0$ the applied potential e is equal to the total potential over the transmission line E_0 in V. These boundary conditions are shown in equations (2.27) and (2.28).

$$i(l) = 0 \tag{2.27}$$

$$e(0) = E_0 \tag{2.28}$$

To obtain Z_{tlm}, equation (2.26) is rewritten as a Bessel differential equation. Since the solution to a Bessel differential equation is known [39], an analytical solution for current i as function of position z can be obtained. The general form of a Bessel differential equation is shown in equation (2.29).

$$z^2 \frac{d^2y}{dz^2} + z\frac{dy}{dz} + (z^2 - a^2)y = 0 \tag{2.29}$$

To rewrite equation (2.26) into the Bessel differential equation, the substitutions as shown in equations (2.30) through (2.33) are performed.

$$i = z^a B \tag{2.30}$$

$$z = \frac{1}{2a} y^{2\,n_*} \tag{2.31}$$

$$n_* = \frac{1}{1 + n_c} \tag{2.32}$$

$$a^2 = \frac{-(n_c + 1)^2}{j\omega C K n_c l^{1-n_c}} \tag{2.33}$$

The resulting Bessel differential equation can be transformed to an analytical solution for the current i as function of position z in the transmission line. Transmission line impedance is defined according to equation (2.34).

$$Z_{tlm} = \frac{E_0}{i(0)} \tag{2.34}$$

Together with the analytical solution for the current i, equation (2.34) results in equation (2.35), the analytical solution for the transmission line impedance.

$$Z_{tlm} = A\frac{(-j\omega_*)^{n_*}\,\mathrm{J}_{-n_*}\left(2\,n_*\sqrt{-j\omega_*}\right)}{-j\omega_*\mathrm{J}_{n_*}\left(2\,n_*\sqrt{-j\omega_*}\right)} \tag{2.35}$$

$$A = -\frac{K\,(-1 + n_*)\left(\frac{1}{n_*}\right)^{-2\,n_*}\left[\Gamma\,(-n_*)\right]^2 \sin\left(\pi n_*\right)}{\pi} \tag{2.36}$$

$$n_* = \frac{1}{1 + n_c} \tag{2.37}$$

$$\omega_* = n_c K l C \omega \tag{2.38}$$

In this equation, $\Gamma(x)$ is the Gamma function of argument x, and $\mathrm{J}_v(x)$ is the Bessel function of the first kind of argument x with order v. For clarity, the function is displayed using the constant A independent of frequency ω, and dimensionless factors n_* and ω_* (equations (2.37) and (2.38)).

2.A.2 Power law TLM characteristics

Three important characteristics of the power law TLM are the limiting equivalent capacitance C_c in $F\ cm^{-2}$, the slope α of the transmission line and the limiting equivalent resistance R_c, these can be derived from equation (2.35).

Equivalent capacitance

Since C_p is constant according to equations (2.14) and (2.15), limiting capacitance C_c of the transmission line is defined according to equation (2.39).

$$C_c = lC \tag{2.39}$$

Transmission line slope

The slope α of the transmission line is equal to the phase angle of the impedance Z_{tlm} at $\omega \to \infty$, which according to equation (2.38) is equivalent to Z_{tlm} at $\omega_* \to \infty$. As follows from equation (2.35), when $\omega_* \to \infty$, the argument of the Bessel functions go to zero. Therefore the Bessel fraction in equation (2.35) becomes constant [39], as shown in equation (2.40).

$$Z_{tlm}(\omega_* \to \infty) = A_* \frac{(-j\omega_*)^{n_*}}{-j\omega_*} \tag{2.40}$$

In equation (2.40), A_* is a proportional real number related to A, and therefore has no effect on the phase angle of Z_{tlm}. The expression for α is equal to the phase angle of equation (2.40). The result is shown in equation (2.41), where n_* is replaced by equation (2.37).

$$\alpha = \frac{90^\circ}{\frac{1}{n_c} + 1}. \tag{2.41}$$

When $n_c = 1$ a slope of 45° is obtained, and in that case the power law TLM is equal to the linear TLM.

Equivalent resistance

The equivalent resistance of a TLM is defined as the equivalent resistance at $\omega \to 0$. Since at this point the phase angle of the TLM is 90°, the equivalent resistance R_c can be obtained from the real part of Z_{tlm} at $\omega \to 0$, which according to equation (2.38) is equivalent to the real part of Z_{tlm} at $\omega_* \to 0$.

In contrary to the situation at $\omega_* \to \infty$, at $\omega_* \to 0$ the Bessel fraction of equation (2.35) does not become constant. However, for small values of the argument x, the limiting Bessel function as shown in equation (2.42) can be used for both positive as well as negative orders of v [39].

$$\mathrm{J}_v(x \to 0) = \frac{\left(\frac{x}{2}\right)^v}{v!} - \frac{\left(\frac{x}{2}\right)^{v+2}}{(v+1)!} \tag{2.42}$$

When replacing the Bessel functions in equation (2.35) with equation (2.42), and taking $\omega_* \to 0$, the transmission line impedance at $\omega_* \to 0$ is obtained. The real part of this equation is equal to the limiting resistance R_c, and is shown in equation (2.43).

$$R_c = 2\frac{K}{(n_c+1)(n_c+2)}. \tag{2.43}$$

When $n_c = 1$ the equation for limiting resistance of the linear TLM is obtained, equal to equation (2.19).

2.A.3 Summary

Figure 2.22 shows Nyquist plots of the power law TLM for $R_c = C_c = 1$ and various values of n_c. As shown in this figure, phase angles deviating from 45° can be obtained using a power law TLM, and at $n_c = 1$ the linear TLM is obtained.

Bibliography

[1] A. Ban, A. Schafer, and H. Wendt. Fundamentals of electrosorption on activated carbon for wastewater treatment of industrial effluents. *Journal of Applied Electrochemistry*, 28(3):227–236, 1998.

[2] H. Oda and Y. Nakagawa. Removal of ionic substances from dilute solution using activated carbon electrodes. *Carbon*, 41(5):1037–1047, 2003.

[3] Y. Oren and A. Soffer. Electrochemical parametric pumping. *Journal of the Electrochemical Society*, 125(6):869–875, 1978.

[4] A. Afkhami. Adsorption and electrosorption of nitrate and nitrite on high-area carbon cloth: an approach to purification of water and waste-water samples. *Carbon*, 41(6):1320–1322, 2003.

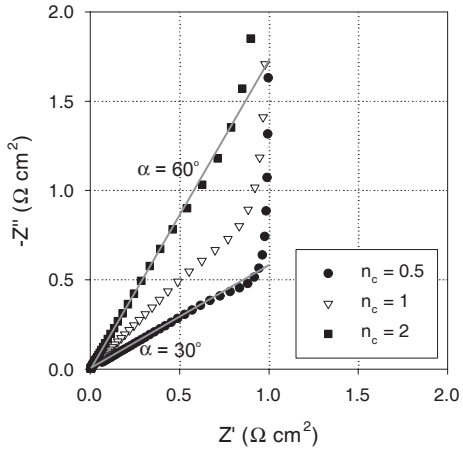

Figure 2.22: Nyquist plot of power law transmission line model as function of power factor n_c showing the relation between phase angle and power factor

[5] H. J. Oh, J. H. Lee, H. J. Ahn, Y. Jeong, Y. J. Kim, and C. S. Chi. Nanoporous activated carbon cloth for capacitive deionization of aqueous solution. *Thin Solid Films*, 515(1):220–225, 2006.

[6] M. W. Ryoo, J. H. Kim, and G. Seo. Role of titania incorporated on activated carbon cloth for capacitive deionization of NaCl solution. *Journal of Colloid and Interface Science*, 264(2):414–419, 2003.

[7] X. Z. Wang, M. G. Li, Y. W. Chen, R. M. Cheng, S. M. Huang, L. K. Pan, and Z. Sun. Electrosorption of NaCl solutions with carbon nanotubes and nanofibers composite film electrodes. *Electrochemical and Solid-State Letters*, 9(9):E23–E26, 2006.

[8] J. C. Farmer, S. M. Bahowick, J. E. Harrar, D. V. Fix, R. E. Martinelli, A. K. Vu, and K. L. Carroll. Electrosorption of chromium ions on carbon aerogel electrodes as a means of remediating ground water. *Energy & Fuels*, 11(2):337–347, 1997.

[9] C. J. Gabelich, T. D. Tran, and I. H. Suffet. Electrosorption of inorganic salts from aqueous solution using carbon aerogels. *Environmental Science & Technology*, 36(13):3010–3019, 2002.

[10] H. H. Jung, S. W. Hwang, and S. H. Hyun. Capacitive deionization characteristics of nanostructured carbon aerogel electrodes synthesized via ambient drying. *Desalination*, 216(1-3):377, 2007.

[11] P. Rana-Madaria, M. Nagarajan, C. Rajagopal, and B. S. Garg. Removal of chromium from aqueous solutions by treatment with carbon aerogel electrodes using response surface methodology. *Industrial & Engineering Chemistry Research*, 44(17):6549–6559, 2005.

[12] P. Xu, J. E. Drewes, and D. Heil. Treatment of brackish produced water using carbon aerogel-based capacitive deionization technology. *Water Research*, 42(10-11):2605, 2008.

[13] C. M. Yang, W. H. Choi, and B. K. Na. Capacitive deionization of NaCl solution with carbon aerogel-silica gel composite electrodes. *Desalination*, 174(2):125–133, 2005.

[14] T. Y. Ying, K. L. Yang, S. Yiacoumi, and C. Tsouris. Electrosorption of ions from aqueous solutions by nanostructured carbon aerogel. *Journal of Colloid and Interface Science*, 250(1):18–27, 2002.

[15] K. L. Yang, T. Y. Ying, and S. Yiacoumi. Electrosorption of ions from aqueous solutions by carbon aerogel: An electrical double-layer model. *Langmuir*, 17(6):1961–1969, 2001.

[16] J. C. Farmer, D. V. Fix, and G. V. Mack. Capacitive deionization of NaCl and $NaNO_3$ solutions with carbon aerogel electrodes. *Journal of the Electrochemical Society*, 143(1):159–169, 1996.

[17] J. C. Farmer, D. V. Fix, and G. V. Mack. Capacitive deionization of NH_4ClO_4 solutions with carbon aerogel electrodes. *Journal of Applied Electrochemistry*, 26(10):1007–1018, 1996.

[18] E. Frackowiak and F. Beguin. Carbon materials for the electrochemical storage of energy in capacitors. *Carbon*, 39(6):937–950, 2001.

[19] C. Kim. Electrochemical characterization of electrospun activated carbon nanofibres as an electrode in supercapacitors. *Journal of Power Sources*, 142(1-2):382–388, 2005.

[20] R. Saliger, U. Fischer, and C. Herta. High surface area carbon aerogels for supercapacitors. *Journal of Non-Crystalline Solids*, 225(1):81–85, 1998.

[21] J. Gamby, P. L. Taberna, P. Simon, J. F. Fauvarque, and M. Chesneau. Studies and characterisations of various activated carbons used for carbon/carbon supercapacitors. *Journal of Power Sources*, 101(1):109–116, 2001.

[22] K. L. Yang, S. Yiacoumi, and C. Tsouris. Electrosorption capacitance of nanostructured carbon aerogel obtained by cyclic voltammetry. *Journal of Electroanalytical Chemistry*, 540:159–167, 2003.

[23] E. Barsoukov and Macdonald J. R. *Impedance Spectroscopy.* Wiley, Hoboken, New Jersey, 2nd edition, 2005.

[24] C. Portet, P. L. Taberna, P. Simon, and C. Laberty-Robert. Modification of Al current collector surface by sol-gel deposit for carbon-carbon supercapacitor applications. *Electrochimica Acta*, 49(6):905–912, 2004.

[25] C. H. Hsu and F. Mansfeld. Technical note: concerning the conversion of the constant phase element parameter y0 into a capacitance. *Corrosion*, 57(9):747–748, 2001.

[26] J. Newman and K. E. Thomas-Alyea. *Electrochemical Systems.* John Wiley & Sons, Hoboken, 3rd edition, 2004.

[27] Y. R. Nian and H. S. Teng. Influence of surface oxides on the impedance behavior of carbon based electrochemical capacitors. *Journal of Electroanalytical Chemistry*, 540:119–127, 2003.

[28] H. Keiser, K. D. Beccu, and M. A. Gutjahr. Evaluation of pore structure of porous-electrodes using measurements of impedance. *Electrochimica Acta*, 21(8):539–543, 1976.

[29] C. L. Liu, W. S. Dong, and G. P. Cao. Influence of KOH followed by oxidation pretreatment on the electrochemical performance of phenolic based activated carbon fibers. *Journal of Electroanalytical Chemistry*, 611(1-2):225, 2007.

[30] M. Toupin, D. Belanger, and I. R. Hill. Performance of experimental carbon blacks in aqueous supercapacitors. *Journal of Power Sources*, 140(1):203–210, 2005.

[31] B. Kastening, M. Hahn, B. Rabanus, M. Heins, and U. zumFelde. Electronic properties and double layer of activated carbon. *Electrochimica Acta*, 42(18):2789–2799, 1997.

[32] R. J. Latham, S. E. Rowlands, and W. S. Schlindwein. Supercapacitors using polymer electrolytes based on poly(urethane). *Solid State Ionics*, 147(3-4):243–248, 2002.

[33] R. de Levie. On porous electrodes in electrolyte solutions: I. Capacitance effects. *Electrochimica Acta*, 8(10):751, 1963.

[34] G. J. Brug, A. L. G. van den Eeden, and M. Sluyters-Rehbach. The analysis of electrode impedances complicated by the presence of a constant phase element. *Journal of Electroanalytical Chemistry*, 176(1-2):275, 1984.

[35] T. F. Coleman and Y. Y. Li. An interior trust region approach for nonlinear minimization subject to bounds. *Siam Journal On Optimization*, 6(2):418–445, 1996.

[36] A.J. Bard and L.R. Faulkner. *Electrochemical Methods: Fundamentals and Applications*. Wiley, New York, 2nd edition, 2001.

[37] R. de Levie. On porous electrodes in electrolyte solutions: IV. *Electrochimica Acta*, 9(9):1231, 1964.

[38] K. Kinoshita. *Carbon, Electrochemical and physicochemical properties*. Wiley Interscience, New York, 1st edition, 1987.

[39] B. Arfken and H. J. Weber. *Mathematical Methods for Physicists*. Academic Press, London, 5th edition, 2001.

Chapter 3

Application of double-layer theory to model the dependency of electrochemical capacitance on operational parameters

3.1 Summary

The relation between electrochemical capacitance and operational parameters (temperature, electrolyte concentration and cell voltage) was investigated, and related to the Gouy-Chapman-Stern double-layer model. In this model, the Helmholtz layer capacitance and the temperature dependency of the dielectric constant in the Helmholtz layer capacitance were considered as an unknown. The relation between electrochemical capacitance and operational parameters was found to be in close agreement with the double-layer model. For the Helmholtz double-layer capacitance a value of $28 \pm 1\ \mu F\ cm^{-2}$ was found, and a relative change in dielectric constant of a factor $-24 \pm 4 \cdot 10^{-3}$ per degree Kelvin deviation from 298.15 K. The double-layer model is valid for carbon fiber as well as for carbon powder materials. The double-layer model was used to obtain the amount of double-layer area per weight of carbon electrode for the used carbon, independent of concentration, temperature and cell voltage. The amount of double-layer area per weight of carbon electrode is an independent performance parameter for carbon powder and carbon fiber electrodes.

3.2 Introduction

In the previous chapter, a method to characterize Capacitive Deionization (CDI) electrodes with electrochemical techniques is presented. This method produces characteristics of a CDI electrode in terms of resistance and capacitance. However, these characteristics are only valid for the experimental conditions of the characterization experiment. Therefore the dependency of resistance and capacitance on operational parameters such as electrolyte concentration, temperature and cell voltage has also to be investigated. In this chapter, the focus is on the dependency of capacitance

van Limpt, B., Bruning, H., Rulkens, W.H.

on operational parameters, in chapter 4 the dependency of resistance on operational parameters is investigated.

The amount of charge generated on the surface of the electrode can be predicted by double-layer theory [1], which is dependent on temperature, concentration and cell voltage. In literature, various models are used to treat the double-layer in CDI systems, such as the GC (Gouy-Chapman) model [2] and the GCSG (Gouy-Chapman-Stern-Grahame) model [3]. These models shown reasonable agreement with experimental data, and are able to predict the dependency of capacitance, and thus deionization capacity, on concentration and cell voltage. To our knowledge, double-layer dependency on temperature for CDI systems has never been investigated.

In this work, the GCS (Gouy-Chapman-Stern) double-layer model is considered, since less assumptions are needed than in the GCSG model, and the GCS model is a more accurate description of the double-layer than the GC model [1]. In the GCS model we consider the Helmholtz layer capacity as a parameter to be determined, since no unique value for the Helmholtz capacity in literature was found, other than that the value is expected to be in the range of $5 - 40\ \mu F\ cm^{-2}$ [4]. Furthermore, we consider the temperature dependency of the dielectric constant in the Helmholtz capacity as a parameter to be determined. No literature was found regarding the temperature dependency of the Helmholtz capacity.

The objective of this chapter is to investigate the dependency of electrode capacity in CDI systems on operational parameters, and assess whether the GCS model is an accurate representation of these dependencies. If this is confirmed, the GCS model can in turn be used to predict deionization capacity of a certain electrode as function of operational parameters.

To achieve this objective, electrolyte concentrations ranging from 1 mM to 1 M NaCl were investigated, electrolyte temperatures ranging from 278 K to 318 K, and cell voltages from 0 to 1.4 V. These results were related to the GCS double-layer model, where a fitting procedure was used to obtain a value for the capacity of the Helmholtz layer and the temperature dependency of this capacity. Validation is performed by comparing the obtained Helmholtz layer capacity to the expected range of $5 - 40\ \mu F\ cm^{-2}$ found in literature [3–8], and comparing the temperature dependency of the Helmholtz layer dielectric constant to the temperature dependency of the diffuse layer dielectric constant, which is known from literature [9]. Furthermore, to investigate whether the constructed GCS double-layer model is also valid for other carbon materials, the model is applied to the powder and aerogel data from chapter 2.

3.3 Theory

3.3.1 Double-layer model

Figure 3.1 shows a presentation of the double-layer model according to the GCS theory. As shown in this figure, the double-layer model consists of two parts, the Helmholtz layer and the diffuse layer. The amount of charge stored in the Helmholtz layer is equal to the amount of charge stored in the diffuse layer, while the bulk solution remains neutral in charge.

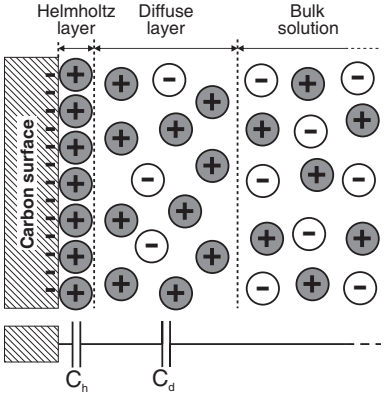

Figure 3.1: Presentation Gouy-Chapman-Stern double-layer model

Equation (3.1) shows the overall capacity of the double-layer C_{dl} in $F\ cm^{-2}$.

$$\frac{1}{C_{dl}} = \frac{1}{C_h} + \frac{1}{C_d} \tag{3.1}$$

In this equation, C_h is the Helmholtz capacity, and C_d is the diffuse layer capacity, both in $F\,cm^{-2}$. For the Helmholtz layer, the capacity is expressed as equation (3.2) [1].

$$C_h = \frac{\epsilon_h \epsilon_0}{d_h} \tag{3.2}$$

In this equation, ϵ_h is the dielectric constant of the Helmholtz layer, ϵ_0 is the vacuum permittivity ($8.854 \cdot 10^{-14}\ F\ cm^{-1}$) and d_h the thickness of the Helmholtz layer in cm. Little literature data is known on values of d_h and ϵ_h. Therefore, C_h is treated as a constant that will be obtained from the concentration dependency of electrode capacity. In comparison of experimental data with the model, ϵ_h is fitted instead of C_h. For d_h, one unique value of $6.71 \cdot 10^{-8}\ cm$ is used for all experiments at fixed absolute temperature T, based on the average thickness of a monolayer of

adsorbed Na^+ and Cl^- ions [5]. Various literature sources [4, 5, 10] report a value of $C_h = 20\ \mu F\ cm^{-2}$. This value is also used in existing double-layer modeling [3, 6, 7].

For the diffuse layer, the capacity is expressed as equation (3.3).

$$C_d = \frac{\epsilon_d \epsilon_0}{\lambda} \cosh\left(\frac{zFE_d}{2\,RT}\right) \tag{3.3}$$

$$\lambda = \sqrt{\frac{\epsilon_d \epsilon_0 RT}{2\,z^2 F^2 c}} \tag{3.4}$$

In this equation, ϵ_d is the dielectric constant for the diffuse layer, λ is the Debye length in cm, and expressed in equation (3.4), c is the electrolyte concentration in $mol\,cm^{-3}$, z is the valence charge number of the adsorbing ion, R is the gas constant ($8.3145\ J\ mol^{-1}\ K^{-1}$), F is the Faraday constant ($96485.3\ C\ mol^{-1}$), T is the temperature in K, and E_d is the potential drop over the diffuse layer in V.

The value for E_d is unknown, but can be obtained using the known potential drop over the double-layer E_{dl} in V. Since electrochemical impedance spectroscopy (EIS) measurements are always performed at a steady state, and since the electrode configuration is symmetrical, E_{dl} is equal to half of the cell voltage E_{cell}. Furthermore, E_{dl} is equal to E_d plus E_h. These relations are shown in equation (3.5).

$$E_{dl} = \frac{1}{2}E_{cell} = E_h + E_d \tag{3.5}$$

Since the Helmholtz layer and diffuse layer are effectively two capacitors in series, charge conservation requires equation (3.6) [1]. Since Helmholtz capacity is not potential dependent, Helmholtz charge Q_h in $C\ cm^{-2}$ is expressed as equation (3.7). Diffuse-layer capacity is potential dependent, therefore C_d is integrated between 0 and E_d, as shown in equation (3.8). The result of this integration is shown in equation (3.9).

$$Q_h = Q_d \tag{3.6}$$

$$Q_h = E_h C_h \tag{3.7}$$

$$Q_d = \int_0^{E_d} C_d\, dE_d \tag{3.8}$$

$$Q_d = \frac{2\,\epsilon_d \epsilon_0 RT \sinh\left(\frac{zFE_d}{2\,RT}\right)}{\lambda z F} \tag{3.9}$$

From equation (3.3) through equation (3.9) E_d and E_h are calculated as a function of E_{cell}. These potentials are inserted into equations (3.3) and (3.2) to obtain respectively C_d and C_h, which is transformed into the total double-layer capacity C_{dl} using equation (3.1).

3.3.2 Dielectric constants

To obtain the complete GCS double-layer model, the dielectric constants of the double-layer model are needed, and the temperature dependency of these dielectric constants. For temperature dependency, all dielectric constants will be related to their respective value at standard temperature $T_s = 298.15\ K$.

The dielectric constant for the diffuse layer is assumed to be equal to the dielectric constant of water ($\epsilon_{d,T=T_s} = 78.4$ [11]), since C_d only has an effect on C_{dl} at low concentrations, and at these low concentrations ϵ_d is equal to the dielectric constant of water [12]. By using the dielectric constant of water, the change in ϵ_d with temperature can be obtained. The relation between the dielectric constant of water and temperature at atmospheric pressure is obtained from a linearization of literature data [9] and shown in equation (3.10).

$$\epsilon_d = 78.44 - 0.362\,\Delta T \tag{3.10}$$

In this equation, ΔT is the temperature difference between T_s and the experimental temperature, for a ΔT of -20 through 20 K.

Since ϵ_d is affected by temperature, ϵ_h is also expected to be affected by temperature. However, no literature exists describing the temperature dependency of ϵ_h. Therefore it is assumed that ϵ_h follows a similar temperature dependency as ϵ_d, as is shown in equation (3.11).

$$\epsilon_h = \epsilon_{h,T=T_s} + k_{\epsilon,h}\Delta T \tag{3.11}$$

In this equation, $\epsilon_{h,T=T_s}$ is the dielectric constant of the Helmholtz layer at T_s, and $k_{\epsilon,h}$ is the change in ϵ_h per K relative to T_s. The value for $k_{\epsilon,h}$ is obtained from the temperature dependency of the electrode capacity. The relative change in $\epsilon_{h,T=T_s}$ is assumed to be comparable to the relative change in $\epsilon_{d,T=T_s}$, which is 0.5 % K^{-1} (equation (3.10)).

3.3.3 Link capacity to double-layer theory

Double-layer theory describes the capacity of an ideally flat single electrode. However, using the procedures as presented in chapter 2, instead the total capacity C_c is obtained, which is expressed in F per square centimeter cell area. To relate electrode capacity to double-layer capacity, the specific double-layer area S is defined, in $m^2\ g^{-1}$ activated carbon, according to equation (3.12).

$$S = \frac{4\,C_c}{1 \cdot 10^4\,C_{dl}\rho_{c,A}} \tag{3.12}$$

In this equation, $\rho_{c,A}$ is the carbon surface density, the weight of activated carbon per unit surface cell area in $g\ cm^{-2}$. The factor four is present since double-layer theory describes the capacity of a single electrode. A single electrode has half the amount of carbon, and therefore has a factor two higher capacity based on activated carbon weight. Furthermore, the amount of charge stored in both electrodes is equal, but the potential drop over the electrodes is half the cell voltage E_{cell}. Therefore, a single electrode has a factor two higher capacity [1]. The factor $1 \cdot 10^4$ results from the conversion of the unit of C_{dl} into $F\ m^{-2}$.

3.4 Materials and methods

3.4.1 Experimental setup

All experiments were performed with the characterization setup as described in chapter 1.

The investigated electrode material was a carbon felt material "FT 300-15" from Kuraray Chemical Co., Osaka, Japan. The BET surface area of the material was 1270 $m^2 g^{-1}$ (obtained from chapter 5) and the thickness d_c 1 mm. The carbon surface density $\rho_{c,A}$ of the carbon samples varied, the average density was $36 \pm 3\ mg\ cm^{-2}$. The insulating spacer material was a glass fiber filter material (Millipore AP20, 380 μm thick with binder resin). The cell configuration was held together by an external polytetrafluoroethylene (PTFE) frame and polyamide screws.

Three identical CDI cells were constructed, one cell was used for temperature experiments, one for concentration experiments and one for cell voltage experiments.

3.4.2 Experiments

For the concentration dependency, 7 different electrolyte concentrations were investigated; 1, 0.5, 0.1, 0.05, 0.01, 0.005 and 0.001 M NaCl at 298.15 K. For the temperature dependency, 5 different electrolyte temperatures were investigated; 278, 288, 298, 308 and 318 K at 0.1 M NaCl electrolyte concentration. For cell voltage dependency, the FT 300-15 fiber data as presented in chapter 2 was used. In all experiments, temperature and conductivity were constantly measured and the average value used to obtain exact electrolyte temperature and concentration.

For concentration and temperature dependency, the experiments performed on the cell for each concentration and each temperature are summarized in table 3.1.

The potentiometry experiments (A and C) were performed at a constant charge / discharge current density of 0.28 $mA\ cm^{-2}$ (which is a current of 10 mA for the entire cell) within two different cell voltages. When one cell voltage was reached, the

Table 3.1: Experiments performed for each concentration and each temperature, in chronological order

Experiment	Method	Cell voltage (V)
A	Potentiometry	From 1.2 to -1.2
B	EIS	0
C	Potentiometry	From 0.6 to -0.6
D	EIS	0

current was reversed until the other cell voltage was reached. For each potentiometry experiment, at least four charge / discharge cycles were performed to ensure a steady-state result. During the potentiometry experiments the electrolyte solution was stirred at 300 rpm to reduce local pH and conductivity changes, and purged with nitrogen to prevent oxygen and carbon dioxide from dissolving into the water (see also chapter 2).

The EIS experiments (B and D) were performed at a cell voltage of 0 V with an amplitude of 5 mV and a frequency range of 100 kHz through 0.5 mHz. During the EIS experiments nitrogen was flushed through the headspace of the reactor to prevent oxygen and carbon dioxide from dissolving into the electrolyte. The electrolyte solution was not stirred during the experiment, since the EIS measurement depends on diffusion limitation. Two EIS measurements were performed to ensure reproducibility.

Between the first EIS experiment (B) and the second potentiometry experiment (C) the electrolyte was renewed to attain the same electrolyte conditions for both potentiometry experiments.

By investigating three different voltages (0, 0.6 and 1.2 V), correlation between potential and temperature / concentration dependency can be investigated.

3.4.3 Fitting procedure

In the fitting procedure three data sets are recognized. The first contains data on the dependency of C_c on cell voltage, taken from chapter 2. The second contains data on the dependency of C_c on concentration, and the third contains data on the dependency of C_c on temperature. All data sets were fitted simultaneously using the GCS double-layer model, to obtain a unique value for C_h and for $k_{\epsilon,h}$. However, for each data set a separate value for S was obtained, to account for differences between samples. Therefore in total five independent fitting parameters were used.

The fitting was performed by a nonlinear least-squares fitting procedure in Matlab (The MathWorks Inc., USA), the target function to be minimized follows from equation (3.12) and is depicted in equation (3.13)

$$\sum_{n=1}^{3}\left[\left(\frac{C_c}{\rho_{c,A}}-\frac{C_{dl}S_n}{4}\right)^2\right] \tag{3.13}$$

In this equation, S_n is the specific double-layer area S of each data set n. The procedure calculates the double-layer capacitance C_{dl} belonging to the experimental conditions of a certain total capacitance measurement C_c. Equation (3.13) is minimized by varying the values for double-layer parameters C_h and $k_{\epsilon,h}$, and double-layer surface areas S_n.

3.4.4 Validation carbon powders and carbon aerogel

Results of the carbon powder and carbon aerogel material from chapter 2 were used to assess if the developed double-layer model is also valid for powder and aerogel data. For powder data, the same procedure as stated in section 3.4.2 was followed to obtain C_c as function of cell voltage (3 data points), for carbon aerogel C_c as function of cell voltage was obtained from figure 2.17 (9 data points).

3.5 Results and discussion

3.5.1 Fit results

Figure 3.2 shows the relation between measured capacity and cell voltage, together with the fit of the GCS double-layer model. This figure shows that the measured total capacity C_c increases with cell voltage E_{cell}, which deviates slightly from the trend of the GCS double-layer model fit, especially in the region between 0.3 and 1.2 V. However, measurements are still very close to the model (maximum deviation of 5 %).

Figure 3.3 shows the relation between measured capacity and electrolyte temperature, together with the fit of the GCS double-layer model. This figure shows that the measured capacity C_c decreases with temperature for all three cell voltages, which agrees perfectly with the GCS double-layer model fit. Furthermore, in this case the 0.6 V measurements do show a very good agreement with the GCS double-layer model fit.

Figure 3.4 shows the relation between measured capacity and electrolyte concentration for EIS results, together with the fit of the GCS double-layer model, and

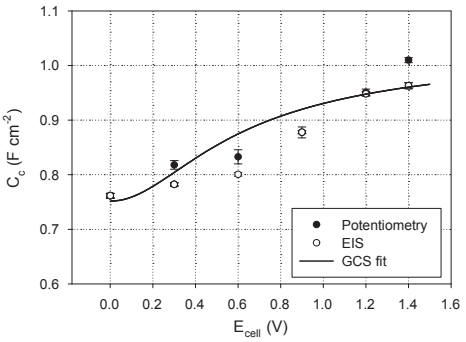

Figure 3.2: Potentiometry and EIS capacity results versus cell voltage with double-layer model fit

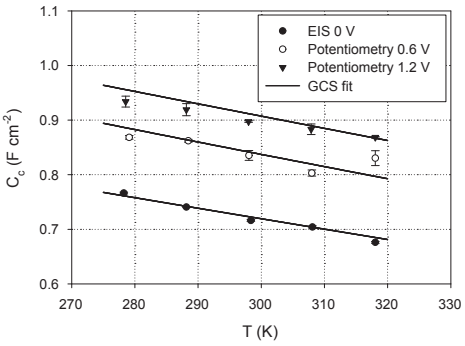

Figure 3.3: Potentiometry and EIS capacity results versus electrolyte temperature with double-layer model fit

figure 3.5 shows the relation between measured capacity and electrolyte concentration for potentiometry results, together with the fit of the GCS double-layer model for both investigated cell voltages. These figures show that measured capacity C_c decreases with concentration, and the relation between C_c and concentration c agrees reasonably with the GCS double-layer model fit. As shown in figure 3.5, for low concentration $c < 5 \cdot 10^{-6}\ mol\ cm^{-3}$ no potentiometry results could be obtained. This is because at low concentration electrolyte resistance is high, and therefore the measured voltage drop becomes very large. This has the consequence that capacity can no longer be accurately obtained. Another observation for figure 3.5 is that for a concentration of $c = 1 \cdot 10^{-3}\ mol\ cm^{-3}$ the measured C_c of the 0.6 V potentiometry experiments is higher than the measured C_c of the 1.2 V potentiometry experiment. Since the standard deviation of this measurement is relatively high, this is attributed to a measurement error.

3.5.2 Obtained double-layer parameters

In the fitting procedure, five independent fitting parameters were defined. Two fitting parameters describe the double-layer, which are the Helmholtz dielectric constant ϵ_h, and the temperature dependency of the Helmholtz dielectric constant $k_{\epsilon,h}$. The three other parameters describe the specific double-layer area S of the used electrode samples.

For the Helmholtz dielectric constant ϵ_h an overall value of 11 ± 0.5 was obtained, which corresponds according to equation (3.2) with a Helmholtz capacity C_h of $28 \pm 1\ \mu F cm^{-2}$, which is close to values used in literature [3–8]. The value for the tem-

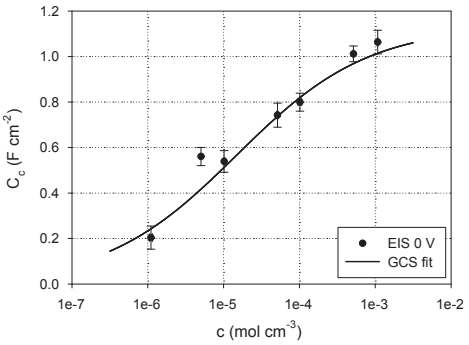

Figure 3.4: EIS capacity results versus electrolyte concentration with double-layer model fit

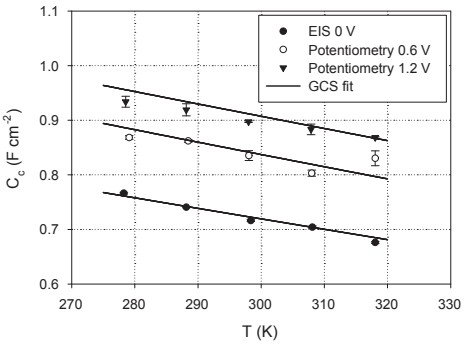

Figure 3.5: Potentiometry capacity results versus electrolyte concentration with double-layer model fit

perature dependency of the Helmholtz dielectric constant $k_{\epsilon,h}$ was $-24 \pm 4 \cdot 10^{-3}\ K^{-1}$, which is 0.25 % deviation of ϵ_h per degree deviation from T_s, which is close to the expected value of 0.5 % when taking into account that no prior knowledge on $k_{\epsilon,h}$ was available.

In table 3.2 the obtained values for the specific double-layer area S are shown for the investigated dependencies.

Table 3.2: Obtained values for the specific double-layer area S for each of the investigated dependencies

Dependency	$S\ (m^2\ g^{-1})$
Cell voltage	409 ± 15
Electrolyte temperature	431 ± 16
Electrolyte concentration	479 ± 16

As is shown in this table, the values are all equal within the variance of the data. The differences are attributed to variations in sample quality.

3.5.3 Validation carbon powders and carbon aerogel

For validation of the developed double-layer model on carbon powders and aerogel, the parameters obtained in the previous section were used, $\epsilon_h = 11 \pm 0.5$ and $k_{\epsilon,h} = -24 \pm 4 \cdot 10^{-3}\ K^{-1}$.

Figure 3.6 shows the relation between measured capacity and cell voltage for carbon powder data, together with the fit of the GCS double-layer model. The figure

shows that the measured capacity C_c increases with cell voltage, and that this relation is described accurately by the GCS double-layer model fit, the obtained value for S is $379 \pm 2\ m^2\ g^{-1}$. It must be noted that the amount of samples is limited, however all other investigated carbon powder materials showed similar relations between measured capacity and cell voltage, as will be discussed in chapter 5.

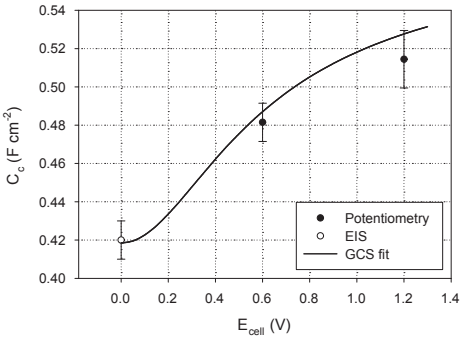

Figure 3.6: Potentiometry and EIS capacity results for carbon powder electrode versus cell voltage with double-layer model fit

Figure 3.7 shows the relation between measured capacity and cell voltage for carbon aerogel data, together with the fit of the GCS double-layer model. The figure shows that the measured capacity C_c increases exponentially with cell voltage, equal as observed with carbon powder capacity data. However, the increase with cell voltage is to a much higher extent as observed with carbon fiber capacity data. The developed double-layer model does not describe the relation between capacity and cell voltage accurately, even when fitting ϵ_h together with S on the carbon aerogel data, no accurate fit could be obtained. A study by Yang et. al. [3] confirms that a general double-layer model cannot accurately predict double-layer capacity of carbon aerogel, here it is postulated that double-layer overlap is the cause of the deviation. However, it is uncertain if this is the cause for the deviation, since double-layer overlap will also occur to some extent in carbon fiber and carbon powder materials.

3.6 Conclusion

The relation between electrochemical capacity and operational parameters (temperature, electrolyte concentration and cell voltage) can be described by GCS theory for carbon powder and carbon fiber materials. For the carbon fiber material, a reasonable

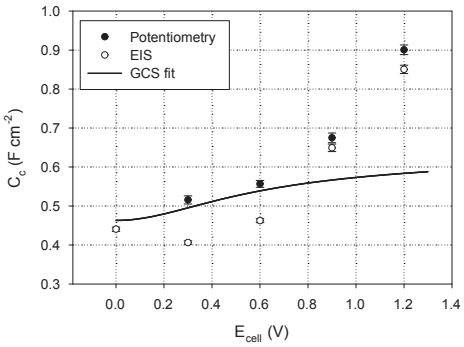

Figure 3.7: Potentiometry and EIS capacity results for carbon aerogel electrode versus cell voltage with double-layer model fit

fit with cell voltage was found, and a good fit with temperature and concentration data. Furthermore, the resulting value for Helmholtz layer capacity is in accordance with literature, and the temperature dependency of the Helmholtz layer capacity is in accordance with the temperature dependency of the diffuse layer.

The GCS double-layer model can be used to obtain specific double-layer area S of carbon fiber and carbon powder materials, as long as capacity data as function of cell voltage, concentration or temperature is available, and the carbon electrode is constructed out of carbon fiber or carbon powder. The specific double-layer area can in turn be used to predict deionization capacity as function of cell voltage, concentration and temperature. Application to carbon aerogel data was not possible, double-layer formation in carbon aerogel cannot be described with the GCS model.

Bibliography

[1] J. Newman and K. E. Thomas-Alyea. *Electrochemical Systems.* John Wiley & Sons, Hoboken, 3rd edition, 2004.

[2] T. Y. Ying, K. L. Yang, S. Yiacoumi, and C. Tsouris. Electrosorption of ions from aqueous solutions by nanostructured carbon aerogel. *Journal of Colloid and Interface Science*, 250(1):18–27, 2002.

[3] K. L. Yang, T. Y. Ying, and S. Yiacoumi. Electrosorption of ions from aqueous solutions by carbon aerogel: An electrical double-layer model. *Langmuir*, 17(6):1961–1969, 2001.

[4] K. Kinoshita. *Carbon, Electrochemical and physicochemical properties.* Wiley Interscience, New York, 1st edition, 1987.

[5] B. E. Conway. *Electrochemical Supercapacitors, Scientific Funcamentals and Techno-*

logical Applications. Kluwer Academic / Plenum Publishers, New York, 1st edition, 1999.

[6] H. Gerischer. An interpretation of the double layer capacity of graphite electrodes in relation to the density of states at the fermi level. *Journal of Physical Chemistry*, 89(20):4249–4251, 1985.

[7] M. Hahn, M. Baertschi, and O. Barbieri. Interfacial capacitance and electronic conductance of activated carbon double-layer electrodes. *Electrochem. Solid-State Lett.*, 7(2):A33–A36, 2004. 1099-0062.

[8] A. M. Johnson and J. Newman. Desalting by means of porous carbon electrodes. *Journal of the Electrochemical Society*, 118(3):510–&, 1971.

[9] D. P. Fernandez, A. R. H. Goodwin, and E. W. Lemmon. A formulation for the static permittivity of water and steam at temperatures from 238 K to 873 K at pressures up to 1200 MPa, including derivatives and debye–huckel coefficients. *Journal of Physical and Chemical Reference Data*, 26(4):1125, 1997.

[10] H. Shi. Activated carbons and double layer capacitance. *Electrochimica Acta*, 41(10):1633–1639, 1996.

[11] D. R. Lide. *CRC Handbook of Chemistry and Physics, 85th Edition*. CRC Press, 85th edition, 2004.

[12] B. E. Conway, J. O. Bockris, and I. A. Ammar. The dielectric constant of the solution in the diffuse and helmholtz double layers at a charged interface in aqueous solution. *Transactions Of The Faraday Society*, 47(7):756–766, 1951.

Chapter 4

Relations between electrolyte characteristics and electrochemical resistance

4.1 Summary

The relation between electrolyte characteristics (electrolyte temperature and concentration) and electrochemical resistance as determined by electrochemical impedance spectrometry was investigated, to obtain performance parameters independent of electrolyte characteristics. The electrochemical resistances investigated were system resistance, carbon electrode resistance and charge-transfer resistance. System resistance is linearly related to the absolute conductivity of the electrolyte, resulting in the performance parameters effective spacer thickness and a constant contact resistance. The effective spacer thickness was found to be larger than the actual spacer thickness, the constant contact resistance was equal to the measured contact resistance. Carbon electrode resistance could be proportionally related to the absolute conductivity of the electrolyte, resulting in a performance parameter describing the penetration depth of ions into the carbon electrode. Charge-transfer resistance showed an Arrhenius-like temperature dependency. However, the exact charge-transfer process could not be determined, therefore an empirical approach was used. This resulted in a charge-transfer parameter describing the performance of the charge-transfer process. Processes that limit performance can be recognized by analyzing the contribution of separate performance parameters to total resistance.

4.2 Introduction

In chapter 2, a method to characterize Capacitive Deionization (CDI) electrodes with electrochemical techniques is presented. This method produces characteristics of a CDI electrode in terms of resistance and capacitance. However, these characteristics are only valid for the experimental conditions of the characterization experiment. Therefore the dependency of resistance and capacitance on operational parameters such as electrolyte concentration, temperature and cell voltage is determined. In

van Limpt, B., Bruning, H., Rulkens, W.H.

chapter 3 it was determined that the dependency of capacitance on operational parameters can be predicted by the Gouy-Chapman-Stern theory. In this chapter, the dependency of resistance on operational parameters is investigated, in chapter 5 the dependency of resistance and capacitance on electrode characteristics is investigated.

Figure 4.1 shows the three distinct resistances in a CDI electrode configuration, as derived in chapter 2. These are the system resistance R_s, which is the spacer resistance of a CDI cell including the contact resistance between potentiostat and the current collectors, the charge-transfer resistance R_{ct}, and the resistance of the carbon electrode R_c. In chapter 2 it was verified that the resistances do not change with cell voltage, therefore only the concentration and temperature dependency of electrochemical resistance are investigated.

As observed in chapter 2, R_s and R_c are dependent on electrolyte conductivity. Both R_s and R_c can be related to the thicknesses of respectively spacer and carbon, based on the conductivity of the electrolyte. Since electrolyte conductivity is determined by electrolyte temperature as well as electrolyte concentration, the dependency of R_s and R_c on conductivity can be obtained by performing characterization experiments at various electrolyte temperatures and concentrations. The obtained dependencies are used to define performance parameters for spacer and carbon electrode, giving the ability to compare spacers and carbon electrodes independent of electrolyte concentration and temperature.

In chapter 2 we postulated that R_{ct} is related to a charge-transfer process between carbon electrode and current collector. Therefore, it is expected that R_{ct} follows an Arrhenius-like dependency on temperature and an inverse square root dependency on concentration [1]. Since it is unsure what process causes the charge-transfer resistance, an empirical relation is obtained. The obtained empirical relation is used to define a performance parameter for the charge-transfer process, giving the ability

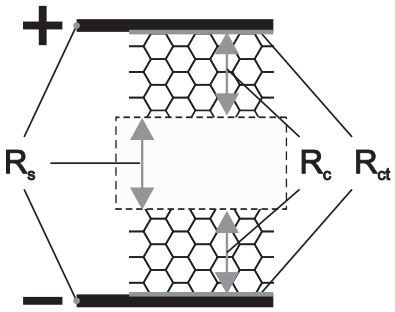

Figure 4.1: Schematic presentation of resistances present in CDI electrode configuration

to further investigate the nature of R_{ct}, independent of electrolyte concentration and temperature.

To investigate what resistance is mainly determining total resistance R_{total}, and therefore limiting the adsorption rate, an analysis is done on the relative contribution of each of the resistances toward R_{total}.

The dependencies of R_s R_c and R_{ct} on temperature and concentration were obtained by using the experimental results of the electrochemical impedance spectroscopy (EIS) experiments as performed in chapter 3. These were NaCl concentrations ranging from 1 mM to 1 M at 298 K and temperatures ranging from 278 K to 318 K at 0.1 M NaCl.

4.3 Theory

4.3.1 System resistance

Since R_s is the spacer resistance in a CDI cell, plus the contact resistance between potentiostat and current collector, a linear relation with conductivity σ in $S\ cm^{-1}$ is expected, according to equation (4.1)

$$R_s = \frac{l_s}{\sigma} + R_0 A_{cell} \tag{4.1}$$

In this equation, l_s in cm is the effective thickness of the spacer and R_0 in Ω is the contact resistance from measuring cell to potentiostat, normalized to total cell area A_{cell} in cm^2.

This relation is tested by plotting the specific electrolyte resistance (inverse conductivity) versus R_s for both temperature and concentration experiments. This should result in a linear relation according to equation (4.1). The validity can be verified by comparing l_s to the spacer thickness, and by comparing R_0 to the actual contact resistance. When l_s is equal to the spacer thickness, the performance parameter for the spacer is the actual spacer thickness. An approximation of the actual contact resistance was obtained by removing spacer and electrodes from the cell, and measuring the resistance over the resulting configuration by a multimeter (Fluke 87V True RMS Multimeter, Everett, USA).

4.3.2 Charge-transfer resistance

As already discussed in chapter 2, charge-transfer resistance R_{ct} (in $\Omega\ cm^2$) can be related to various factors, such as surface groups [2], interface resistance between current collector and carbon [3], structure of carbon pores [4], or polarization resistance

of carbon [5, 6]. This indicates that R_{ct} is a charge transfer resistance between current collector and carbon material, mainly caused by the difference in transport method between current collector and activated carbon. In activated carbon electrons are transported by hopping between electronically coherent domains [7]. This transport is influenced by the natural charge of the carbon, which in turn is influenced by electrolyte concentration and surface groups. This explanation would encompass most of the hypotheses presented in literature. We will regard R_{ct} as a general charge-transfer resistance, and based on experimental results the exact nature of R_{ct} will be determined. Since the exact mechanism of the charge-transfer process is not known, a general charge transfer reaction equation is used by using an Arrhenius approach, as shown in equation (4.2).

$$i_0 = zFk\sqrt{c} \tag{4.2}$$

This approach uses the assumption that a certain species with concentration c in $mol\ l$ is responsible for a charge transfer process with exchange current density i_0 in $A\ cm^{-2}$. It is assumed that the species responsible for the charge-transfer is the used electrolyte. In equation (4.2) z is the valence charge number of the species in question, and k is a rate constant, which is expressed as equation (4.3).

$$k = A\, e^{-\Delta U^{act}/RT} \tag{4.3}$$

In this equation, A is the Arrhenius factor and ΔU^{act} is the activation energy of the charge transfer process in $J\ mol^{-1}$. The exchange current density i_0 from equation (4.2) is inversely related to R_{ct}, as shown in equation (4.4) [1].

$$i_0 = \frac{RT}{zFR_{ct}} \tag{4.4}$$

In this equation, R is the gas constant ($8.3145\ J\ mol^{-1}\ K^{-1}$), F is the Faraday constant ($96485.3\ C\ mol^{-1}$), and T is the temperature in K.

To confirm that R_{ct} is a charge transfer resistance, dependency of R_{ct} on electrolyte temperature T is obtained by combining equations (4.2), (4.3), and (4.4) to equation (4.5).

$$\ln\left(\frac{RT}{FR_{ct}}\right) = -\frac{\Delta U^{act}}{RT} + \ln\left(z^2FA\sqrt{c}\right) \tag{4.5}$$

When obtaining R_{ct} at different electrolyte temperatures, and plotting $\ln\left(RT/FR_{ct}\right)$ versus $1/T$, the slope of this relationship should be constant and equal to $-\Delta U^{act}/R$.

Since we do not know the exact nature of the charge-transfer process, an empirical approach is used to relate R_{ct} to electrolyte concentration and temperature. To obtain

an empirical relation for the dependency of R_{ct} on concentration, equation (4.2) and (4.4) are combined to equation (4.6). This equation can be simplified to equation (4.9).

$$\frac{RT}{zFR_{ct}} = zFk\sqrt{c} \tag{4.6}$$

$$R_{ct} = \frac{RT}{zFk\sqrt{c}} \tag{4.7}$$

$$\beta = \frac{zFk}{RT} \tag{4.8}$$

$$R_{ct} = \frac{1}{\beta\sqrt{c}} \tag{4.9}$$

In equation (4.9), c is the concentration of the electrolyte in $mol\,cm^{-3}$ and β is an empirical parameter describing the relation between the activity of the reacting species and the inverse charge transfer resistance. Thereby, a higher value for β corresponds to a lower R_{ct}, giving a direct indication on the performance of the charge-transfer process.

There still exists a temperature dependency in β, as results from equation (4.8), but also from the dependency on the rate constant k (equation (4.3)). To remove the temperature dependency from β, it is assumed that β is linearly dependent on temperature between 278 K and 318 K. This redefines equation (4.9) to equation (4.10).

$$R_{ct} = \frac{1}{k_{T,ct}\Delta T + 1}\frac{1}{\beta\sqrt{c}} \tag{4.10}$$

In this equation, ΔT is the temperature difference between the actual temperature and T_s (273 K), and $k_{T,ct}$ is the temperature correction factor for the charge-transfer process.

When taking into account that $1/(\beta\sqrt{c})$ is equal to R_{ct} at T_s, equation (4.10) is rewritten as equation (4.11).

$$R_{ct} = \frac{R_{ct,T=T_s}}{k_{T,ct}\Delta T + 1} \tag{4.11}$$

By plotting the relationship R_{ct} and T equation (4.11) a constant value for $k_{T,ct}$ is obtained if this simplification is valid.

4.3.3 Resistance of carbon electrode

As discussed in chapter 2, the resistance of the carbon electrode R_c is the resistance encountered during the adsorption of ions. When no ions are stored on the carbon

electrode, this resistance is zero. When ions are being adsorbed onto sites on the surface of the carbon, first the sites that are easiest accessible are occupied. When these sites are occupied, ions have to travel further before they can be adsorbed, resulting in an increasing resistance. R_c is defined as the resistance encountered by ions during the adsorption process just before all sites are occupied. This is not necessarily equal to the maximum resistance encountered for ions to reach the least accessible site on the carbon surface, as discussed in chapter 2.

By relating R_c to the conductivity of the electrolyte, the penetration depth l_c is obtained [8]. This relationship is shown in equation (4.12).

$$R_c = \frac{l_c}{\sigma} \tag{4.12}$$

In this equation, σ^{-1} is the electrolyte resistivity in $\Omega\, cm$, and l_c is the penetration depth in cm. To obtain l_c, R_c is plotted versus the electrolyte resistivity $1/\sigma$, which changes as function of both temperature and concentration. The slope of this relationship is equal to l_c, and should be equal for the temperature dependency as for the concentration dependency.

4.4 Results and discussion

4.4.1 System resistance

Figure 4.2 shows the relation between system resistance R_s and electrolyte resistivity σ^{-1}, where σ^{-1} was varied by changing the electrolyte concentration (concentration dependency).

Figure 4.3 shows the relation between system resistance R_s and electrolyte resistivity σ^{-1}, where σ^{-1} was varied by changing the electrolyte temperature (temperature dependency).

Both figures show that the relation between R_s and specific electrolyte resistance is linear, in good agreement with equation (4.1). The obtained parameter values from the linear regression are shown in table 4.1.

Table 4.1: Derived effective spacer thickness l_s and contact resistance R_0 from the concentration and temperature dependency of system resistance

Dependency	l_s (μm)	R_0 (Ω)
Concentration	560 ± 30	0.18 ± 0.03
Temperature	630 ± 30	0.13 ± 0.01

As shown in this table, concentration and temperature dependency show equal

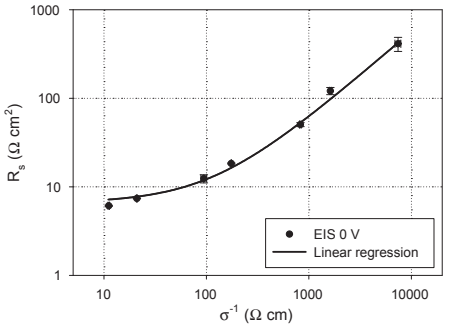

Figure 4.2: System resistance versus specific electrolyte resistance, concentration dependency, with linear regression

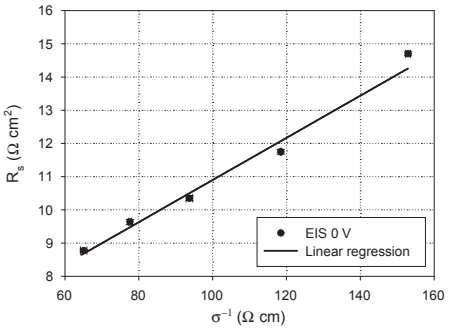

Figure 4.3: System resistance versus specific electrolyte resistance, temperature dependency, with linear regression

results for l_s and R_0. Differences are attributed to differences in cell construction. Values for R_0 are in the range of the measured contact resistance (0.15 Ω). Values for l_s are much higher than the actual spacer thickness (380 μm). This is most likely due to the porosity of the spacer, which increases the effective resistance due to a shadow effect [9].

4.4.2 Charge transfer resistance

Figure 4.4 shows the relation between charge-transfer resistance R_{ct} and electrolyte concentration c. From the inverse square root regression of this relation, a value for β is obtained using equation (4.9). As shown in this figure, the proposed empirical relation agrees to a high degree with the experimental data. For charge-transfer performance β a value of 13.2 ± 0.9 was found.

Figure 4.5 shows the Arrhenius analysis of the relation between charge-transfer resistance R_{ct} and electrolyte temperature T according to equation (4.5). As is shown in this figure, the proposed Arrhenius approach describes the experimental data in a good manner. Therefore it can be confirmed that R_{ct} is indeed a charge transfer resistance.

Figure 4.6 shows the normalized relation between charge-transfer resistance R_{ct} and electrolyte temperature T. From the linear regression of this relation, a value for the temperature correction factor for the charge transfer process, $k_{T,ct}$, is obtained using equation (4.11).

As shown in this figure, the proposed empirical relation agrees to a high degree with the experimental data. For charge-transfer performance β a value of 25 ± 2 was found, which is about twice as high than the charge-transfer performance as found

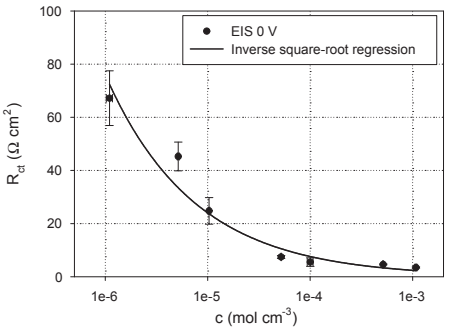

Figure 4.4: Charge transfer resistance versus concentration with inverse square root regression

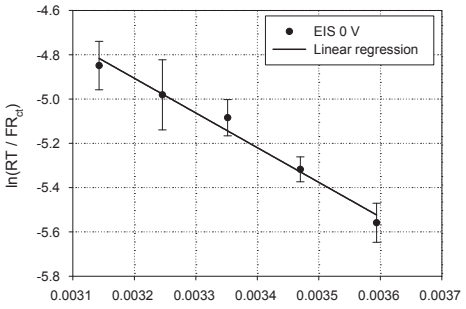

Figure 4.5: Arrhenius analysis of temperature dependency charge transfer resistance

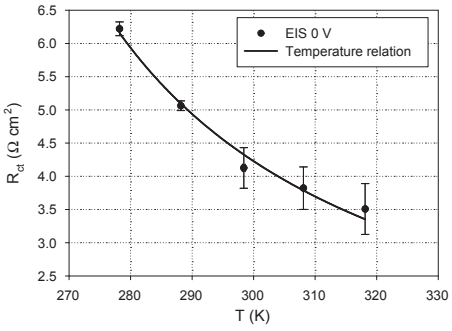

Figure 4.6: Normalized results temperature relation charge transfer resistance with linear regression

for the concentration relation. For $k_{T,ct}$ a value of $0.015 \pm 0.001\,K^{-1}$ was found. This value is close to the k_T of the NaCl electrolyte ($0.0197\,K^{-1}$ [10]). The charge-transfer performance parameter β together with an temperature correction factor $k_{T,ct}$ are used as independent performance parameters for R_{ct}.

4.4.3 Resistance of carbon electrode

Figure 4.7 shows the relation between carbon electrode resistance R_c and electrolyte resistivity σ^{-1}, where σ^{-1} was varied by changing the electrolyte concentration (concentration dependency).

Figure 4.8 shows the relation between carbon electrode resistance R_c and electrolyte resistivity σ^{-1}, where σ^{-1} was varied by changing the electrolyte temperature (temperature dependency).

Both figures show that a linear regression shows good correspondence with the

relation between R_c and specific electrolyte resistance. This is in good agreement with equation (4.12), except for high electrolyte concentrations (low σ^{-1}) where the data shows a deviation of the linear regression. This deviation indicates that at high electrolyte conductivities the carbon electrode resistance is determined by another factor, most likely the electrical resistance of the carbon.

The obtained parameter values from the linear regression are shown in table 4.2, which shows that l_c for the concentration and temperature dependency are not equal, while the used electrode material was equal. This difference is attributed to variations in sample quality, which also explains the variation in β as found in section 4.4.2. In chapter 5 the relation between l_c and electrode characteristics will be further investigated.

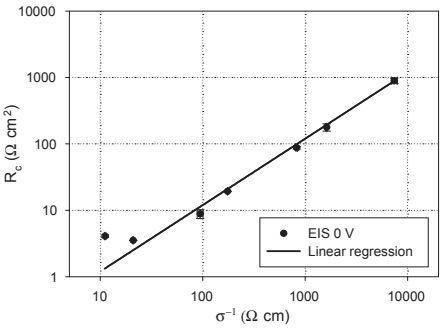

Figure 4.7: Resistance of carbon electrode versus specific electrolyte resistance, concentration dependency, with linear regression

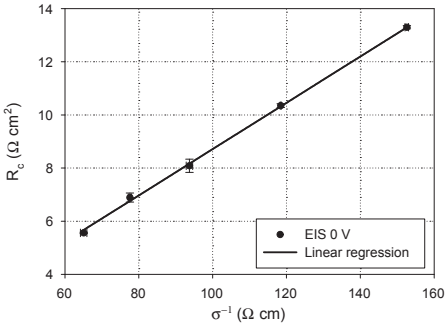

Figure 4.8: Resistance of carbon electrode versus specific electrolyte resistance, temperature dependency, with linear regression

Table 4.2: Derived ion penetration depth l_c from the concentration and temperature dependency of carbon electrode resistance

Dependency	l_c (μm)
Concentration	1120 ± 10
Temperature	871 ± 4

4.4.4 Contribution to total resistance

For calculation of the contribution of performance parameters to total resistance R_{total}, the performance parameters as summarized in table 4.3 were used. These are averages of the performance parameters found in this chapter.

Table 4.3: Used performance parameters for calculation of the relative contribution to total resistance

Parameter	Value	Unit
l_s	250	μm
l_c	995	μm
β	19.1	-
R_0	0.15	Ω

All these performance parameters correspond with certain resistance values as function of temperature and concentration. The sum of all these resistances is the total resistance R_{total}, as discussed in chapter 2. Since each of the separate performance parameters has a different relation with temperature and concentration, also the relative contribution of the performance parameters to R_{total} changes with temperature and concentration.

Figure 4.9 shows the stacked relative contribution of the performance parameters to the total resistance R_{total} as function of concentration, at an electrolyte temperature of 298 K.

Figure 4.10 shows the stacked relative contribution of the performance parameters to the total resistance R_{total} as function of temperature, at an electrolyte concentration of $1 \cdot 10^{-4}$ $mol\ cm^{-3}$.

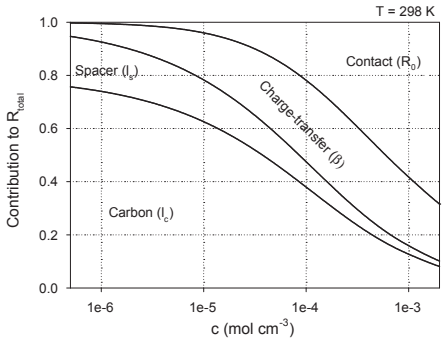

Figure 4.9: Stacked relative contribution of the performance parameters to total resistance as function of concentration

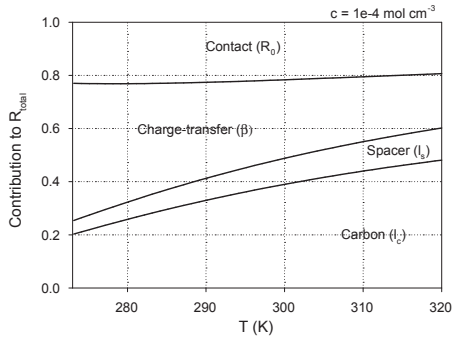

Figure 4.10: Stacked relative contribution of the performance parameters to total resistance as function of temperature

As shown in figure 4.9, the contribution of ion penetration depth l_c and contact resistance R_0 are most relevant in determining R_{total} at varying concentration. At low concentrations ($c < 1 \cdot 10^{-4}$ $mol\ cm^{-3}$), l_c is mostly determining R_{total}, and therefore the deionization rate is limited by the resistance of the carbon electrode.

At high concentrations ($c > 1 \cdot 10^{-4}$ mol cm^{-3}), R_0 is mostly determining R_{total}, and therefore the deionization rate is limited by the contact resistance between cell and power supply. At $c \approx 1 \cdot 10^{-4}$ mol cm^{-3} the contributions of β, l_c and R_0 are balanced, meaning that at this concentration the cell gives optimal performance; none of the performance parameters are limiting.

As shown in figure 4.10, the contribution of ion penetration depth l_c and charge transfer performance β are most relevant in determining R_{total} at varying temperature. At low temperatures ($T < 290$ K), β is mostly determining R_{total}, and therefore the deionization rate is limited by the charge-transfer process. At high temperatures ($T > 290K$), l_c is mostly determining R_{total}, and therefore the deionization rate is limited by the resistance of the carbon electrode. At $T \approx 290$ K the contributions of β and l_c are balanced, meaning that at this temperature the cell gives optimal performance; none of the performance parameters are limiting.

The analysis of limiting contribution to R_{total} can be used to optimize a certain cell design. When one performance parameter is limiting, the process belonging to the performance parameter has to be improved until the contribution of all performance parameters to R_{total} are approximately equal. This results in an optimal design of the cell for a specific electrolyte concentration and temperature.

4.5 Conclusion

The following relations between electrode performance parameters and electrode characteristics were obtained.

System resistance R_s is linearly related to the absolute electrolyte conductivity by an effective spacer thickness l_s, plus a certain constant contact resistance R_0. The value for l_s was found to differ from the actual spacer thickness, most likely due to a shadow effect caused by the porosity of the spacer. The effective spacer thickness together with a constant contact resistance is considered an independent performance parameter for R_s.

Resistance of the carbon electrode R_c is proportionally related to the absolute electrolyte conductivity by a penetration depth l_c of the electrode.

Charge-transfer resistance R_{ct} is caused by an unknown charge-transfer process. By following an Arrhenius approach, R_{ct} could be related to electrolyte concentration and temperature. Based on this relation, an empirical charge-transfer parameter β can be defined, which together with an temperature correction factor $k_{T,ct}$ is considered an independent performance parameter for R_{ct}. For the temperature dependency a different value for the charge-transfer parameter β was found than for the concentration dependency, perhaps due to differences in sample quality. Further investigations

are needed to determine the exact nature of β.

The obtained performance parameters penetration depth l_c and the empirical charge-transfer parameter β are determined by the characteristics of the electrode. Therefore in chapter 5 the dependency of these parameters is investigated on electrode characteristics such as electrode thickness and type of carbon used in the manufacture of the electrode.

By analyzing the contribution of the performance parameters to the total resistance R_{total}, limiting processes can be defined. By subsequently improving these processes, an optimal design can be obtained.

Bibliography

[1] E. Barsoukov and Macdonald J. R. *Impedance Spectroscopy.* Wiley, Hoboken, New Jersey, 2nd edition, 2005.

[2] Y. R. Nian and H. S. Teng. Influence of surface oxides on the impedance behavior of carbon based electrochemical capacitors. *Journal of Electroanalytical Chemistry*, 540:119–127, 2003.

[3] C. Portet, P. L. Taberna, P. Simon, and C. Laberty-Robert. Modification of Al current collector surface by sol-gel deposit for carbon-carbon supercapacitor applications. *Electrochimica Acta*, 49(6):905–912, 2004.

[4] H. Keiser, K. D. Beccu, and M. A. Gutjahr. Evaluation of pore structure of porous-electrodes using measurements of impedance. *Electrochimica Acta*, 21(8):539–543, 1976.

[5] C. L. Liu, W. S. Dong, and G. P. Cao. Influence of KOH followed by oxidation pretreatment on the electrochemical performance of phenolic based activated carbon fibers. *Journal of Electroanalytical Chemistry*, 611(1-2):225, 2007.

[6] M. Toupin, D. Belanger, and I. R. Hill. Performance of experimental carbon blacks in aqueous supercapacitors. *Journal of Power Sources*, 140(1):203–210, 2005.

[7] B. Kastening, M. Hahn, B. Rabanus, M. Heins, and U. zumFelde. Electronic properties and double layer of activated carbon. *Electrochimica Acta*, 42(18):2789–2799, 1997.

[8] R. de Levie. On porous electrodes in electrolyte solutions: IV. *Electrochimica Acta*, 9(9):1231, 1964.

[9] P. Długołęcki, A. Gambier, K. Nijmeijer, and M. Wessling. Practical potential of reverse electrodialysis as process for sustainable energy generation. *Environmental Science & Technology*, 43(17):6888–6894, 2009.

[10] D. R. Lide. *CRC Handbook of Chemistry and Physics, 85th Edition.* CRC Press, 85th edition, 2004.

Chapter 5

Relations between electrode performance and electrode characteristics

5.1 Summary

The relation between electrode performance and electrode characteristics was investigated by performing surface area measurements and electrochemical characterization for a wide range of carbon powders and carbon fibers. From the relation between physical surface area and specific double-layer area, it is concluded that micropore area and small mesopore area are mostly determining capacity, which agrees with literature on supercapacitors. Charge transfer on the interface between current collector and activated carbon is proportionally related to the total BET surface area of the activated carbon; a higher BET surface area will therefore enhance charge transfer. Resistance of the carbon electrode is limited by migration of ions into the separate carbon particles, and is determined by the carbon surface density. This resulted in the definition of the specific penetration depth, which was equal for all investigated carbons.

5.2 Introduction

Chapters 2 through 4 showed that the performance of a CDI carbon electrode is defined by several electrochemical characteristics, independent of operational parameters such as the concentration and temperature of the electrolyte. These characteristics are the specific double-layer area S of the carbon, in $m^2\ g^{-1}$ carbon, the charge-transfer performance β and the penetration depth l_c in cm. In this chapter, these electrochemical characteristics are related to the physical properties of the carbon electrodes.

It is widely known that surface area measurements are related to electrode capacitance and therefore to the specific double-layer area S of the electrode. These surface area measurements are obtained using various techniques, such as nitrogen adsorption [1–7], benzene adsorption [8] and X-ray scattering [3]. Using these techniques, total

van Limpt, B, Bruning, H, Rulkens, W.H.

surface area can be obtained (mostly using BET analysis), the ratio between micropores and macropores, and median pore size. In supercapacitor research it was already found that micropores are mainly responsible for generation of capacitance [2, 5, 8], and thus adsorption of ions [9]. However, some micropores can be inaccessible for adsorption of ions [3, 5]. In general, no straightforward relation exists between capacitance and either surface area or pore size distribution [5]. Another general relation found in supercapacitor research is that mesopores will decrease resistance [2, 5, 7, 8], and thus increase rate of ion adsorption.

The objective of this chapter is to investigate the relations between electrode properties and the electrochemical characteristics. This is done by investigating two different types of electrode materials, carbon fibers and carbon powders, since these materials could be characterized as shown in chapters 2 and 3. A wide range of materials from different manufacturers with different surface characteristics are selected. Electrodes are made by a custom procedure based on membrane casting, enabling us to analyze the effect of electrode thickness on performance. To obtain carbon surface properties, nitrogen adsorption experiments are performed to obtain total surface area (BET), median pore size and the ratio between micropore and macropore surface area.

For the relation between the penetration depth l_c and carbon properties, two relations are possible. When the adsorption of ions is limited by migration of ions into the separate carbon particles, then l_c should be related to the carbon weight per unit cell area $\rho_{c,A}$ in $g\ cm^{-2}$. When the adsorption of ions is limited by migration of ions from bulk electrolyte into the electrode, then l_c should be related to the thickness of the electrode. Both relations will be investigated.

For the relation between charge-transfer performance β and carbon properties, very little information from literature is available. Since β is an interface resistance [10] that is dependent on surface groups present on carbon [11], the assumption is tested that β is related to carbon surface area, since at a higher surface area a higher surface group concentration is present.

5.3 Theory

5.3.1 Relation between electrode resistance and electrode characteristics

In chapter 4 the electrode resistance R_c could be related to the ion penetration depth l_c. Since only one type of carbon was investigated, no further relations could be derived. Since l_c is related to the resistance encountered during the adsorption of

ions, two possible mechanisms for the adsorption of ions are proposed as shown in figure 5.1. The figure visualizes the ion adsorption process, starting at the left hand side of the figure with an uncharged system ($R_c = 0$) and moving to the right hand side to a fully charged system ($R_c = l_c/\sigma$). In both mechanisms, it is assumed that the contact resistance between carbon particles is negligible.

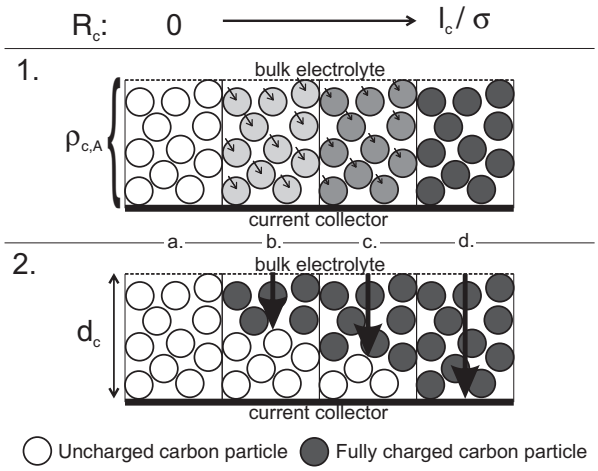

Figure 5.1: Proposed mechanisms for the adsorption process in a carbon electrode. The top section (1.) shows an adsorption process limited by migration into the carbon particles, and therefore dependent on the carbon weight per unit cell area $\rho_{c,A}$. The bottom section (2.) shows an adsorption process limited by migration into the electrode, and therefore dependent on the thickness of the electrode d_c. Letters a. trough d. chronologically indicate the change in R_c during the charging of the electrode, starting at $R_c = 0$ at position a. through $R_c = l_c/\sigma$ at position d.

The first mechanism assumes that the adsorption process is limited by migration of ions into the separate carbon particles. Initially all carbon particles are uncharged and therefore $R_c = 0$ (situation a.). When starting the adsorption process, all carbon particles adsorb ions at an equal rate (situation b.). The accumulation of ions into the separate carbon particles increases the resistance in the carbon particle, and therefore reduces the driving force for adsorption (situation c.). Finally, all carbon per unit cell area, equal to $\rho_{c,A}$, will be fully charged and therefore $R_c = l_c/\sigma$ (situation d.).

The second mechanism assumes that the adsorption process is limited by migration of ions from bulk electrolyte into the electrode. Initially all carbon particles are uncharged and therefore $R_c = 0$ (situation a.). When starting the adsorption process, the carbon particles closest to the bulk electrolyte will be charged first (situation b.). Before other carbon particles can be charged the ions have to travel some distance from the bulk electrolyte toward the next uncharged carbon particles (situation c.).

Finally, the ions have traveled a distance of d_c and reached the end of the carbon electrode, therefore all carbon particles are charged and $R_c = l_c/\sigma$.

To investigate which of the two processes is determining l_c, two relations are set up and tested experimentally.

If the penetration of ions into the separate carbon particles is determining l_c (mechanism 1), then l_c is related to the amount of carbon per unit area according to equation (5.1).

$$l_c = \lambda_c \rho_{c,A} \tag{5.1}$$

In this equation, $\rho_{c,A}$ is the carbon weight per unit cell area $g\ cm^{-2}$, and λ_c is the specific pore length of the carbon, in $cm\ g^{-1}\ cm^2$. A high specific pore length λ_c means that the ions have to travel far before the full capacity of the carbon is reached, resulting in a higher electrode resistance R_c.

If the migration of ions through the electrode is determining l_c (mechanism 2), then l_c is related to the thickness of the electrode according to equation (5.2).

$$l_c = 2\,\phi_c\,d_c \tag{5.2}$$

In this equation, the factor two is present since a cell configuration contains two electrodes, and ϕ_c is the porosity of the electrode. A high porosity means that less electrolyte is present per cubic centimeter electrode, resulting in a higher electrode resistance R_c.

5.3.2 Hypotheses performance relations

Electrode capacity / specific electrode double-layer area

When increasing electrode thickness, the carbon weight per unit cell area $\rho_{c,A}$ also increases. When relating the electrode capacity C_c in $F\ cm^{-2}$ to $\rho_{c,A}$ at increasing electrode thickness, the slope of this relationship should return a constant specific carbon capacity in $F\ g^{-1}$.

When increasing the physical surface area of a certain carbon, it is expected that the specific double-layer area of the electrode also increases. By investigating the relation between specific double-layer area S and the micro- and macropore area, it can be determined whether the micropores or macropores are responsible for generation of charge and thus adsorption of ions.

Charge-transfer performance

If charge-transfer performance describes the charge-transfer on the interface between carbon electrode and current collector, then the charge-transfer performance should be constant with increasing electrode thickness.

When increasing the physical surface area of carbon, also the density of carbon surface groups on the interface between carbon electrode and current collector is increased. Since the carbon surface groups are known to be related to charge-transfer reactions [11], a relation between physical surface area of the carbon and charge-transfer performance would indicate that the carbon surface groups in the interface are responsible for the measured charge-transfer resistance R_{ct}.

Electrode resistance / penetration depth

If the adsorption process is limited by migration of ions into the separate carbon particles (top section of figure 5.1), then only the carbon weight per unit cell area $\rho_{c,A}$ should have an effect on the measured penetration depth l_c, and the thickness of the electrode should be irrelevant.

If the obtained specific penetration depth λ_c is independent of the physical surface area of carbon, then the pore size distribution has no effect on the total resistance of the carbon R_c, contrary to what is measured in supercapacitor literature [2, 5, 7, 8].

If the adsorption process is limited by migration of ions from bulk electrolyte into the electrode (bottom section of figure 5.1), only the electrode thickness has an effect on the measured penetration depth l_c, and should be independent on the physical properties of the carbon.

Furthermore, the obtained value for electrode porosity ϕ_c should be realistic. This can be investigated by comparing ϕ_c to the estimated porosity of the electrode ϕ, which can be obtained by investigating the relative volume occupied by the activated carbon in the electrode. Since activated carbon has a density ρ_V of about 0.5 $g\ cm^{-3}$ [12], the porosity of the electrode ϕ can be estimated using equation (5.3).

$$\phi = 1 - \frac{\rho_{c,V}}{\rho_V} \tag{5.3}$$

In this equation, $\rho_{c,V}$ is the volumetric density of the electrode, which is the weight of carbon per volume electrode in $g\ cm^{-3}$.

5.4 Materials and methods

5.4.1 Investigated carbon materials

Two different types of carbons were tested, carbon fibers and carbon powders. Carbon fibers were used in the form of felts and cloths, and carbon powders were used in a polyvinylidene fluoride (PVDF) matrix. Table 5.1 shows the carbon materials investigated, together with the composition, supplier, electrode thickness d_c in μm and carbon weight per unit cell area $\rho_{c,A}$ in $g\ cm^{-3}$.

This table shows carbon fiber electrode composition as felt or cloth. The carbons 1 and 2 are made from the same activated carbon fiber, this also accounts for carbons 3 through 5. Carbon number 4 is equal to carbon number 3, except that the carbon felt FT 300-15 was ground in a ball mill grinder (PM 100, Retsch, Haan, Germany) together with N-Methylpyrrolidone (NMP, analytical grade, Boom, Meppel, The Netherlands) solvent for 2 h at 450 RPM to obtain a carbon paste. This was done to assess whether performance decrease occurs in the production of carbon powder electrodes with a PVDF matrix. In section 5.5, carbon 4 is classified as a carbon fiber.

Table 5.1 shows carbon powder electrode composition in weight percentage carbon, binder and graphite (carbon wt% - binder wt% - graphite wt%). Only in some cases graphite was added to the mixture, according to literature inclusion of graphite increases performance [13–15]. This was not observed in this study, and therefore it was omitted in most carbon mixtures. Carbon 12 is equal to carbon 13 except for the fineness of the carbon powder. Since all carbon powders were ground during electrode production, it is unlikely that this difference still exists in the PVDF matrix.

Electrode thickness d_c in μm was obtained using a thickness gauge (547-401 Mitutoyo, Veenendaal, The Netherlands). It must be noted that thickness could not be accurately determined in all cases due to compressibility, as indicated in the table.

Carbon number 17 was used in assessing the effect of electrode thickness on performance, 6 samples were made for 5 different thicknesses (1 duplo) ranging from 120 μm to 750 μm. Furthermore, carbon number 12 and 13 were also included in this analysis, to test the assumption that these carbons are equal and that inclusion of graphite has no effect on performance, since carbon 13 contains 10 % graphite. The average density of $0.45 \pm 0.02\ g\ cm^{-3}$ is used in the calculation of the performance parameters.

Table 5.1: Composition of all investigated electrodes, showing the carbon type, configuration of the electrode, supplier of the material, thickness d_c of the finished electrode, and the carbon weight per unit cell area $\rho_{c,A}$. Configuration indicates for carbon fiber electrodes the fiber configuration (felt or cloth), and for carbon powder electrodes the weight percentage carbon (% C), weight percentage binder (% B) and weight percentage graphite (% G) in the electrode.

Nr.	Carbon	Configuration % C - % B - % G	Supplier	d_c μm	$\rho_{c,A}$ $mg\ cm^{-2}$
1.	FT 300-20	Felt	[d]	1000[a]	34.8
2.	CH 900-20	Cloth	[d]	540	29.5
3.	FT 300-15	Felt	[d]	1000[a]	33.5
4.	FT 300-15	85.7 - 14.3 - 0	[d]	270	18.7
5.	CH 700-15	Cloth	[d]	460	23.4
6.	Evergrow	Felt	[e]	600[a]	14.2
7.	FM 10	Cloth	[f]	425	22.1
8.	FM 10 Meso	Cloth	[f]	548	22.4
9.	DLC Supra 50	84.8 - 15.2 - 0	[g]	260	16.0
10.	A Supra Eur	85.4 - 14.5 - 0	[g]	320	21.6
11.	YP 17D	85.8 - 14.2 - 0	[d]	280	18.5
12.	DLC Super 50 [b]	85.4 - 14.6 - 0	[g]	339	25.7
13.	DLC Super 30 [b]	81.6 - 8.2 - 10.2	[g]	328	24.0
14.	SAE Super	85.8 - 14.2 - 0	[g]	260	14.8
15.	SX Ultra	85.1 - 8.7 - 6.2	[g]	301	23.0
16.	Darco	85.9 - 14.1 - 0	[g]	240	15.8
17.	DLC Super 50 [b]	81.3 - 8.1 - 10.6	[g]	-	- [c]

[a] Approximate
[b] Used for thickness effect analysis
[c] Average volumetric density $\rho_{c,V} = 0.45\ g\ cm^{-3}$
[d] Kuraray Chemical Co. Ltd., Osaka, Japan
[e] Beijing Evergrow Resources Co., Beijing, China
[f] Chemviron, Charcoal Cloth International, Newcastle, UK
[g] Norit, Amersfoort, The Netherlands

5.4.2 Electrode production technique

To produce electrodes, a binder and carbon is needed. A polymer (Kynarflex 2800-00, Atofina, Philadelphia, USA) containing mainly PVDF[a] was used as a binder, since PVDF is inert and chemically stable. Increased binder content reduces performance

[a] The polymer also contains additives such as polyvinylpyrrolidone (PVP) to make the final electrodes more hydrophilic, the exact composition is undisclosed by the company

of the electrode [13, 15], therefore the PVDF content in the final produced electrode was minimized.

Preparation electrode solution

A 18 w% PVDF solution was made by mixing PVDF beads with NMP. The solution was stirred for 24 hours to ensure that PVDF fully dissolves. After the PVDF was dissolved, the PVDF solution was stored at 50 $°C$ to maintain low viscosity and to remove any entrained air.

The carbon was dried for 24 hours at 105 $°C$ to remove any adsorbed water. After drying, the carbon was mixed with NMP to make a 25 w% carbon ink. This ink was vacuum exsiccated for 4 hours to wet all carbon pores with NMP.

To make the final electrode solution, a 6:1 ratio ink to PVDF solution was put into a ball mill grinder (PM 100, Retsch, Haan, Germany), and the solution was mixed for 30 minutes at 450 RPM to ensure homogeneity of the electrode solution. After mixing, the electrode solution was left at 50 $°C$ for 24 h to deaerate.

Electrode casting

Electrodes were produced by the phase-inversion membrane casting method [16], whereby the electrode solution was cast onto a glass plate using a casting knife. This cast was immersed in demineralized water for at least 12 h to extract the solvent, which resulted in solidification of the PVDF binder and consequently the finished electrode. After casting the composite carbon electrode was cut to size and soaked in 0.1 M NaCl solution for at least 12 h, after which it could be used in the CDI setup. Soaking in NaCl solution ensures ions are present in the carbon pores, and ensures that a steady-state response can be quickly achieved.

5.4.3 Electrochemical characterization

The characterization setup as described in chapter 2 was used, except for some minor deviations. In this work a smaller electrode size of 16 cm^2 was used, allowing for more reproducible results. Furthermore, a non-activated felt (FMI Composites Ltd., Galashields, Scotland, further referred to as NA felt) was introduced between the electrode material and the current collectors. The inclusion of the NA felt was needed to prevent damaging fragile carbon electrodes.

By following the characterization procedure as described in chapter 2 electrode characteristics were obtained. These electrode characteristics were the total capacity C_c, in $F\,cm^{-2}$ at three cell voltages (E_{cell} = 0; 0.6 and 1.2 V), and resistance values

R_c and R_{ct}, in $\Omega\, cm^{-2}$, where R_c is the carbon electrode resistance and R_{ct} is the charge-transfer resistance between carbon electrode and current collector.

The specific double-layer area S of each carbon was obtained by relating the capacity results at the three cell voltages to the double-layer model as developed in chapter 3. Charge-transfer performance β was obtained by relating R_{ct} to the concentration and temperature of the electrolyte, as described in chapter 4. The penetration depth l_c was obtained by relating R_c to the conductivity of the electrolyte, as described in chapter 4.

5.4.4 Physical characterization

Nitrogen adsorption isotherms were measured using a Tristar 3000 system (Micromeritics, Norcross, USA) at 77 K. These isotherms were interpreted using BET analysis [17] to obtain total surface area BET, in $m^2\, g^{-1}$, using Harkins and Jura analysis [18] to obtain total micropore area A_{micro}, in $m^2\, g^{-1}$, and total macropore area A_{macro}, in $m^2\, g^{-1}$, and using Dubinin-Astakhov analysis [19] to obtain the median pore diameter of the micropores, d_p, in nm.

5.5 Results and discussion

5.5.1 Experimental observations during electrode preparation

Several experimental observations have to be taken into account to ensure success in the production of electrodes. When using carbons with a very high pore volume, or a very low pore volume, the amount of NMP in the ink has to be adjusted to ensure full wetting of the carbon pores. The resulting electrode solution should have approximately 25 w% solids for a good casting behavior. After casting the electrodes, immersion has to be done with the least amount of shear, high shear will break the electrodes.

5.5.2 SEM pictures

Figures 5.2 and 5.3 show SEM (scanning electron microscopy) pictures of a typical cast electrode. These figures show that using the developed electrode production technique, a very porous electrode can be made, consisting of carbon particles within a PVDF matrix. In figure 5.2 the PVDF fibrils that contain the carbon powder particles are clearly visible.

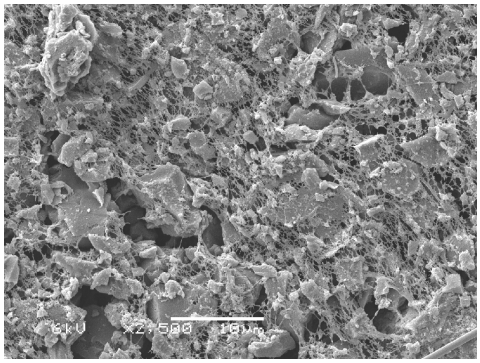

Figure 5.2: Top view of typical cast electrode, 2500x magnified

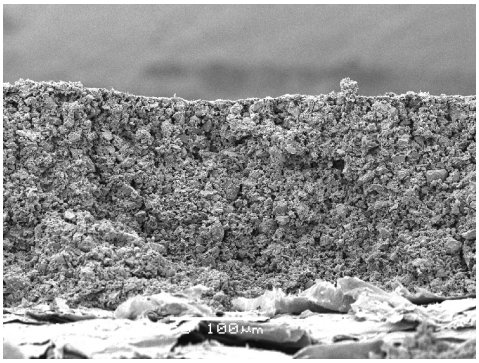

Figure 5.3: Cross section of typical cast electrode, 250x magnified

5.5.3 Effect inclusion NA felt

In most experiments, the cell is constructed as discussed in chapter 2. However, when performing experiments on fragile electrodes a non-activated carbon felt (NA felt) was included between current collector and carbon electrode to prevent damage to these electrodes. The inclusion of NA felt was found not to influence performance, except for the value of R_s. Table 5.2 shows results of some experiments with and without included NA felt. As shown in this table, inclusion of NA felt reduces R_s. The reason for this reduction is enhanced contact between current collector and carbon electrode; without NA felt some Ohmic resistance exists between current collector and carbon electrode, which is measured as part of R_s.

Table 5.2: Dependency of system resistance R_s on the inclusion of non-activated felt (NA felt) in the CDI cell

Material	Included NA felt	R_s ($\Omega\ cm^2$)	Source
FT 300-15	no	10.35 ± 0.1	Temperature dependency chapter 4
FT 300-15	no	12.4 ± 1.3	Concentration dependency chapter 4
CH 700-15	no	11 ± 2	Additional experiment
FT 300-15	yes	5.9 ± 0.1	Chapter 2
CH 700-15	yes	4.1 ± 0.1	This chapter

5.5.4 Electrode thickness

Figure 5.4 shows the linear increase of electrode capacity C_c with the weight of carbon per unit cell area $\rho_{c,A}$, represented by a linear regression through the origin. From the slope of the linear regression a specific capacity of $22.2 \pm 0.3\ Fg^{-1}$ is obtained.

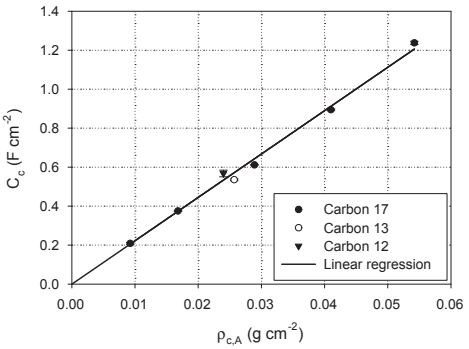

Figure 5.4: Measured capacity versus carbon weight per unit cell area with linear regression for electrodes made from DLC Super carbons

Figure 5.5 shows the linear increase of electrochemical thickness l_c with carbon weight per unit cell area, represented by a linear regression through the origin. From the slope of the linear regression a specific penetration depth λ_c of 2.6 ± 0.05 $cm\ g^{-1}\ cm^2$ is obtained. A small effect of electrode composition on l_c is seen, carbon electrode number 12 contains more binder and no graphite, and shows a slightly higher value for l_c.

Figure 5.6 shows the linear increase of electrochemical thickness l_c with electrode thickness d_c, represented by a linear regression through the origin. From the slope of the linear regression a porosity ϕ_c of 0.90 ± 0.04 is obtained. This is unrealistically high when only considering the porosity of the electrode, the estimated porosity ϕ using equation (5.3) is only about 30 %. Only when taking into account the very high porosity of the carbon powders the high value for ϕ_c be explained.

All other measured characterization parameters were found not to be related with electrode thickness. This includes the measurement for R_{ct}; an average value of $2.84 \pm 0.05\ \Omega\ cm^{-2}$ was found. This corresponds according to equation (4.10) to a β of 35.4 ± 0.6, and confirms that charge-transfer performance describes the charge-transfer on the interface between carbon electrode and current collector.

For R_s, an average value of $4.6 \pm 0.2\ \Omega\ cm^{-2}$ was found, which corresponds according to equation (4.1) with an effective spacer thickness l_s of $250 \pm 20\ \mu m$, which is low as compared to the actual spacer thickness. Possibly contact resistance R_0 is lower than measured in chapter 4, setting $R_0 = 0.07$ results in a electrochemical spacer thickness equal to the actual spacer thickness ($l_s = 380\ \mu m$).

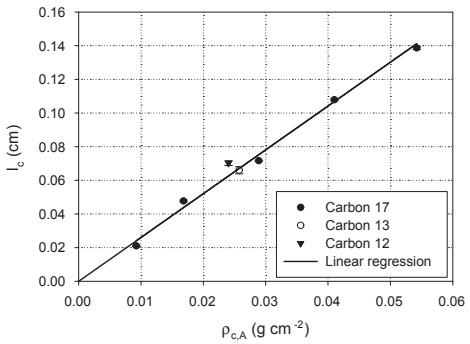

Figure 5.5: Electrochemical thickness versus the carbon weight per unit cell area with linear regression

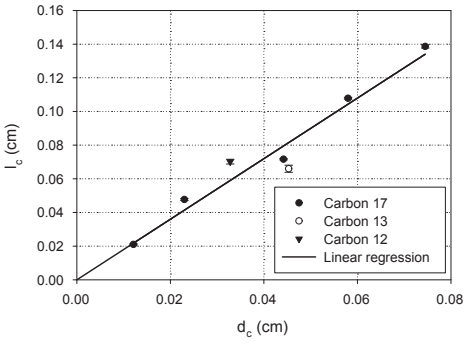

Figure 5.6: Electrochemical thickness versus electrode thickness with linear regression

5.5.5 Electrochemical surface area

Figure 5.7 shows the specific double-layer area S in $m^2\,g^{-1}$ versus BET in $m^2\,g^{-1}$. For both carbon types a clear link between BET and S can be seen; an increase in BET will increase S. Two exceptions exist in this relation, these are carbons 11 and 16, which show a higher specific double-layer area than expected from the BET surface area. There is a clear distinction between fiber electrode materials and powder electrode materials, fiber electrode materials have a significantly higher specific double-layer area at equal BET.

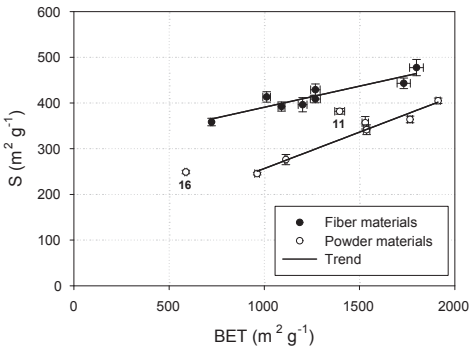

Figure 5.7: Specific double-layer area versus BET area, numbers relate to subsequent carbons. Linear trends are included to visualize the clear distinction between the two carbon types

Figure 5.8 shows the specific double-layer area S in $m^2\,g^{-1}$ versus micropore area A_{micro} in $m^2\,g^{-1}$. A clear trend is observed where S increases as A_{micro} increases. This trend accounts for both fiber as well as powder materials.

The carbons 11 and 16 that were exceptions in figure 5.7 to follow the general trend in figure 5.8. However, some new exceptions can be seen in figure 5.8, carbons 8, 9 and 15. This is due to the definition of A_{micro}, which is the amount of BET generated by carbon pores smaller than 1.6 nm. This is an arbitrary definition, when changing the definition of A_{micro} to the amount of BET generated by carbon pores smaller than 1.8 nm, A_{micro} for carbon number 9 increases significantly, as is depicted in figure 5.8 by the arrow. This means that for carbon number 9 a significant amount of pore area exists in the range of 1.6 through 1.8 nm. This observation is confirmed when investigating the relation between S and median pore diameter d_p as shown in figure 5.9; a higher median micropore size results in a higher value for S.

No relation between macropore area A_{macro} and S could be found.

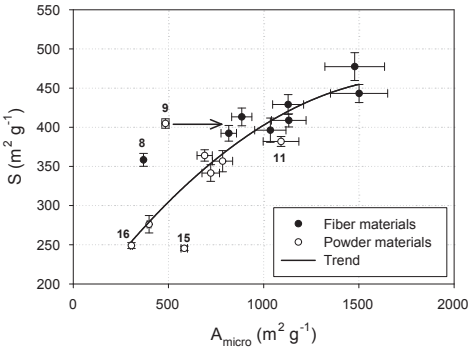

Figure 5.8: Electrochemical surface area versus micropore area, numbers relate to subsequent carbons. Trend is included to visualize approximate relation between S and A_{micro}

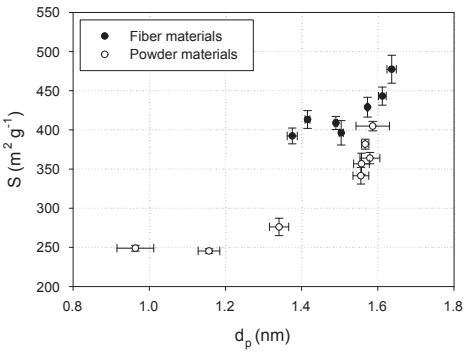

Figure 5.9: Electrochemical surface area versus median pore diameter

5.5.6 Charge-transfer performance

Figure 5.10 shows the relation between charge-transfer performance β and BET. In this figure, two proportional relations are seen between BET and charge-transfer performance β, where β increases as BET is increased. This agrees with the assumption that R_{ct} is a charge-transfer resistance, if more surface is available for electrons to move through, the resistance will be lower. The reason two distinct proportional relations exist might be because of differences in surface groups [11], however this remains speculation.

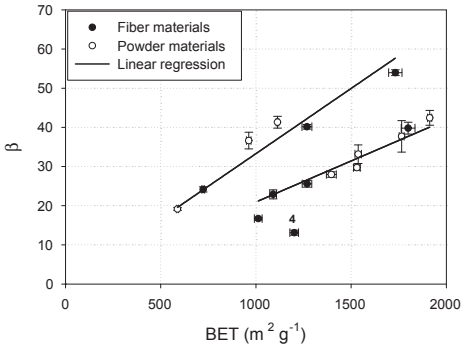

Figure 5.10: Charge-transfer performance versus BET, numbers relate to subsequent carbons

5.5.7 Electrode resistance

Figure 5.11 shows the relation between penetration depth l_c and electrode thickness d_c for all investigated electrodes. As can be seen from this figure, no clear relationship exists between l_c and d_c. It can be concluded from this graph that the thickness of an electrode d_c is not a good parameter to relate to the carbon electrode resistance R_c.

Figure 5.12 shows the relation between penetration depth l_c and the weight of carbon per unit cell area $\rho_{c,A}$ for all investigated electrodes. As can be seen from this figure, a reasonable proportional relationship exists between l_c and $\rho_{c,A}$, which using equation (5.1) results in an average specific penetration depth λ_c of 2.47 ± 0.09 $cm\ g^{-1}\ cm^2$ which is equal to the value found in section 5.5.4. It can be concluded from this graph that the weight of carbon per unit cell area $\rho_{c,A}$ is a good parameter to relate to the carbon electrode resistance R_c.

No clear relation was found between l_c and surface area characteristics such as micro- and macropore area.

5.5.8 Carbon matrix

To investigate the effect of the carbon matrix on performance, three carbons are compared that are constructed from the same carbon material, but where the electrode is constructed in different ways. Carbon 3 consists of a fiber in felt configuration (FT 300-15), carbon 4 consists of a ground fiber (FT 300-15) in a PVDF matrix, and carbon 5 consists of a fiber in cloth configuration (CH 700-15, equal fiber as FT 300-15). Characterization results for electrodes made from these materials are shown in table 5.3.

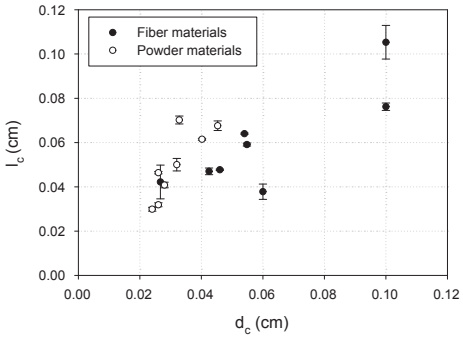

Figure 5.11: Penetration depth versus electrode thickness

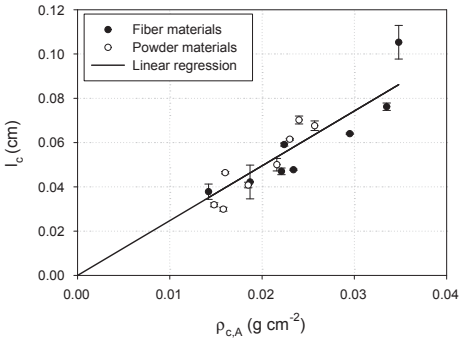

Figure 5.12: Penetration depth versus carbon weight per unit cell area

Table 5.3: Comparison of electrochemical and physical performance parameters for electrodes made of three configurations of the same carbon fiber; a felt configuration (carbon 3), a configuration where the fibers are ground and cast in a PVDF matrix (PVDF configuration, carbon 4), and a cloth configuration (carbon 5)

	Felt	PVDF	Cloth
Carbon number	3	4	5
BET	1270 ± 30	1200 ± 20	1260 ± 30
A_{micro}	1130 ± 80	1040 ± 80	1130 ± 90
d_p	1.57 ± 0.01	1.49 ± 0.01	1.49 ± 0.01
S	430 ± 13	400 ± 15	409 ± 8
β	25.6 ± 0.8	13.1 ± 0.7	40.3 ± 0.4
λ_c	2.27 ± 0.05	2.3 ± 0.4	2.04 ± 0.01
n_c	1.46 ± 0.01	0.62 ± 0.05	1.27 ± 0.01

Table 5.3 shows that the characterization for all three electrodes are very similar, the cloth configuration is equal to the felt configuration in terms of BET, micro pore area A_{micro} and specific double-layer area S. An insignificant part of the micropores is lost when using the PVDF configuration. This also results in a slightly lower value for S, but still within the error bounds of the felt and cloth configuration result. The specific penetration depth λ_c of all three electrodes is very similar, which is further proof that the adsorption process is limited by migration of ions into the separate carbon particles, since density and thickness differ for each electrode.

However, the transmission line behavior is different for the three carbon configurations; for the felt and cloth configuration a n_c higher than one is found, while for the PVDF configuration a n_c lower than one is found. This would mean that for the

felt and cloth configuration capacitance is concentrated in the beginning of the transmission line, meaning that capacitance can be accessed fast. Instead for the PVDF configuration the resistance is concentrated in the beginning of the transmission line, meaning that capacitance can only be slowly accessed.

Another difference between the three electrodes is for charge-transfer performance β, where the PVDF configuration shows about half the value for β as compared to the felt configuration, while the cloth configuration shows the highest value for charge-transfer performance. Even when compared to other carbons, as shown in figure 5.10, the PVDF configuration show a very low charge-transfer performance. In figures 5.13 and 5.14 SEM pictures are shown of the electrode with PVDF configuration.

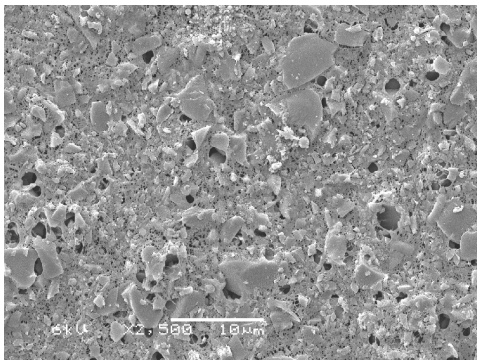

Figure 5.13: Top view of electrode with PVDF configuration, where carbon fibers were ground and cast in a PVDF matrix, 2500x magnified

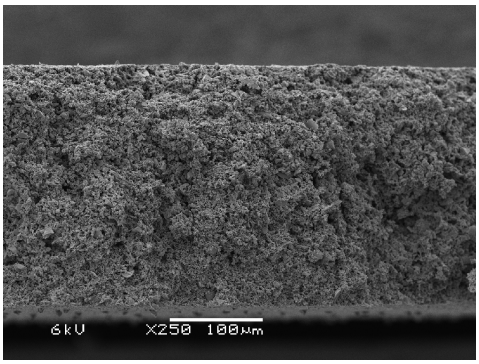

Figure 5.14: Side view of electrode with PVDF configuration, where carbon fibers were ground and cast in a PVDF matrix, 250x magnified

When comparing these SEM pictures to the SEM pictures of a normal cast electrode as shown in figures 5.2 and 5.3, it seems that a relatively high amount of binder is present in the electrode with PVDF configuration. Most likely the carbon fibers contain a certain amount of binder, during the grinding of the felt some of this binder is dissolved and re-solidifies in the electrode production process. Another difference between the two electrodes is the average carbon particle size, which seems smaller for the ground carbon fiber electrode. This can also be attributed to the long grinding time needed to transform the felt into a carbon paste.

The lower average particle size, and the relative high amount of binder are most likely responsible for the low value of β, the charge transfer process is blocked by the PVDF and the small contact area between current collector and carbon. The blocking of the pores would also explain the low value for n_c. The high value for β for the carbon cloth matrix can be explained by the difference in structure between felt and cloth. A cloth is much more ordered than a felt, therefore a higher contact

area exists between current collector and the separate carbon fibers.

5.6 Conclusion

The following relations between electrode performance parameters and electrode characteristics were obtained.

The inclusion of a non-activated carbon felt between electrode and current collector was found to affect measurement of system resistance R_s. This inclusion of non-activated carbon felt is needed to ensure proper contact between current collector and electrode.

The ion penetration depth l_c is directly related to the carbon weight per unit cell area $\rho_{c,A}$, and can be rewritten to a constant specific penetration depth λ_c of $2.47 \pm 0.09\ cm\ g^{-1}\ cm^2$ for all investigated carbons. This means that the resistance encountered during the adsorption of ions is determined by migration of ions into the separate carbon particles, and not by the migration of ions toward the separate carbon particles. Some reservations on this relationship exist, since binder and graphite content of the electrode do seem to have some influence on the ion penetration depth. Most likely this is caused by the electrical resistance between the separate carbon particles, as also seen in chapter 4, where at high conductivity the electrode resistance R_c became constant.

The specific double-layer area S is governed by micropore area that can be measured by nitrogen adsorption experiments according to Harkins and Jura analysis. By analyzing the median pore size, these micropores are found to be relatively big, up to 1.6 nm. This agrees with supercapacitor literature, where micropores and small mesopores were considered responsible for double-layer formation [2, 5, 7, 8], and with findings that micropores are important for ion electrosorption [9].

The pore structure of carbon is not related to resistance of the electrode, which contradicts supercapacitor research [2, 5, 7, 8]. This is attributed to the relatively low conductivity of the electrolyte used for CDI purposes. Because of the low conductivity, migration of the ions in the pores is relatively slow, and therefore a pore structure consisting mainly of small pores will not significantly hinder ion migration.

Charge-transfer performance β is not related to the thickness of the electrode, and therefore β is an interface process. β can be directly related to the BET area of a certain carbon, in two distinct proportional ways. This is affected by the nature of the contact between carbon and current collector, carbon fibers in a cloth configuration show a higher charge-transfer performance than carbon fibers in a felt configuration. More research is needed into the nature of β to clarify this difference,

Fiber materials have a higher performance in terms of specific double-layer area

than powder materials. This is due to microporous nature of these carbons. Grinding a fiber material and using the membrane casting method to produce an electrode using PVDF as a matrix has no negative effects on the performance of the subsequent carbon in terms of specific double-layer area S or specific penetration depth λ_c. Care must be taken not to include too much PVDF, since this reduces charge-transfer performance β since then the contact between current collector and carbon is altered.

Overall, it can be concluded that if the micropore area of a certain carbon is known, the specific double-layer area S can be predicted and therefore the deionization capacity. From loading rate of the carbon, part of the total resistance of the cell can be predicted, and therefore an indication for the deionization rate can be obtained. The charge-transfer performance has to be investigated more closely since two possible trends between charge-transfer performance and BET surface area exist, which does not allow a clear classification.

Bibliography

[1] M. J. Bleda-Martinez, J. A. Macia-Agullo, and D. Lozano-Castello. Role of surface chemistry on electric double layer capacitance of carbon materials. *Carbon*, 43(13):2677–2684, 2005.

[2] J. Gamby, P. L. Taberna, P. Simon, J. F. Fauvarque, and M. Chesneau. Studies and characterisations of various activated carbons used for carbon/carbon supercapacitors. *Journal of Power Sources*, 101(1):109–116, 2001.

[3] R. Saliger, U. Fischer, and C. Herta. High surface area carbon aerogels for supercapacitors. *Journal of Non-Crystalline Solids*, 225(1):81–85, 1998.

[4] H. Shi. Activated carbons and double layer capacitance. *Electrochimica Acta*, 41(10):1633–1639, 1996.

[5] M. Toupin, D. Belanger, and I. R. Hill. Performance of experimental carbon blacks in aqueous supercapacitors. *Journal of Power Sources*, 140(1):203–210, 2005.

[6] J. Wang, X. Yang, and D. Wu. The porous structures of activated carbon aerogels and their effects on electrochemical performance. *Journal of Power Sources*, 185(1):589, 2008.

[7] F. C. Wu, R. L. Tseng, C. C. Hu, and C. C. Wang. Physical and electrochemical characterization of activated carbons prepared from firwoods for supercapacitors. *Journal of Power Sources*, 138(1-2):351–359, 2004.

[8] G. Gryglewicz, J. Machnikowski, and E. Lorenc-Grabowska. Effect of pore size distribution of coal-based activated carbons on double layer capacitance. *Electrochimica Acta*, 50(5):1197–1206, 2005.

[9] H. Oda and Y. Nakagawa. Removal of ionic substances from dilute solution using activated carbon electrodes. *Carbon*, 41(5):1037–1047, 2003.

[10] C. Portet, P. L. Taberna, P. Simon, and C. Laberty-Robert. Modification of Al current collector surface by sol-gel deposit for carbon-carbon supercapacitor applications. *Electrochimica Acta*, 49(6):905–912, 2004.

[11] Y. R. Nian and H. S. Teng. Influence of surface oxides on the impedance behavior of carbon based electrochemical capacitors. *Journal of Electroanalytical Chemistry*, 540:119–127, 2003.

[12] K. Kinoshita. *Carbon, Electrochemical and physicochemical properties.* Wiley Interscience, New York, 1st edition, 1987.

[13] L. Bonnefoi, P. Simon, J. F. Fauvarque, C. Sarrazin, J. F. Sarrau, and A. Dugast. Electrode compositions for carbon power supercapacitors. *Journal of Power Sources*, 80(1-2):149–155, 1999.

[14] M. S. Michael and S. R. S. Prabaharan. High voltage electrochemical double layer capacitors using conductive carbons as additives. *Journal of Power Sources*, 136(2):250–256, 2004.

[15] K. K. Park, J. B. Lee, P. Y. Park, S. W. Yoon, J. S. Moon, H. M. Eum, and C. W. Lee. Development of a carbon sheet electrode for electrosorption desalination. *Desalination*, 206(1-3):86, 2007.

[16] M. Mulder. *Basic Principles of Membrane Technology.* Springer, 1996.

[17] S. Brunauer, P. H. Emmett, and Edward Teller. Adsorption of gases in multimolecular layers. *Journal of the American Chemical Society*, 60(2):309–319, 1938.

[18] W. D. Harkins and G. Jura. Surfaces of solids. XIII. A vapor adsorption method for the determination of the area of a solid without the assumption of a molecular area, and the areas occupied by nitrogen and other molecules on the surface of a solid. *Journal of the American Chemical Society*, 66(8):1366–1373, 1944.

[19] M. M. Dubinin. Fundamentals of the theory of adsorption in micropores of carbon adsorbents: Characteristics of their adsorption properties and microporous structures. *Carbon*, 27(3):457, 1989.

Chapter 6

Relations between electrochemical performance and deionization performance

6.1 Summary

To relate electrochemical performance to deionization performance, deionization experiments were performed for two different capacitive deionization cell configurations at different cell voltages. Electrochemical performance could be interpreted as a simple resistor - capacitor system, and could be linked to deionization performance by using two distinct efficiency parameters. To prevent electrical short-circuit and redox reactions in a capacitive deionization cell, ion-exchange membranes can be used, which furthermore increases deionization rate by 25 % as compared to a cell without ion-exchange membranes. This system, called MCDI for membrane capacitive deionization, yields a factor 10 higher deionization rate, a 36 % higher adsorption capacity and reduced redox reactions as compared to state-of-the-art carbon aerogel electrode systems.

6.2 Introduction

In the previous chapters, CDI material characteristics were linked to electrochemical performance in terms of capacity and resistance. In this chapter, the relation between electrochemical performance and deionization performance is investigated. This is done by performing deionization experiments with two different capacitive deionization cell configurations. The first configuration is a "classical" CDI configuration where two electrodes are separated by a spacer and immersed in electrolyte, as discussed in the previous chapters. The second is a configuration where ion-exchange membranes are employed. To make the distinction with "classical" CDI, CDI with ion-exchange membranes is referred to as MCDI, and if no distinction is made, the general process is referred to as (M)CDI.

A typical MCDI unit consists of a stack of MCDI cells. A diagram of the MCDI cell configuration as used in this research is shown in figure 6.1. The MCDI cell consists of two porous carbon electrodes separated by two ion-exchange membranes

van Limpt, B., Bruning, H., Metz, S.J., Rulkens, W.H.

and a spacer. The cell is connected to a power supply by current collectors. The spacer distributes the saline influent and separates the membranes.

The ion-exchange membranes present in the cell are membranes containing functional groups. When positive functional groups are present, the membrane is an anion-exchange membrane and only exchanges anions, and when negative functional groups are present, the membrane is an cation-exchange membrane and only exchanges cations [1, 2]. The cell consists of three separate compartments, a spacer compartment and two electrode compartments. Due to the ion-exchange membranes, only anions can be transported between the positive electrode compartment and the spacer compartment, and only cations can be transported between the negative electrode compartment and the spacer compartment.

The deionization process starts by applying a potential difference over the cell. This creates a driving force for ions to migrate from the saline solution through the ion-exchange membranes towards the porous electrode surface, as depicted in figure 6.1. The ions are electrochemically adsorbed on the surface of the porous electrodes in an electrical double-layer. This process results in a decrease of ions in the spacer compartment, and an increase of ions in the electrode compartments, therefore deionizing the saline influent.

Due to the accumulation of charge in the electrodes, the potential difference over the cell reduces to zero, and therefore adsorption of ions is halted. At this point, the cell is saturated and the process can be reversed by setting the potential difference between the two porous electrodes to zero. The driving force for migration is now the charge difference between the two electrodes, and therefore ions will migrate back from the electrode compartment to the spacer compartment.

The rate of the deionization process depends on the electrical resistance of the MCDI cell, and is determined by the distance between the two electrodes and the specific conductivity of the solution, as discussed in chapter 4. A high deionization

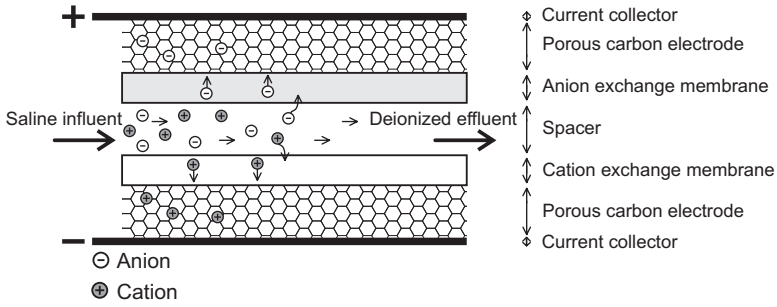

Figure 6.1: Diagram of the MCDI cell configuration depicting the deionization process

rate can be obtained by minimizing the electrical and ionic resistances of the cell. A large part of this resistance is situated in the solution of the spacer compartment, reducing the thickness results in a lower resistance and therefore a higher deionization rate.

The maximum adsorption capacity of the deionization process is dependent on the type of porous carbon electrode, as discussed in chapter 5. Usually these are high specific surface area carbons, such as powders (extruded or in a composite with polymers) [3–5], fibers [6–8], nanotubes [9], and aerogel [10–16]. In the configuration as described in this chapter, carbon powder composites are used, since carbon powder is inexpensive and has a high surface area (up to 3000 $m^2\ g^{-1}$ [17]).

The use of ion-exchange membranes for capacitive deionization is relatively new, however some research exists on application of ion-exchange membranes [18, 19]. The application of ion-exchange membranes in MCDI has the following advantages:

- Ion-exchange membranes physically isolate the electrode compartment, therefore no electrode erosion occurs. In normal CDI this takes place due to shear forces of the solution flow [20]. Erosion results in loss of performance in time, and eroded carbon particles can cause electrical short-circuits.

- Low spacer channel thicknesses can be obtained without chance of electrical short-circuit due to the physical isolation

- Electrochemically active groups present on the surface of carbon powders can give rise to surface redox reactions [21, 22] in normal CDI, and therefore part of the applied current is lost to these reactions. By using ion-exchange membranes reaction products of surface redox reactions remain in the electrode compartment, and the buildup of these reaction products might eventually reduce the surface redox reactions.

- During discharging ions are recombined only in the spacer compartment, creating a highly concentrated brine stream.

- During charging co-ions are obstructed in migrating from the electrode compartment to the spacer compartment [19]. This enhances the efficiency of the deionization process.

Drawbacks of ion-exchange membranes include increased resistance [23–25] and increased costs.

Besides testing the relationship between electrochemical performance and deionization performance, the performance of normal CDI cells and MCDI cells where ion-exchange membranes are included is studied. These membranes prevent erosion

of carbon particles and electrical short-circuit. The performance of the membrane system is compared with a composite electrode with a dense non-woven glass fiber insulating spacer. This dense spacer also prevents electrical short-circuit and erosion of the carbon electrode but is not practical in its use for CDI applications (too high hydrodynamic resistance, susceptible for fouling). However, it clearly demonstrates the performance of a CDI system with only carbon electrodes. On both cells deionization rate and maximum adsorption capacity (performance) will be obtained, and the relation between applied charge and removed ions (efficiency).

The results of the MCDI system will be compared to CDI systems described in literature.

6.3 Theory

6.3.1 Principle of (M)CDI operation

The driving force for ion transport in a (M)CDI cell is the potential gradient in the cell $-\Delta E$ in $V cm^{-1}$ [26]. With Ohm's law, this potential gradient can be related to a current density i in $A\ cm^{-2}$ according to equation (6.1)

$$i = -\Delta E \sigma \tag{6.1}$$

In this equation, σ is the electronic conductivity of the cell, in $S\ cm^{-1}$. Equation (6.1) can redefined to equation (6.2) when considering that the potential gradient is related to cell voltage E_{cell} in V.

$$i = \frac{E_{cell}}{R} \tag{6.2}$$

In this equation, R is the total cell resistance per unit area in $\Omega\ cm^2$, which depends on the resistance of the individual components of the cell.

The amount of ions stored in the porous carbon electrode per unit area cell $c_{s,A}$ in $mol\ cm^{-2}$ is linked to the amount of charge stored per unit area cell as is presented in equation (6.3).

$$c_{s,A} = \frac{C E_{cell}}{zF} \tag{6.3}$$

In this equation, C is the electrical capacity of the cell, in $F\ cm^{-2}$, and zF is the equivalent of charge needed to effectively adsorb one mole of salt.

With the expression of the deionization process as function of the electrical properties C and R, an equivalent electrical RC circuit for the whole process can be constructed, as shown in figure 6.2. This equivalent electrical circuit is similar to the

RC circuit presented in chapter 2 for interpretation of potentiometry data. In this figure, i_{leak} is a possible leak current per unit area (M)CDI cell, in $A\ cm^{-2}$, for example due to redox reactions [22]. Amperometry [27] was used as a method to obtain values for the electrical properties. Hereby the (M)CDI cell is charged at constant cell voltage E_{cell} in V, and discharged at 0 V cell voltage. By discharging at $E_{cell} = 0$, no leak current can occur.

Using the equivalent system as described in figure 6.2 the theoretical charge on the electrodes can be defined as function of time at given R and C. This is presented in equations (6.4) and (6.5).

$$Q_{charge}(t) = i_{leak}t + E_{cell}C\left(1 - e^{-t/\tau}\right) \quad (6.4)$$

$$Q_{discharge}(t) = E_{cell}Ce^{-t/\tau} \quad (6.5)$$

$$\tau = RC \quad (6.6)$$

In this equation, $Q_{charge}(t)$ is the charge on the electrodes during charging in $C\ cm^{-2}$ as function of time t in s, $Q_{discharge}$ is the charge on the electrodes during discharging in $C\ cm^{-2}$ as function of time t in s, and τ is the characteristic time of the cell, in s, defined according to equation (6.6). It takes $3\,\tau\ s$ to charge or discharge the cell for 95 %.

6.3.2 Discussion on the use of an equivalent electrical circuit

The equivalent electrical circuit as presented in this section is a simplification, as already discussed in chapter 2. In practice, R and C will vary during the deionization process, R and C are dependent on the salt concentration in the spacer compartment; C due to double-layer characteristics [26] (chapter 3) and R due to conductivity effects (chapter 4). Therefore, the value for the obtained R and C will be an average over the discharge process. To obtain an accurate value for R and C, a constant influent

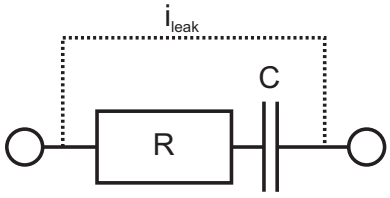

Figure 6.2: Equivalent electrical RC circuit for the (M)CDI process consisting of a resistor R corresponding with ion transport resistance, a capacitor C corresponding with double-layer capacitance, and a leak current i_{leak}

concentration is used, and each charge and discharge step is performed for an extended amount of time ($t >> 3\tau$). In chapter 8 the simplified RC approach will be compared to a more thorough modeling of the (M)CDI process.

6.3.3 Performance

To obtain the deionization rate J, defined as amount of salt removed per cell area over time ($mol\ cm^{-2}\ s^{-1}$), the fact is used that it takes $3\,\tau$ to adsorb or desorb 95 % of $c_{s,A}$, as follows from equation (6.5). Therefore it takes at least $6\,\tau\ s$ to complete a combined charge and discharge step. By using equation 6.3 the deionization rate J in $mol\ cm^{-2}\ s^{-1}$ can be obtained according to equations (6.7) and (6.8).

$$J = \frac{c_{s,A}}{6\tau} \tag{6.7}$$

$$J = \frac{E_{cell}}{6RzF} \tag{6.8}$$

The adsorption capacity is already defined in equation (6.3) in $mol\ cm^{-2}$. However, by obtaining the adsorption capacity in $mol\ g^{-1}$ carbon electrode, a more general performance parameter can be obtained, since a weight based performance parameter directly relates to the amount of carbon in the electrode. To obtain c_s in $mol\ g^{-1}$, $c_{s,A}$ is related to the carbon weight per unit cell area $\rho_{c,A}$ in $g\ cm^{-2}$, according to equation 6.9.

$$c_s = \frac{c_{s,A}}{\rho_{c,A}} \tag{6.9}$$

In obtaining $\rho_{c,A}$, only the weight of carbon powder in the composite electrodes is considered, not of other constituents of the composite, since only the carbon powder significantly contributes to ion adsorption.

6.3.4 Efficiency

Coulombic efficiency

To relate electrochemical performance to deionization performance two efficiencies are defined.

The first efficiency is the coulombic efficiency CE, the fraction of applied current that is actually stored on the electrode. It is a measure for the amount of leak processes occurring during the charging process, a low CE means a big part of the applied current is lost due to leak processes. CE is defined according to equation (6.10).

$$\text{CE} = \frac{Q_{discharge}}{Q_{charge}} \tag{6.10}$$

In this equation, Q_{charge} is the total amount of charge applied to the electrodes during charging in $C\ cm^{-2}$, and $Q_{discharge}$ is the total amount of charge released by the electrodes during discharging in $C\ cm^{-2}$.

One problem that arises in this method is that CE is dependent on the length of the experiment; the longer the electrode is charged, the higher the amount of leak charge included in Q_{charge}. Therefore CE reduces when increasing charging time.

To make CE independent of charging time, only the leak current that occurs between $t = 0$ and $t = 3\ \tau$ is considered, as is shown in equations (6.11) and (6.13), this is in line with the calculation of J.

$$\text{CE}_{3\tau} = \frac{Q_{discharge}}{Q_{charge} - i_{leak}\,(t_{step} - 3\tau)} \tag{6.11}$$

$$\tag{6.12}$$

In this equation, t_{step} is the time the charge step takes, and i_{leak} is the average leak current, defined according to equation (6.13).

$$i_{leak} = \frac{Q_{charge} - Q_{discharge}}{t_{step}} \tag{6.13}$$

By subtracting the leak current occurring after $t = 3\tau$ from Q_{charge}, CE becomes independent of charging time.

Deionization efficiency

The second efficiency is deionization efficiency Λ, the fraction of stored charge that is used to adsorb ions. Various processes can give rise to a $\Lambda < 1$. One process is pseudo-capacitance, where capacity is generated due to redox reactions on the surface of the electrode [22], which increases electrical capacity but not ionic capacity. A second possible process is expulsion of co-ions from electrode compartment to spacer compartment [28], which reduces the ionic capacity. A third possible process is that before an ion can be adsorbed onto a surface, first the natural surface charge has to be overcome. Activated carbons have a high natural surface charge due to the surface functional groups. This surface charge is dependent on the type of carbon and pH of solution [21]. Finally, the fourth possible process is that isolated cell sections (dead pockets) can reduce Λ, since these dead pockets will generate electrical capacity, but due to the isolation they will not participate in deionization.

Deionization efficiency Λ is defined according to equation (6.14)

$$\Lambda = \frac{Q_s}{Q_{discharge}} \tag{6.14}$$

In this equation, $Q_{discharge}$ is the electric charge released during discharge in $C\ cm^{-2}$, and Q_s in $C\ cm^{-2}$ is the equivalent ionic charge released during discharge. Q_s is obtained from the concentration difference between influent and effluent, according to equations (6.15) and (6.16).

$$Q_s = \frac{z\Phi F \int_0^{t_{step}} \Delta c\ dt}{A} \tag{6.15}$$

$$\Delta c = c(t) - c_0 \tag{6.16}$$

In these equations, $c(t)$ in $mol\ cm^{-3}$ is the measured effluent concentration as function of time t in s, c_0 in $mol\ cm^{-3}$ is the influent concentration, t_{step} is the step time in s, A is the total cell area in cm^2 and Φ is the flow rate in $cm^3\ s^{-1}$.

Correction performance for efficiency

To obtain a fair comparison between performance of our cell configuration and performance of cell configurations described in literature, c_s and J are corrected for Λ according to equations (6.17) and (6.18).

$$c_{s,eff} = c_s\ \Lambda \tag{6.17}$$

$$J_{eff} = J\ \Lambda \tag{6.18}$$

In this equation, $c_{s,eff}$ is the effective salt capacity in $mol\ g^{-1}$, and J_{eff} the effective deionization rate in $mol\ cm^{-2}\ s^{-1}$.

6.4 Materials and methods

6.4.1 Setup

Figure 6.3 shows a presentation of the experimental setup. The deionization process takes place in the (M)CDI unit. The (M)CDI unit was connected to a potentiostat (IviumStat, Eindhoven, The Netherlands) that was used as a power supply, and also records pH and conductivity values.

The solution in the influent tank was continuously deaerated by nitrogen bubbling. Before each experiment, the exact solution composition in the influent tank

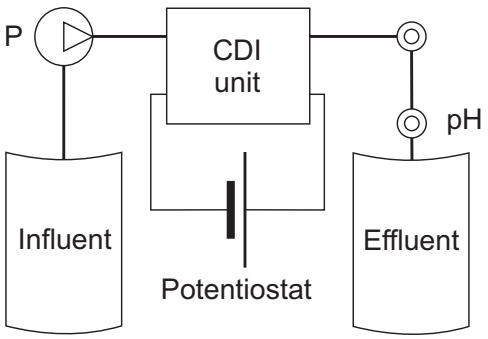

Figure 6.3: Presentation of the used experimental setup. P indicates the pump, σ indicates measurement of conductivity, and pH indicates measurement of pH

was recorded. Flow rate was controlled by a peristaltic pump P (Masterflex pump, Cole-Parmer, Vernon Hills, USA) at 1.5 $cm^3\ s^{-1}$. Conductivity of the effluent was measured by a conductivity electrode, denoted as σ in figure 6.3 (ProSense, Oosterhout, The Netherlands), and pH was measured by electrode pH (ProSense, Oosterhout, The Netherlands). The solution was discharged into an effluent tank.

In all cases the solution used for deionization was a 0.01 M NaCl (analytical grade, Boom, Meppel, The Netherlands) solution in demineralized water. Conductivity values were transformed to concentration (calculated using Stream Analyzer 2.0, OLI Systems Inc.). Conductivity was compensated for the pH of the effluent to correct for conductivity effects of H^+ and OH^- formation.

6.4.2 (M)CDI cells

Figure 6.1 shows a presentation of the MCDI cell. The CDI cell is similar to the MCDI cell, except for the use of membranes and the use of spacer. In case of the MCDI cell, a 92 μm open mesh spacer (Nitex 03-80/37, Sefar, Goor, The Netherlands) was used. In case of the CDI cell, the elements CEM and AEM were removed and a 350 μm non-woven glass fiber spacer (AP20, Millipore, Billerica, USA) was used since an open spacer will cause electrical short-circuit and erosion of carbon. The choice of spacer will have an effect on the total resistance of the cell that will be considered in the results.

6.4.3 Composite carbon electrodes

Composite carbon electrodes were constructed by mixing carbon with a PVDF (Kynarflex 2800-00, Atofina, Philadelphia, USA) solution in NMP (analytical grade,

Boom, Meppel, The Netherlands). The mixing was done in a ball mill grinder (PM 100, Retsch, Haan, Germany) at 450 RPM for 30 minutes to ensure homogeneity. After mixing, the resulting dispersion of carbon particles in PVDF solution is left at 50 $°C$ for 24 h to deaerate.

Casting of the dispersion was done by the phase-inversion membrane casting method [29], where a 500 μm thick layer of the dispersion was cast onto a glass plate. This cast was immersed in demineralized water to extract the solvent, which resulted in solidification of PVDF and consequently the finished electrode. After casting the composite carbon electrode was cut to size and soaked in 0.1 M NaCl solution for 12 h, after which it could be used in the (M)CDI setup.

The electrode consisted after casting of 80 w% DLC Super 50 (Norit, Amersfoort, The Netherlands), 10 w% graphite powder (Boom, Meppel, The Netherlands) and 10 w% PVDF. Thickness of one electrode was 270 ± 10 μm and the area 33.44 cm^2. Graphite powder was added since it is reported to increase performance [30]. Carbon surface density of the CDI cell was 22.2 ± 0.8 mg carbon cm^{-2} cell, and 21.6 ± 0.8 mg carbon cm^{-2} cell for the MCDI cell. In carbon surface density, only the amount of DLC Super 50 per square centimeter cell was considered, since the specific surface area of the graphite is negligible.

6.4.4 Ion-exchange membranes

The ion-exchange membranes used were Neosepta AMX and CMX membranes. Table 6.1 summarizes the characteristics of the membranes.

Table 6.1: Physical and electrical characteristics of the used Neosepta membranes

Characteristic	AMX	CMX	Source
Permselectivity (%)	91	99	[1]
Electric resistance ($\Omega\ cm^2$)	2.4	2.9	[1]
Thickness (mm)	0.14	0.18	Measured

Membrane characteristics from Długołęcki et. al. [1] were obtained at $0.5\,M$ NaCl, and are highly dependent on salt concentration of the solution [23–25].

6.4.5 (M)CDI operation

In all cases the (M)CDI unit was operated at amperometric conditions, where cell voltage was controlled and the resulting current was measured. One (M)CDI cycle comprises two steps. In the first step a positive E_{cell} was applied for 400 s, and the resulting current was measured as i_{charge} in $A\ cm^{-2}$. In the second step the (M)CDI

unit was discharged at $E_{cell} = 0\,V$ for 400 s and the resulting current was measured as $i_{discharge}$ in $A\ cm^{-2}$. Each cycle was repeated at least 4 times, data from the first cycle was omitted to ensure steady state results. Cell voltages E_{cell} of 0.3, 0.6, 0.9, 1.2, 1.4 and 1.6 V were investigated.

6.5 Results and discussion

6.5.1 Effect of membranes on performance and efficiency

General behavior

Figures 6.4 and 6.5 show the results of a typical deionization experiment for both the CDI cell as well as the MCDI cell. For both experiments during charging a cell voltage E_{cell} of $1.4\,V$ was applied for 400 seconds and during discharge a cell voltage E_{cell} of $0\,V$ was applied also for 400 seconds.

Figure 6.4 shows evolution of effluent concentration c, and figure 6.5 shows evolution of accumulated charge on the (M)CDI electrodes Q together with RC model response.

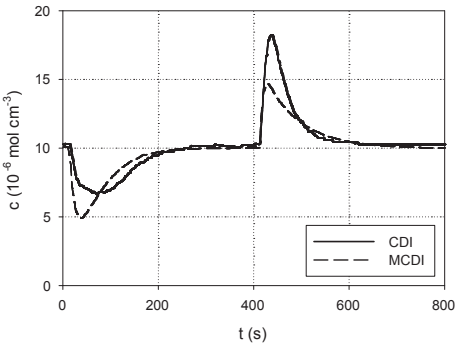

Figure 6.4: Effluent concentration versus time for the CDI cell and the MCDI cell. Cell voltage was 1.4 V, cell voltage during $400 < t < 800$ s was 0 V, influent concentration was $10\ 10^{-6}\ mol\ cm^{-3}$

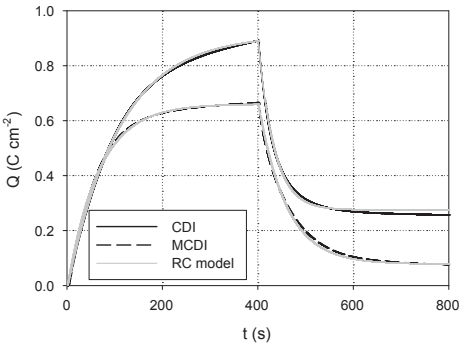

Figure 6.5: Accumulated charge versus time for the CDI cell and the MCDI cell together with proposed RC model response. Cell voltage during $0 < t < 400$ s was 1.4 V, cell voltage during $400 < t < 800$ s was 0 V

As shown in both figures, during charging ($0 < t < 400$ s) the accumulated charge Q for both cell configurations increased. Consequently ions were adsorbed, and effluent concentration c decreased. After a certain time ($t \approx 200$ s) the electrodes were fully charged and adsorption stopped; effluent concentration became equal to

influent concentration. In the MCDI cell a lower minimal effluent concentration was reached, and a faster deionization rate was obtained. This is most likely due to differences in spacer material, the non-woven glass fiber spacer in the membrane-less system caused a high pressure drop between the inlet and outlet of the CDI cell, this will promote preferential flow, resulting in an uneven charging of the electrode surface.

After the electrodes were fully charged and the effluent concentration reached the concentration of the influent, accumulated charge Q still increased, especially in the CDI cell. During charging the pH of the effluent decreased from pH 7 to pH 4.5 for the MCDI cell, and from pH 7 to pH 3.1 for the CDI cell. The lower pH in the in the CDI cell indicates that the observed continuous increase of Q can be attributed to redox reactions, since only redox reactions can give rise to the pH decrease.

During discharge ($400 < t < 800$ s) the accumulated charge Q on both cell configurations decreased. Consequently the adsorbed ions were desorbed, and effluent concentration c increased. The discharge for the MCDI cell was slower, most likely due to the membranes that introduce extra resistance. The reason that with the MCDI cell resistance is reduced during charging, while resistance is increased during discharging is subject of investigation.

After a certain amount of time ($t \approx 600$ s) the cell configurations were fully discharged, and the effluent concentration became equal to the influent concentration. Accumulated charge Q became stable, and effluent pH of both systems became constant at pH 7, indicating absence of redox reactions during discharge.

From both figures performance parameters capacity C and resistance R were obtained by applying the proposed RC model. Figure 6.5 shows the application of the proposed RC model (equations (6.4) and (6.5)) to the measured charge Q. As shown in the figure, the RC model corresponds well with data for both cell configurations. For capacity one unique value could be obtained for both the charge as well as the discharge process. However, for resistance not one unique value could be obtained, resistance during charging differed from resistance during discharge. Therefore, two values will be obtained for resistance, R_{charge} for the resistance during charging, and $R_{discharge}$ for the resistance during discharge.

From both figures coulombic efficiency CE was obtained using equation (6.10) and the final value for Q, deionization efficiency Λ was obtained by comparing the total amount of released charge between $400 < t < 800$ s with the total amount of released ions according to equation (6.14). As shown in the figure, CE for the CDI cell is lower than CE for the MCDI cell, since the final value for Q is higher for the CDI cell while the discharge curves themselves are similar.

Resistance and capacity

Figure 6.6 shows capacity C in $F\ cm^{-2}$ obtained using equation (6.5), versus E_{cell} in V. As is shown in this figure, capacity increases with E_{cell}, in accordance with double-layer kinetics. When taking into account that the CDI cell has a higher carbon surface density, results are similar for both cell configurations.

Figure 6.7 shows resistance during charging R_{charge} in $\Omega\ cm^2$ obtained using equation (6.4), versus E_{cell} in V. As is shown in this figure, for both cell configurations resistance during charging R_{charge} increases with E_{cell}. This can be explained since with increasing E_{cell} the average concentration in the spacer compartment during charging decreases. Therefore capacity C increases, resulting in an increase of solution resistance with E_{cell}. For the CDI cell, obtaining accurate values for R_{charge} became difficult at high values of E_{cell} due to correlation between R_{charge} and R_{leak}; at high leak current equation (6.4) no longer accurately represents the charge process. R_{charge} for MCDI is 40 $\pm$ 10 $\Omega\ cm^{-2}$ lower than R_{charge} for CDI, which translates in approximately 25 % faster charge kinetics for MCDI. In chapter 8 this phenomena is more closely investigated.

Figure 6.8 shows resistance during discharging $R_{discharge}$ in $\Omega\ cm^2$ obtained using equation (6.5), versus E_{cell}. As is shown in this figure, for both cell configurations resistance during discharging $R_{discharge}$ decreases with E_{cell}. This can be explained since with increasing E_{cell} the average concentration during discharging increases since capacity C increases, resulting in an decrease of solution resistance with E_{cell}. The average difference in $R_{discharge}$ between both cell configurations is $68 \pm 9\,\Omega\ cm^2$, meaning that the discharge process of the CDI cell is approximately 44 % faster than the discharging process of the MCDI cell. This difference is attributed to membrane resistance. The high value for this resistance is due to the low concentration of salts in the solution, causing a significant increase in membrane resistance [23–25]. Results from Długołęcki et al. indicate a value of $\Delta R = 64 \pm 1\,\Omega\ cm^2$ for combined AMX and CMX membranes at 10 mM NaCl, which confirms our result, despite the difference in spacer material and thickness.

Figure 6.9 shows overall resistance R in $\Omega\ cm^2$, which is the average of R_{charge} and $R_{discharge}$, versus E_{cell}. As shown in this figure, an approximate constant resistance of is obtained for both MCDI and CDI, where for the MCDI cell an average of $122 \pm 5\ \Omega\ cm^2$ is reached, and for the CDI cell an average of $137 \pm 5\ \Omega\ cm^2$ is reached, meaning that both resistances are approximately equal.

Efficiency

Figure 6.10 shows coulombic efficiency $CE_{3\tau}$, obtained using equation (6.13), versus E_{cell}. This figure shows that for the CDI cell $CE_{3\tau}$ decreases with increasing E_{cell},

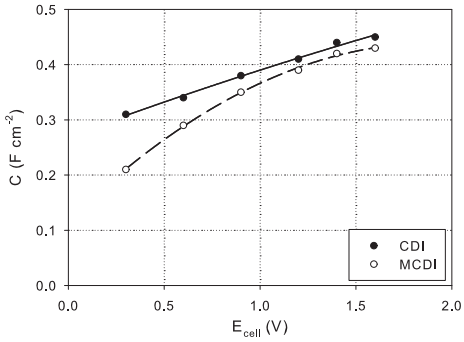

Figure 6.6: Capacity versus cell voltage for CDI cell and MCDI cell together with lines to guide the eye

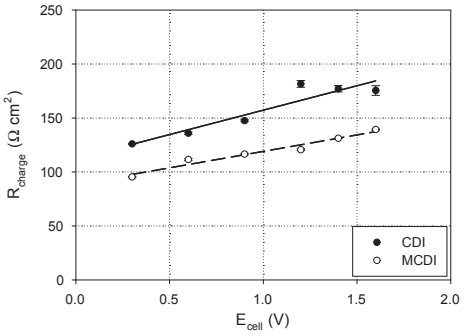

Figure 6.7: Charge resistance versus cell voltage for CDI cell and MCDI cell together with trend lines

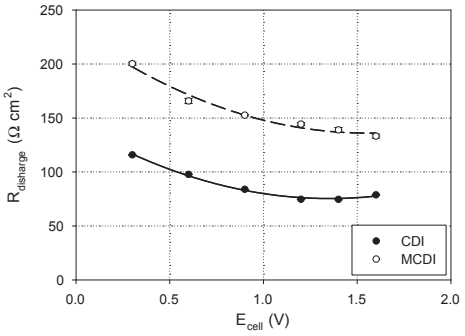

Figure 6.8: Discharge resistance versus cell voltage for CDI cell and MCDI cell together with trend lines

while for the MCDI cell $CE_{3\tau}$ increases with cell voltage to a maximum value of 0.96 at $E_{cell} = 0.9\,V$, after which $CE_{3\tau}$ decreases again. The decrease of $CE_{3\tau}$ for the CDI cell can be explained by the occurrence of redox reactions which are dependent on E_{cell}. By using ion-exchange membranes this occurs to a lesser extent, co-ion redox reaction products will accumulate in the electrode since they cannot penetrate the membrane. This will inhibit redox reactions. The lower value for $CE_{3\tau}$ at $E_{cell} < 0.9$ is probably related to charge losses over the membrane. More research on membrane characteristics in (M)CDI cells is needed to explain this phenomena.

Figure 6.11 shows deionization efficiency Λ, obtained using equation (6.14), versus E_{cell}. For the CDI cell Λ increases with cell voltage, while at cell voltages above 1.2

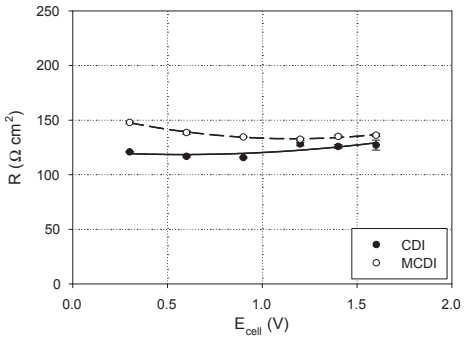

Figure 6.9: Overall resistance versus cell voltage for CDI cell and MCDI cell together with trend lines

V Λ seems to decrease again. For the MCDI cell Λ is relatively constant around 0.75.

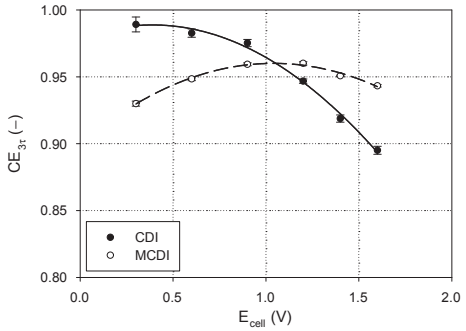

Figure 6.10: Coulombic efficiency versus cell voltage for CDI cell and MCDI cell together with trend lines

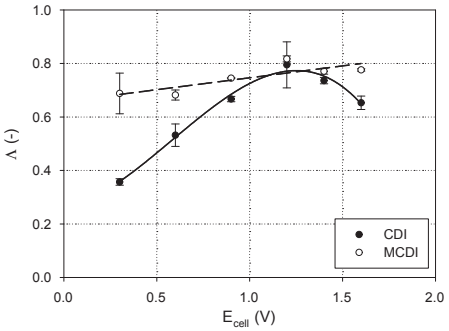

Figure 6.11: Deionization efficiency versus cell voltage for CDI cell and MCDI cell together with trend lines

In section 6.3.4 four different processes were proposed to explain the deviation of Λ from unity. The first process, pseudo-capacitance can be ruled out since then Λ should decrease with E_{cell} [22]. The second process, expulsion of co-ions from the electrode, can explain the difference between the MCDI cell and the CDI cell. When using membranes, expulsion of co-ions will be slowed down due to the ion selectivity of the membranes. Furthermore, the amount of co-ions in the electrode is limited, therefore the relative amount of co-ion expulsion will reduce with increasing cell potential, which agrees with results. However, this process does not explain an overall maximum value of $\Lambda = 0.75$ for both MCDI and CDI. This could be due to surface charge effects or

dead pocket effects, both processes increase proportionally with cell voltage. Surface charge effects on Λ can be evaluated by investigating dependence of Λ on the type of carbon in the electrode. Dead pocket effects on Λ can be evaluated by investigating dependence of Λ on cell geometry.

Performance

Figure 6.12 shows the effective deionization rate J_{eff} in 10^{-9} $mol\ cm^{-2}\ s^{-1}$, obtained using equation (6.18), versus E_{cell}. As shown in this figure, J_{eff} is equal for both CDI and MCDI, since the overall resistance R is similar for both CDI and MCDI. However at $E_{cell} = 1.6\ V$ the MCDI cell gives a significantly higher deionization rate. In general, J_{eff} shows a linear relation with E_{cell}. It is interesting to note that this linear relation does not intercept the origin, instead the intercept is at $E_{cell} \approx 0.11\ V$, which would indicate that there exists a certain minimum cell voltage before deionization takes place. More research into the low cell voltage range is needed to confirm this finding.

Figure 6.13 shows effective deionization capacity $c_{s,eff}$ in 10^{-3} $mol\ g^{-1}$, obtained using equation (6.17), versus E_{cell}

As shown in this figure, $c_{s,eff}$ is equal for both CDI and MCDI, however at $E_{cell} = 1.6\ V$ the MCDI cell gives a significantly higher deionization capacity, mostly because the CDI cell at this cell voltage has a low deionization efficiency.

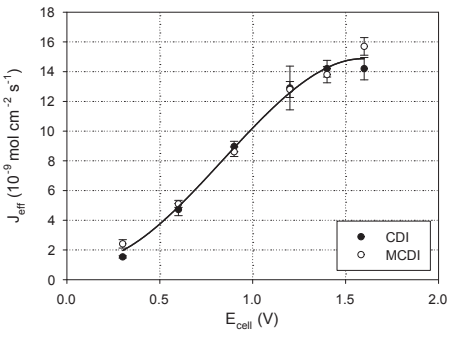

Figure 6.12: Effective deionization rate versus cell voltage for CDI cell and MCDI cell together with trend line

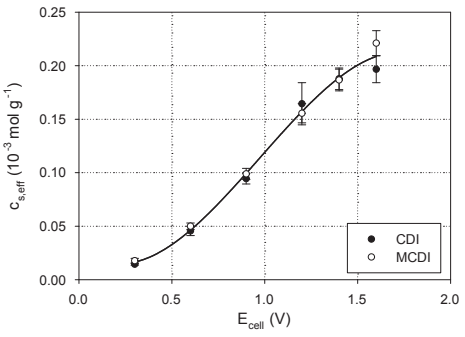

Figure 6.13: Effective deionization capacity versus cell voltage for CDI cell and MCDI cell together with trend line

6.5.2 Relation performance to existing cell configurations

To compare performance of the MCDI cell to other cell configurations, only literature was considered where experimental conditions for $c[NaCl]$ and carbon weight per unit cell area $\rho_{c,A}$ are similar to conditions used in this research (10 mM NaCl and 27 $mg\ cm^{-2}$ respectively). In most of the literature only effective deionization capacity $c_{s,eff}$ was reported. In these cases, deionization rate J is estimated by using the reported value of $\rho_{c,A}$ and by analyzing the charge / discharge plots to obtain the characteristic time $6\,\tau$. For some literature [8, 15, 16] no values for $\rho_{c,A}$ were reported, therefore values for J could not be obtained. Performance results are summarized table 6.5.2.

Table 6.2: Reported literature CDI performance and experimental conditions for various carbon electrode types compared to MCDI performance reported in this work

Electrode configuration	E_{cell} V	c[NaCl] mM	$c_{s,eff}$ $10^{-6}\ mol\ g^{-1}$	J_{eff} $10^{-9}\ mol\ cm^{-2}\ s^{-1}$	$\rho_{c,A}$ $mg\ cm^{-2}$	$6\,\tau$ s	
Aerogel	1.3	8.5	24	1.2	120	-	[14]
Aerogel	1.2	8.4	52	1.5[c]	15	500	[10]
Aerogel	0.9	8.4	0.17	-	-	-	[15]
Aerogel	1.2	2.5	77	-	-	-	[16]
Aerogel	1.4	4.5	110	-	-	-	[11]
Nanotubes	1.2	2.5	57	1.2[c]	15	750	[9]
Fibers	1.2	4.3	250	-	-	-	[8]
Fibers[a]	1.2	4.3	470	-	-	-	[8]
Powder[b]	0.9	10	100	8.6	22	210	[d]
Powder[b]	1.2	10	160	13	22	220	[d]
Powder[b]	1.4	10	190	14	22	230	[d]

[a] Titanium modified
[b] MCDI cell
[c] Estimated from reported $6\,\tau$ and $\rho_{c,A}$
[d] This work

This table shows that the MCDI cell performs better on $c_{s,eff}$ and J_{eff} in all cases except for the fiber materials. However, the fiber materials were tested in a batch reactor under ideal circumstances, it is unsure how they perform in a real CDI setup. Furthermore, fiber materials generally have a low bulk density, therefore volumetric capacity will be lower.

The factor 10 difference in J_{eff} between the MCDI cell and the aerogel and nanotube cell configurations can be attributed to the difference in flow channel thickness. High flow channel thickness will increase cell resistance, and therefore reduce J_{eff}. Since the ion-exchange membranes are insulators, thin spacers can be employed in the MCDI cell, which cannot be employed in the aerogel and nanotube cell configurations since then electrical short-circuit will occur.

6.6 Conclusion

A simple equivalent electrical circuit consisting of a capacitor in series with a resistor can be used to represent the kinetics of a (M)CDI cell. However, resistance values are not constant throughout the deionization cycle. In a CDI cell, more resistance is measured when charging as compared to discharging , while in a MCDI cell, the opposite is true, more resistance is measured when discharging as compared to charging. On average, both cell configurations result in an equal resistance. Since in a practical deionization setup the charge step will be rate limiting, by employing AMX / CMX ion-exchange membranes a 25 % increase in deionization rate can be achieved.

The relation between electrochemical characteristics and deionization performance can be translated into two efficiency parameters, coulombic efficiency CE and deionization efficiency Λ. The coulombic efficiency is related to the fraction of electrons used to generate charge on the system, and the deionization efficiency is related to the fraction of charge used to remove ions. When employing AMX / CMX membranes increased coulombic efficiency and deionization efficiency can be obtained at higher ($> 1.2\ V$) cell voltages.

Regarding deionization performance, when comparing the MCDI cell configuration with carbon aerogel CDI cells, a factor 10 higher deionization rate was found, together with a 36 % higher adsorption capacity. Furthermore, at a cell voltage of 1.6 V still a linear increase of deionization performance was found, therefore it is likely even higher cell voltages can be used.

Bibliography

[1] P. Długołęcki, K. Nymeijer, and S. Metz. Current status of ion exchange membranes for power generation from salinity gradients. *Journal of Membrane Science*, 319(1-2):214, 2008.

[2] R. D. Noble and S. A. Stern. *Membrane Separations Technology: Principles and Applications*. Elsevier Science, 1995.

[3] A. Ban, A. Schafer, and H. Wendt. Fundamentals of electrosorption on activated carbon for wastewater treatment of industrial effluents. *Journal of Applied Electrochemistry*, 28(3):227–236, 1998.

[4] H. Oda and Y. Nakagawa. Removal of ionic substances from dilute solution using activated carbon electrodes. *Carbon*, 41(5):1037–1047, 2003.

[5] Y. Oren and A. Soffer. Electrochemical parametric pumping. *Journal of the Electrochemical Society*, 125(6):869–875, 1978.

[6] A. Afkhami. Adsorption and electrosorption of nitrate and nitrite on high-area carbon cloth: an approach to purification of water and waste-water samples. *Carbon*, 41(6):1320–1322, 2003.

[7] H. J. Oh, J. H. Lee, H. J. Ahn, Y. Jeong, Y. J. Kim, and C. S. Chi. Nanoporous activated carbon cloth for capacitive deionization of aqueous solution. *Thin Solid Films*, 515(1):220–225, 2006.

[8] M. W. Ryoo, J. H. Kim, and G. Seo. Role of titania incorporated on activated carbon cloth for capacitive deionization of NaCl solution. *Journal of Colloid and Interface Science*, 264(2):414–419, 2003.

[9] X. Z. Wang, M. G. Li, Y. W. Chen, R. M. Cheng, S. M. Huang, L. K. Pan, and Z. Sun. Electrosorption of NaCl solutions with carbon nanotubes and nanofibers composite film electrodes. *Electrochemical and Solid-State Letters*, 9(9):E23–E26, 2006.

[10] J. C. Farmer, S. M. Bahowick, J. E. Harrar, D. V. Fix, R. E. Martinelli, A. K. Vu, and K. L. Carroll. Electrosorption of chromium ions on carbon aerogel electrodes as a means of remediating ground water. *Energy & Fuels*, 11(2):337–347, 1997.

[11] C. J. Gabelich, T. D. Tran, and I. H. Suffet. Electrosorption of inorganic salts from aqueous solution using carbon aerogels. *Environmental Science & Technology*, 36(13):3010–3019, 2002.

[12] H. H. Jung, S. W. Hwang, and S. H. Hyun. Capacitive deionization characteristics of nanostructured carbon aerogel electrodes synthesized via ambient drying. *Desalination*, 216(1-3):377, 2007.

[13] P. Rana-Madaria, M. Nagarajan, C. Rajagopal, and B. S. Garg. Removal of chromium from aqueous solutions by treatment with carbon aerogel electrodes using response surface methodology. *Industrial & Engineering Chemistry Research*, 44(17):6549–6559, 2005.

[14] P. Xu, J. E. Drewes, and D. Heil. Treatment of brackish produced water using carbon aerogel-based capacitive deionization technology. *Water Research*, 42(10-11):2605, 2008.

[15] C. M. Yang, W. H. Choi, and B. K. Na. Capacitive deionization of NaCl solution with carbon aerogel-silica gel composite electrodes. *Desalination*, 174(2):125–133, 2005.

[16] T. Y. Ying, K. L. Yang, S. Yiacoumi, and C. Tsouris. Electrosorption of ions from aqueous solutions by nanostructured carbon aerogel. *Journal of Colloid and Interface Science*, 250(1):18–27, 2002.

[17] M. J. Bleda-Martinez, J. A. Macia-Agullo, and D. Lozano-Castello. Role of surface chemistry on electric double layer capacitance of carbon materials. *Carbon*, 43(13):2677–2684, 2005.

[18] J. B. Lee, K. K. Park, H. M. Eum, and C. W. Lee. Desalination of a thermal power plant wastewater by membrane capacitive deionization. *Desalination*, 196(1-3):125–134, 2006.

[19] H. Li, Y. Gao, L. Pan, Y. Zhang, Y. Chen, and Z. Sun. Electrosorptive desalination by carbon nanotubes and nanofibres electrodes and ion-exchange membranes. *Water Research*, 42(20):4923–4928, 2008.

[20] J. C. Farmer, D. V. Fix, and G. V. Mack. Capacitive deionization of NaCl and $NaNO_3$ solutions with carbon aerogel electrodes. *Journal of the Electrochemical Society*, 143(1):159–169, 1996.

[21] H. P. Boehm. Surface oxides on carbon and their analysis: a critical assessment. *Carbon*, 40(2):145–149, 2002.

[22] E. Frackowiak and F. Beguin. Carbon materials for the electrochemical storage of energy in capacitors. *Carbon*, 39(6):937–950, 2001.

[23] F. Harnisch. The suitability of monopolar and bipolar ion exchange membranes as separators for biological fuel cells. *Environ. Sci. Technol.*, 42(5):1740–1746, 2008.

[24] J. S. Park, J. H. Choi, J. J. Woo, and S. H. Moon. An electrical impedance spectroscopic (EIS) study on transport characteristics of ion-exchange membrane systems. *Journal of Colloid and Interface Science*, 300(2):655, 2006.

[25] V. I. Zabolotsky and V. V. Nikonenko. Effect of structural membrane inhomogeneity on transport properties. *Journal of Membrane Science*, 79(2-3):181–198, 1993.

[26] J. Newman and K. E. Thomas-Alyea. *Electrochemical Systems*. John Wiley & Sons, Hoboken, 3rd edition, 2004.

[27] A.J. Bard and L.R. Faulkner. *Electrochemical Methods: Fundamentals and Applications*. Wiley, New York, 2nd edition, 2001.

[28] M. Z. Bazant, K. Thornton, and A. Ajdari. Diffuse-charge dynamics in electrochemical systems. *Physical Review E*, 70(2):021506, 2004.

[29] M. Mulder. *Basic Principles of Membrane Technology*. Springer, 1996.

[30] L. Bonnefoi, P. Simon, and J. F. Fauvarque. Electrode optimisation for carbon power supercapacitors. *Journal of Power Sources*, 79(1):37–42, 1999.

Chapter 7

Effect ionic species on deionization performance and efficiency

7.1 Summary

In this chapter, the effect of the ionic species comprising the electrolyte on performance is investigated. This is done by comparing the deionization performance with a broad range of electrolytes to the deionization performance with a sodium chloride electrolyte.

When taking into account the valence and the specific conductivity of the ionic species comprising the electrolyte, most electrolytes gave an equal deionization performance to sodium chloride. For electrolytes containing only monovalent ions, anode charge capacity is limiting, and for electrolytes containing bivalent ions, cathode charge capacity is limiting. Only sodium hydroxide and sodium phosphate gave deviating results, the performance of the CDI cell changed irreversibly after investigating these electrolytes. This is because the used ion-exchange membranes were not resistant to the high pH of the sodium hydroxide electrolyte, and due to speciation of phosphate during the experiment with the sodium phosphate electrolyte.

7.2 Introduction

An electrolyte is defined as a solution containing ionic species. These ionic species can be divided in two groups, species that are removed from a liquid due to redox reactions, which are mostly heavy metals [1–6], and ionic species that are removed from a liquid due to electrosorption, such as nitrates [7, 8], sulfur containing ions [9], and various other ions [6, 8, 10–12]. Literature studies showed that the valence of the ionic species in the electrolyte dictates the amount of charge needed to adsorb one mole of those ions. For example, two moles of charge are needed to adsorb one mole of bivalent ions, together with two moles of monovalent counterions, or one mole of bivalent counterions. The (hydrated) size of the ion has no effect on deionization capacity [12].

In this chapter, the effect of electrosorption of various ion species on deionization performance and efficiency is investigated. This is done to confirm the findings from

van Limpt, B., Bruning, H., Rulkens, W.H.

literature, and to investigate the effect of ion species on deionization rate, charge efficiency and deionization efficiency.

Since anions and cations cannot be removed independently, sodium or chloride ions were used as a counter ion. The electrolytes under investigation were a base (NaOH) and an acid (HCl), electrolytes containing the major nutrients (KCl, NH_4Cl, $NaNO_3$ Na_2SO_4, Na_2HPO_4) and electrolytes containing hardness ions ($CaCl_2$, $MgCl_2$). Furthermore, it was assessed whether a electrolyte containing two bivalent ions ($MgSO_4$) gives different performance relations as an electrolyte consisting of a bivalent ion with monovalent counter ions [12] ($MgCl_2$). Electrolytes containing mixtures of different ionic species were not part of the investigation, the method as developed in chapter 6 relies on using conductivity as a measure for concentration. For mixtures the relation between conductivity and concentration no longer holds, since the ratio between ionic species is not known.

To monitor for any irreversible effects of the electrolyte on deionization, a reference experiment with a NaCl electrolyte between investigations of the electrolytes. A change in the results of the reference experiment indicates a irreversible effect of the previously investigated electrolyte. Another purpose of the reference experiments is that all results can be normalized toward the performance with a NaCl electrolyte.

7.3 Materials and methods

7.3.1 Setup

The experimental setup as described in chapter 6 was used, which consists of four repeating CDI cells. However, different electrodes and membranes were employed.

The electrodes were constructed using the electrode production technique discussed in chapter 5, and after construction consisted of 86 w% A Supra Eur (Norit, Amersfoort, The Netherlands), and 14 w% PVDF. Thickness of one electrode was 270 ± 10 μm and the area was 33.44 cm^2. The weight of carbon per unit cell area $\rho_{c,A}$ was 21.3 ± 0.8 mg carbon cm^{-2} cell. In the carbon weight per unit cell area, only the amount of A Supra Eur per square centimeter cell was considered.

The ion-exchange membranes used were Neosepta AM1 and CM1 membranes. Characteristics of the membranes are summarized in table 7.1. Characteristics were obtained at 0.5 M NaCl [13], and are highly concentration dependent [14, 15]. As can be seen when comparing the characteristics of the AM1/CM1 membranes to the characteristics of the AMX/CMX membranes as shown in chapter 6 table 6.1, the AM1/CM1 membranes have lower electrical resistance and a comparable permselectivity.

Table 7.1: Physical and electrical characteristics of the used Neosepta membranes

Item	AM1	CM1	Reference
Permselectivity	92	97	[13]
Electric resistance ($\Omega\ cm^2$)	1.8	1.7	[13]
Thickness (mm)	0.13	0.13	Measured

7.3.2 Experiments

Electrolytes

The electrolytes under investigation were solutions of the acid hydrogen chloride (HCl) the base sodium hydroxide (NaOH), the nutrients potassium chloride (KCl), ammonium chloride (NH_4Cl), sodium nitrate ($NaNO_3$), sodium sulfate (Na_2SO_4), sodium phosphate (Na_2HPO_4), the hardness salts calcium chloride ($CaCl_2$) and magnesium chloride ($MgCl_2$), and the bivalent salt magnesium sulfate ($MgSO_4$). All used salts were analytical grade (Boom, Meppel, The Netherlands).

For each electrolyte, a 0.01 M concentration was investigated. Conductivity and pH before each experiment were recorded, since conductivity has an effect on deionization rate; a higher conductivity results in a lower total cell resistance and therefore a higher deionization rate, and changes in pH have an effect on membrane characteristics [14].

Experimental procedure

The experimental procedure as described in section 6 was followed to obtain the average resistance R, the deionization capacity C, the deionization efficiency Λ and the coulombic efficiency corrected for the characteristic time of the system, $CE_{3\tau}$. These parameters can be used to obtain effective deionization rate J_{eff} and the effective deionization capacity $c_{s,eff}$ by taking into account the valence of the electrolyte, or the amount of electrons needed to adsorb at least one cation or one anion.

All experiments were performed at a cell voltage of 1.2 V, and at least 4 cycles of 30 minutes were performed to ensure steady state response. Steady state was verified by comparing results of the second through the fourth cycle. If the results remained constant, steady state response was assumed.

Before each experiment with an electrolyte under investigation, the performance with a NaCl electrolyte was determined, and thereby any irreversible effects on the CDI cells could be monitored. The obtained steady state performance was normalized toward the performance of the NaCl experiment preceding the actual experiment of the electrolyte under investigation to correct for changes in performance over time.

This is done by dividing the obtained capacity and resistance for the investigated electrolyte by respectively the capacity and resistance of the preceding NaCl experiment, to obtain normalized charge capacity C/C_{NaCl} and normalized resistance R/R_{NaCl}.

$c_{s,eff}$ and J_{eff} were not normalized toward the performance of the preceding NaCl experiment to obtain the actual deionization capacity and deionization rate.

7.4 Results and discussion

7.4.1 pH and conductivity

Table 7.2 shows measured pH and conductivity for each electrolyte solution at 0.01 M.

Table 7.2: Used electrolyte solutions showing electrolyte valence together with average influent pH and conductivity

Solution	Salt valence (z)	pH	Conductivity ($mS\ cm^{-1}$)
NaCl	1	6.8	1.17
HCl	1	2	4.07
NaOH	1	12	2.35
KCl	1	6.8	1.4
NH_4Cl	1	6.9	1.39
$NaNO_3$	1	6.6	1.12
Na_2SO_4	2	7	2.07
Na_2HPO_4	1.97 [a]	8.5	1.23
$CaCl_2$	2	6.6	2.31
$MgCl_2$	2	6.6	2.23
$MgSO_4$	2	6.8	1.55

As shown in this table, the HCl and NaOH electrolyte had a pH clearly deviating from neutrality. Furthermore, the electrolyte valence of Na_2HPO_4 was not exactly 2 at the experimental conditions. This is since phosphate is a weak base, and at pH 8.5 part of the phosphate is present in the monovalent form ($H_2PO_4^-$). This also means that pH changes during the experiment result in a change in the electrolyte valence z, which has to be taken into consideration when reviewing the results.

Regarding conductivity, there is a moderate variation in conductivity for all electrolytes, due to the different mobilities of the separate ions [16]. For the monovalent electrolytes ($z = 1$) except HCl and NaOH, conductivities were very similar. The differences in conductivity have to be taken into account when investigating resistance.

7.4.2 Species

Figure 7.1 shows normalized charge capacity C/C_{NaCl} for all investigated electrolytes. As shown in the figure, the normalized charge capacity for strong acid (HCl) and strong base (NaOH) were relatively high, due to the very small size of the hydrogen and hydroxyl ion [17]. The higher capacity for a strong acid and a strong base is also reported in supercapacitor literature [18, 19], and is one of the reasons strong acids and bases are used as electrolyte in supercapacitors.

When considering the monovalent binary electrolytes besides HCl and NaOH, results indicate that the chlorine ion is limiting the normalized charge capacity, all electrolytes containing chlorine resulted in a similar normalized charge capacity, while $NaNO_3$ yielded a slightly higher normalized charge capacity. The normalized charge capacity of $NaNO_3$ was again equal to the normalized charge capacity of Na_2SO_4 and Na_2HPO_4, indicating that adsorption of sodium limits the normalized charge capacity for electrolytes containing both bivalent as well as monovalent ions. This is confirmed when considering $MgSO_4$, here capacity was equal to $MgCl_2$ and $CaCl_2$ but higher than Na_2SO_4 and Na_2HPO_4. This indicates that for the investigated monovalent binary electrolytes the normalized charge capacity is limited by the adsorption capacity of the anode, while for the investigated bivalent electrolytes the normalized charge capacity is limited by the adsorption capacity of the cathode.

Figure 7.2 shows the normalized deionization rate for all investigated electrolytes. As shown in the figure, all normalized results were close to the results from the preceding NaCl experiments except for sodium hydroxide and Na_2HPO_4. In section 7.4.3 these two species are discussed further. $MgSO_4$ also showed slightly higher resistance than the other electrolytes containing bivalent ions. This can be explained by the lower specific conductivity of $MgSO_4$ as compared to other electrolytes containing bivalent ions, as shown in table 7.2. Another observation is that HCl showed a relatively high normalized resistance, while specific conductivity as shown in 7.2 is very high. Possibly the membranes are affected by the low pH.

Figure 7.3 shows the deionization efficiency Λ for all investigated electrolytes. As shown in this figure, most species gave an deionization efficiency of around 80 %. Only sodium hydroxide gave a low deionization efficiency. This means that a large fraction of the charge was not used for deionization. For Na_2HPO_4, an efficiency close to 100 % was measured. The pH during the experiment dropped, which reduces the effective value for electrolyte valence z (more phosphate is in the $H_2PO_4^-$ form) resulting in the relatively high value for deionization efficiency.

Figure 7.4 shows the coulombic efficiency $CE_{3\tau}$ for all investigated electrolytes. As can be seen from this figure, only sodium hydroxide gave a lower coulombic efficiency, however given the high standard deviation this does not seem significant.

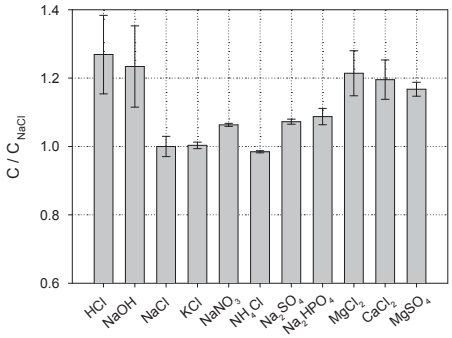

Figure 7.1: Charge capacity for all investigated electrolytes normalized toward capacity of the preceding NaCl experiment

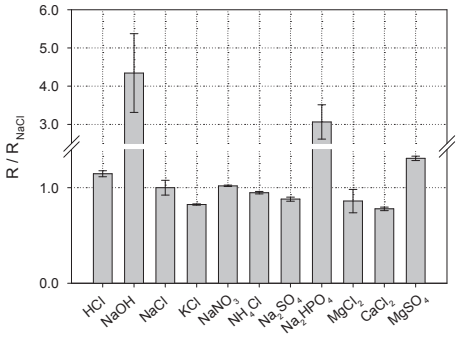

Figure 7.2: Resistance for all investigated electrolytes normalized toward resistance of the preceding NaCl experiment

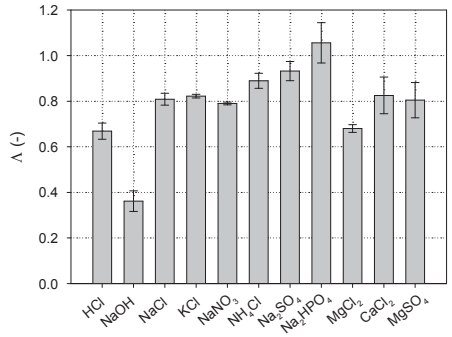

Figure 7.3: Deionization efficiency for all investigated electrolytes

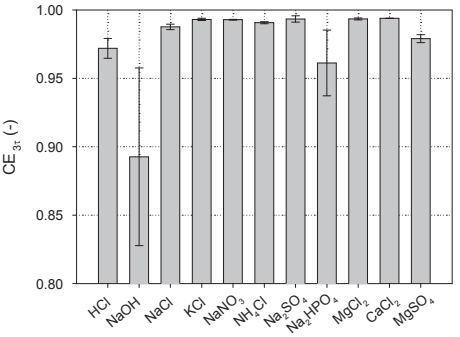

Figure 7.4: Coulombic efficiency for all investigated electrolytes

Figure 7.5 shows the effective deionization capacity $c_{s,eff}$ for all investigated electrolytes, obtained by combining figures 7.3 and 7.4.

Figure 7.6 shows the effective deionization rate J_{eff} for all investigated electrolytes, obtained by combining figures 7.2 and 7.4.

As shown in figure 7.5, all monovalent binary electrolytes except sodium hydroxide give a constant effective deionization capacity of approximately 0.2 10^{-3} $mol\ g^{-1}$, and all bivalent electrolytes give a constant effective deionization capacity of approximately 0.12 10^{-3} $mol\ g^{-1}$. As can be seen from figure 7.6, variation between species is high for effective deionization rate. For sodium hydroxide and Na_2HPO_4 only a very low effective deionization rate can be obtained.

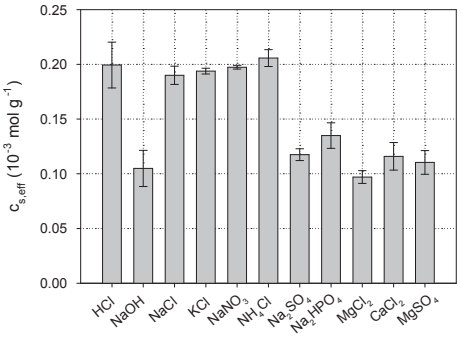

Figure 7.5: Effective deionization capacity for all investigated electrolytes

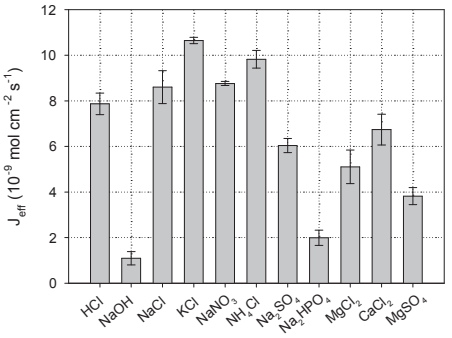

Figure 7.6: Effective deionization rate for all investigated electrolytes

7.4.3 Stability

To investigate the long term stability of results generated by the deionization setup, the capacity of the performed NaCl experiments was monitored in time. Capacity was investigated instead of resistance to obtain an indication of stability, since charge capacity measurements were more precise and for resistance the same trend was observed as for capacity.

Figure 7.7 shows the normalized capacity for all performed NaCl experiments. Normalization is done versus the average NaCl capacity C_{mean} of 18.9 ± 0.6 F g^1 carbon electrode.

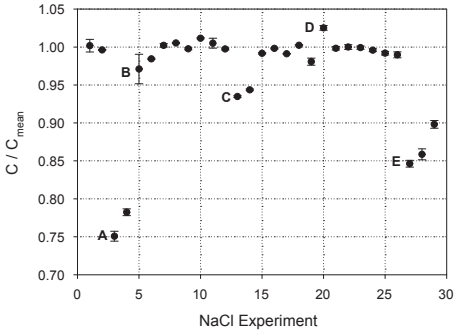

Figure 7.7: Normalized deionization capacity for all performed NaCl experiments. **A** indicates the first experiment after investigation of NaOH, **B** indicates renewal CDI cell, **C** indicates nitrogen purging was disabled, **D** indicates second renewal CDI cell, **E** indicates the first experiment after investigation of Na_2HPO_4 electrolyte.

NaCl experiment 1 is the first NaCl experiment performed, NaCl experiment 29 is the last NaCl experiment performed. Between the NaCl experiments, experiments with the electrolytes as summarized in table 7.2 were performed. Most investigated electrolytes had no effect on stability, therefore only when a certain electrolyte had an effect on stability it is indicated in the graph.

In figure 7.7 **A** indicates experiment 3, the first experiment after investigation of NaOH. After investigation of NaOH, deionization capacity drops by 25 %, and only recovers very slowly, experiment 4 still has a 22 % lower capacity than average. This effect was also seen on resistance, for experiments 3 and 4 resistance increased by approximately 70 %.

After opening the CDI cell, it was noticed that the AM1 anion exchange membranes changed in appearance, as shown in figure 7.8. As shown in this figure, the color of the membrane changed from translucent to brownish, especially in the center of the membrane. This indicates that the ion exchange properties changed during the experiments. It can be concluded that the used membranes cannot handle the very high pH, at 0.01 M NaOH pH is 12. Supplier information confirms that AM1 membranes are negatively affected by high pH solutions.

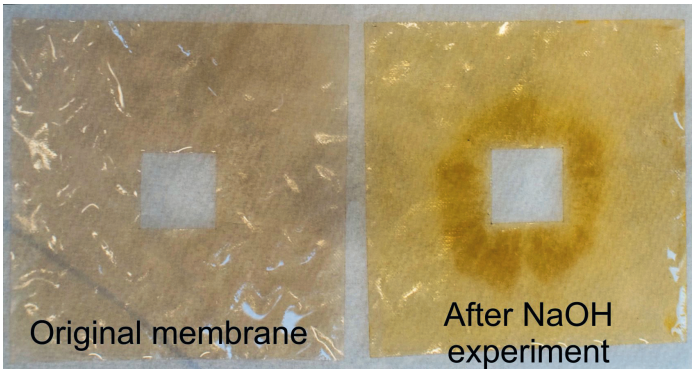

Figure 7.8: Original AM1 membrane and AM1 membrane after experiment with NaOH

After changing the membranes and electrodes in the CDI cell, indicated in figure 7.7 as the first **B** before experiment 5, the deionization capacity became stable again. Capacity dropped slightly (6 %) after experiment 12, indicated as **C** in figure 7.7. Here, nitrogen purging of the influent solution was disabled. The reduction of capacity is attributed to dissolved oxygen [8]. Nitrogen purging was re-enabled from experiment 15 onward.

After experiment 19, the membranes and electrodes in the CDI cell were replaced, indicated in figure 7.7 as **D**.

In figure 7.7 **E** indicates the first experiment after investigation of Na_2HPO_4, experiment 27. As is shown in this figure, Na_2HPO_4 also negatively influences stability of the experiments, capacity dropped by 15 %, and resistance increased by approximately 100 %. The decrease in capacity can be attributed to retained Na_2HPO_4 in the electrode compartment, since after experiment 27, capacity and resistance slowly returned to their average value. Visual inspection of the membranes after experiment 29 did not shown any membrane degradation like was observed after the experiment with NaOH.

7.5 Conclusion

When deionizing electrolytes containing ionic species other than sodium chloride, the following issues have to be considered when an indication for performance is needed:

- For electrolytes containing bivalent ions, cathode charge capacity is limiting; an electrolyte containing monovalent cations and a bivalent anion shows lower normalized charge capacity than an electrolyte containing a bivalent cation and monovalent anions. When the electrolyte contains a bivalent anion and a bivalent cation, the charge capacity is equal to an electrolyte containing a bivalent cation and monovalent anions.

- For electrolytes containing only monovalent ions, anode charge capacity is limiting; a nitrate electrolyte yields a higher normalized charge capacity than chloride electrolytes. More experiments with electrolytes containing anions other than chloride or nitrate are needed to confirm this finding.

- Deionization of solutions with high pH can irreversibly damage the used membranes.

- Deionization of weak acids and weak bases seems possible, however speciation of these species with pH has to be taken into account. This also means that using conductivity as a measure for concentration results in less accurate results.

When taking the above issues into account, performance of electrolytes other than sodium chloride show remarkably close performance and efficiency to sodium chloride. This means that in general the proposed double-layer model in chapter 3 can be used to predict deionization capacity of any common electrolyte, and that the resistance relations found in chapter 4 can be used to predict deionization rate.

Bibliography

[1] A. Afkhami and B. E. Conway. Investigation of removal of Cr(VI), Mo(VI), W(VI), V(IV), and V(V) oxy-ions from industrial waste-waters by adsorption and electrosorption at high-area carbon cloth. *Journal of Colloid And Interface Science*, 251(2):248–255, 2002.

[2] A. Alfarra, E. Frackowiak, and F. Beguin. Mechanism of lithium electrosorption by activated carbons. *Electrochimica Acta*, 47(10):1545–1553, 2002.

[3] A. Brennsteiner, J. W. Zondlo, A. H. Stiller, P. G. Stansberry, D. C. Tian, and Y. Xu. Environmental pollution control devices based on novel forms of carbon: Heavy metals. *Energy & Fuels*, 11(2):348–353, 1997.

[4] J. C. Farmer, S. M. Bahowick, J. E. Harrar, D. V. Fix, R. E. Martinelli, A. K. Vu, and K. L. Carroll. Electrosorption of chromium ions on carbon aerogel electrodes as a means of remediating ground water. *Energy & Fuels*, 11(2):337–347, 1997.

[5] M. M. Goldin, A. G. Volkov, and D. N. Namychkin. Adsorption of copper, silver, and zinc cations on polarized activated carbons. *Journal of the Electrochemical Society*, 152(5):E167–E171, 2005.

[6] H. Oda and Y. Nakagawa. Removal of ionic substances from dilute solution using activated carbon electrodes. *Carbon*, 41(5):1037–1047, 2003.

[7] A. Afkhami. Adsorption and electrosorption of nitrate and nitrite on high-area carbon cloth: an approach to purification of water and waste-water samples. *Carbon*, 41(6):1320–1322, 2003.

[8] J. C. Farmer, D. V. Fix, and G. V. Mack. Capacitive deionization of NaCl and $NaNO_3$ solutions with carbon aerogel electrodes. *Journal of the Electrochemical Society*, 143(1):159–169, 1996.

[9] E. Ayranci and B. E. Conway. Adsorption and electrosorption at high-area carbon-felt electrodes for waste-water purification: Systems evaluation with inorganic, S-containing anions. *Journal of Applied Electrochemistry*, 31(3):257–266, 2001.

[10] A. Ban, A. Schafer, and H. Wendt. Fundamentals of electrosorption on activated carbon for wastewater treatment of industrial effluents. *Journal of Applied Electrochemistry*, 28(3):227–236, 1998.

[11] J. C. Farmer, D. V. Fix, and G. V. Mack. Capacitive deionization of NH_4ClO_4 solutions with carbon aerogel electrodes. *Journal of Applied Electrochemistry*, 26(10):1007–1018, 1996.

[12] C. J. Gabelich, T. D. Tran, and I. H. Suffet. Electrosorption of inorganic salts from aqueous solution using carbon aerogels. *Environmental Science & Technology*, 36(13):3010–3019, 2002.

[13] P. Długołęcki, K. Nymeijer, and S. Metz. Current status of ion exchange membranes for power generation from salinity gradients. *Journal of Membrane Science*, 319(1-2):214, 2008.

[14] F. Harnisch. The suitability of monopolar and bipolar ion exchange membranes as separators for biological fuel cells. *Environ. Sci. Technol.*, 42(5):1740–1746, 2008.

[15] V. I. Zabolotsky and V. V. Nikonenko. Effect of structural membrane inhomogeneity on transport properties. *Journal of Membrane Science*, 79(2-3):181–198, 1993.

[16] P. W. Atkins and J. de Paula. *Atkins' Physical Chemistry*. Oxford University Press, Oxford, 7th edition, 2002.

[17] E. R. Nightingale. Phenomenological theory of ion solvation. effective radii of hydrated ions. *The Journal of Physical Chemistry*, 63(9):1381–1387, 1959.

[18] B. E. Conway. *Electrochemical Supercapacitors, Scientific Funcamentals and Technological Applications*. Kluwer Academic / Plenum Publishers, New York, 1st edition, 1999.

[19] E. Frackowiak and F. Beguin. Carbon materials for the electrochemical storage of energy in capacitors. *Carbon*, 39(6):937–950, 2001.

Chapter 8

Prediction of CDI behavior by implementation of equivalent circuit modeling

8.1 Summary

To predict CDI behavior, a mass and charge transport model was constructed based on the implementation of equivalent circuit modeling. This was done by coupling a bulk transport model based on convection, with an adsorption model based on the time domain response of the transmission line model. In both models, the relations between cell design, electrolyte characteristics and performance and efficiency were used as determined in this thesis. The concentration response of CDI units with membranes as well as CDI units without membranes was validated, and found that some adjustments are needed due to mass transport limitation resulting from cell design and membrane characteristics. Furthermore, it is confirmed that the RC fitting procedure as used in chapters 6 and 7 closely resembles the transmission line model.

8.2 Introduction

CDI is a complex process, where many operational parameters have an effect on the deionization performance. These operational parameters include the composition of the influent, the construction of the electrodes, and the mode of operation. All these parameters will impact the concentration of the effluent, the energy use and the deionization rate. To predict the effect of operational parameters on CDI behavior, a kinetics model of the total CDI process is constructed that predicts CDI performance. This model can be used to perform sensitivity analysis on stack design and quality control of actual CDI cell configurations.

Figure 8.1 shows a presentation of the deionization process. As shown in this figure, two processes can be distinguished. The first process is the bulk mass transport of ions through the CDI cell. In most applications of CDI, including the application as discussed in chapters 6 and 7, this transport is by forcing a solution through a spacer compartment between two parallel electrode compartments, where the electrode compartments comprise of a carbon electrode and a membrane. To model this bulk mass

van Limpt, B., Bruning, H., Rulkens, W.H.

transport, plug flow behavior is used. In existing literature [1], CSTR behavior was assumed, however plug flow behavior is a more accurate representation of a laminar flow between two parallel electrodes [2].

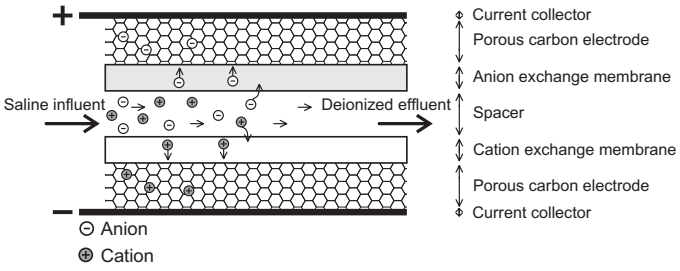

Figure 8.1: Presentation of the CDI cell configuration depicting the deionization process

The second process is ion adsorption. When a potential difference is set across the spacer compartment, ions will be removed from the solution in the spacer compartment due to the induced electric field, and adsorbed onto the carbon electrodes. To model ion adsorption, the transmission line kinetics as derived in chapter 2 is used, as is also used in existing modeling [3]. Since these kinetics are based on charge transport, this charge transport needs to be related to mass transport.

To ensure a close link between model and the actual design of a deionization setup, the validated relations between experimental characteristics and performance as discussed in chapters 3 through 5 will be included. With these relations the physical properties of the deionization setup such as the used carbon and thickness of the spacer compartment can be transformed to electrical properties such as resistance and capacitance that can be used in the modeling. Furthermore, experimental relations between cell design and deionization efficiency as discussed in chapters 6 and 7 will be included. With these relations efficiency parameters can be incorporated in the modeling.

Validation of the constructed model is performed by comparing modeling results with actual experimental results, both for a membrane cell configuration (MCDI cell configuration) as for a cell configuration without membranes (CDI cell configuration). Differences between model and experimental results will be evaluated by investigating which model parameter is responsible for the measured difference. This will give an indication how both model and experiment can be improved. The model will also be used to validate the simplified RC fitting procedure as used in chapter 6 and 7 by comparing RC fit results to model predictions. Finally, sensitivity analysis will be performed to assess the effect of transmission line kinetics on (M)CDI results, and will investigate the effect of the dead volume of the CDI setup.

8.3 Theory

8.3.1 General model

Figure 8.2 shows the mass and charge transport for a (M)CDI cell configuration. Only the deionization process and not the regeneration process is considered, but the model is valid for both deionization (charging) as well as regeneration (discharging). In this figure, on the left hand side the actual process is shown and on the right hand side the mathematical equivalent of the process. In case of a symmetrical binary salt, adsorption of a cation is always linked to adsorption of an anion. This means the cell is symmetrical, as shown in the figure as the symmetry line. From figure 8.2 two transport processes can be distinguished.

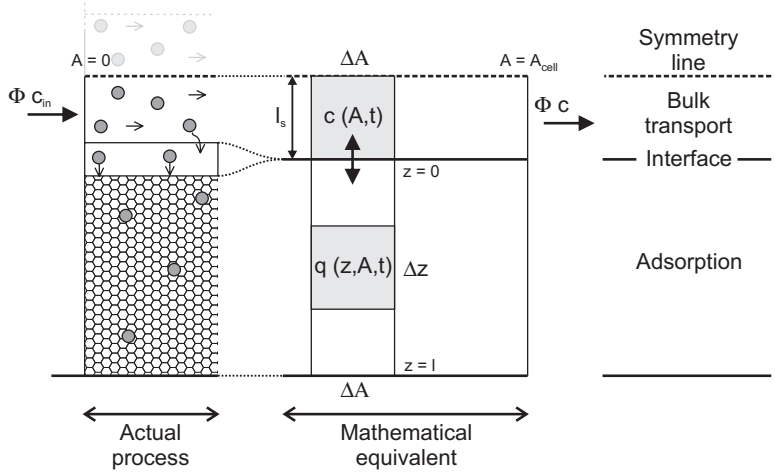

Figure 8.2: Mass and charge transport in a (M)CDI cell configuration

The first transport process is bulk transport, or the transport of ions through the spacer with effective thickness l_s in cm. A flow with flow rate Φ in $cm^3\ s^{-1}$ and salt concentration c_{in} in $mol\ cm^{-3}$ enters the cell at $A = 0$, and is transported through the spacer compartment. A is hereby expressed as the amount of area that is flowed through, it is assumed that the shape of the spacer has no effect on deionization kinetics. During transition, concentration c in $mol\ cm^{-3}$ changes due to adsorption and at $A = A_{cell}$ the deionized solution leaves the cell, where A_{cell} is the total cell area in cm^2. Therefore concentration is considered as a function of time t in s and of area A, in cm^2, flowed through, independent of the configuration of the cells. In practice the configuration of the cells can have some influence on performance, a stack of many small cells can behave differently than a stack of just one cell. Furthermore, depending

on the configuration of the cells the hydrodynamics in the spacer compartment can differ.

The second transport process is adsorption, or more specifically the transport of ions from the spacer compartment toward the carbon surface where actual adsorption takes place. In chapter 2 a model was developed for the adsorption of ions onto a carbon surface in terms of charge, and in chapter 5 it was shown that carbon electrode characteristics can be easily linked to this model. Therefore instead of developing a model for transport of ions in the electrode, which is in this case untestable since the concentration of ions in the electrode compartment cannot be measured, adsorption is considered as charge transport in a transmission line model. Charge q, in $C\ cm^{-3}$, is modeled as function of position in the CDI cell A, in cm^2, time t in s, and position in the transmission line z in cm. It must be noted that this is only valid for single salt solutions, when mixtures are being deionized, charge transport can no longer be considered equivalent to mass transport. Furthermore, the position of charge in the transmission line z is not related to the position of ions in the carbon electrode as suggested in figure 8.2, as already discussed in chapter 2 other distribution models can result in similar charge transport behavior.

To link the bulk mass transport to the adsorption charge transport, a hypothetical interface is defined at $z = 0$ where charge transport and mass transport are linked by the efficiency parameter Λ as defined in chapter 6, or the equivalent of charge needed to adsorb one equivalent of mass. The influence of the membrane on the adsorption process will be considered as a constant resistance to charge transport, as also measured in chapter 6. For a more accurate representation of ion transport through a membrane, existing membrane transport models can be inserted into the existing model, however this is beyond the scope of this thesis.

8.3.2 Bulk transport

Equation (8.1) shows the continuity equation for bulk transport as depicted in figure 8.2.

$$\frac{dc}{dt} + \frac{1}{l_s}\frac{dc_a}{dt} + \frac{\Phi}{l_s}\frac{dc}{dA} = 0 \tag{8.1}$$

In this equation, c_a is the amount of adsorbed salt in $mol\ cm^{-2}$ cell area. Diffusion is not considered in the bulk transport, in practice concentration gradients will arise in the spacer compartment, resulting in diffusion of ions. However, at the relatively high flow rates Φ as used in the experiments, the effect of diffusion on bulk transport is minimal [3].

When taking that at $t = 0$ the entire CDI cell filled with influent solution, and no

salt is adsorbed onto the electrodes, boundary and initial conditions can be defined according to equations (8.2) through (8.4).

$$c(A=0) = c_{in} \tag{8.2}$$
$$c(t=0) = c_{in} \tag{8.3}$$
$$c_a(t=0) = 0 \tag{8.4}$$

The initial condition stated in equation (8.3) is dependent on the situation, for example when the cell is filled with clean water from the start ($c(t=0)=0$).

8.3.3 Interface

The interface describes the relation between charge transport and mass transport, and therefore between total charge on the carbon electrodes Q in $C\ cm^{-2}$ cell area and the amount of adsorbed salt c_a. The balance between change in adsorbed salt onto the electrodes dc_a and change in electrode charge dQ is shown in equation (8.5).

$$\frac{zF}{\Lambda}\frac{dc_a}{dQ} = 1 \tag{8.5}$$

In this equation, zF is the theoretical amount of charge needed to adsorb one mole of salt, and Λ is the deionization efficiency as discussed in chapter 6, or the fraction of electrons effectively used to adsorb ions. For Λ the relations as found in chapter 6 were used, meaning that a constant Λ was used when ion-exchange membranes were employed, and when not employing ion-exchange membranes the potential dependency of Λ was used as depicted in chapter 6 figure 6.11.

8.3.4 Charge transport

General

Figure 8.3 shows a presentation of the charge transport in a CDI cell. On the left hand side of the figure, the driving force for adsorption is shown which is the applied cell voltage E_{cell} in V minus the electrode potential E_C in V. The electrode potential E_C is dependent on the amount of charge present on the electrodes and the specific capacity C_V of the electrode, in $F\ cm^{-3}$. As more charge accumulates on the electrode and therefore more ions are removed from the electrolyte, E_C increases until E_C is equal to E_{cell}, at which point the adsorption stops.

The rate of adsorption, or the current that flows through the CDI cell, is dependent on the resistance of the CDI cell. When there is no charge on the electrodes, the resistance is equal to the external resistance R_{ext}, in $\Omega\ cm^{-2}$, which is the total

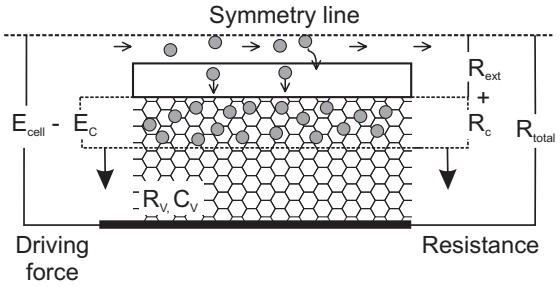

Figure 8.3: Potential distribution in CDI cell

resistance R_{total} minus the electrode resistance R_C. During charging, due to the specific resistance of the electrode R_V, in $\Omega\ cm$, the electrode resistance R_C increases. When the electrodes are fully charged, the resistance is equal to R_{total}.

The charge transport as described in figure 8.3 is depicted in equation (8.6).

$$\frac{dQ}{dt} = \frac{E_{cell} - E_C}{R_{ext} + R_C} \tag{8.6}$$

In equation (8.6) R_C and E_C are dependent on transmission line kinetics. To obtain these transmission line kinetics, the time response of the transmission line can be derived, similar as performed by Johnson et al. [3] but more in line with calculations of De Levie [4] as presented in chapter 2.

Time response transmission line

In section 2.A.1 the differential equations describing the linear De Levie transmission line model (linear TLM) were derived. These are shown in equations (8.7) through (8.8).

$$\frac{de}{dz} + iR_V = 0 \tag{8.7}$$

$$\frac{di}{dz} + \frac{e}{Z_p(\omega)} = 0 \tag{8.8}$$

In these equations, e is the potential in V, i is the current density in $A\ cm^{-2}$, R_V is the volumetric resistance in $\Omega\ cm$, $Z_p(\omega)$ is the specific impedance of the TLM in $\Omega\ cm$, ω is the frequency in s^{-1} and z is the position in the TLM in cm. To remove the frequency dependent specific TLM impedance, C_V is introduced as the differential volumetric capacitance in $F\ cm^{-3}$ according to equation (8.9) and considering that the potential drop over $Z_p(\omega)$ is equal to the current in $A\ cm^{-1}$ running through capacitor C_V according to equation (8.10) (also see section 2.A).

$$C_V = \frac{dq}{de} \tag{8.9}$$

$$i = \frac{dq}{dt} = \frac{e}{Z_p(\omega)} \tag{8.10}$$

When the equations (8.7) through (8.10) are combined the time based response of the transmission line is obtained, as shown in equation (8.11).

$$\frac{dq}{dt} = \frac{d}{dz}\left(\frac{1}{R_V C_V}\frac{dq}{dz}\right) \tag{8.11}$$

When taking a constant R_V and C_V with respect to z, as in the case of the linear TLM, equation (8.11) can be simplified into equation (8.12).

$$\frac{dq}{dt} = \frac{1}{R_V C_V}\frac{d^2q}{dz^2} \tag{8.12}$$

The boundary conditions for this equation are similar to those stated in section 2.A.1, and shown in equations (8.13) and (8.14).

$$\frac{dq}{dz}(z = l) = 0 \tag{8.13}$$

$$\frac{dq}{dt}(z = 0) = \frac{E_{cell} - E_C}{R_{ext}} \tag{8.14}$$

$$E_C = f(q, S\rho_{c,A}) \tag{8.15}$$

In these equations, L is the total length of the TLM in cm as also depicted in figure 8.2, E_{cell} is the externally applied potential in V, and R_{ext} is the external resistance in $\Omega\ cm^2$, and E_C is the double-layer potential, which is a function (f) of charge q and specific double-layer area $S\rho_{c,A}$ in m^2 double-layer area per cm^2 cell area as shown in equation (8.15), and further discussed in section 8.B.

The external resistance R_{ext} is defined according to equation (8.16) (obtained from chapter 4).

$$R_{ext} = R_s + R_{ct} + R_m \tag{8.16}$$

$$R_s = \frac{l_s}{\sigma} + R_0 A_{cell} \tag{8.17}$$

$$R_{ct} = \frac{1}{k_{T,ct}\Delta T + 1}\frac{1}{\beta\sqrt{c}} \tag{8.18}$$

In this equation, R_s is the system resistance consisting of contact resistance R_0 in Ω and effective spacer compartment thickness l_s in cm. R_{ct} is the charge-transfer

resistance with temperature correction factor $k_{T,ct}$ in K^{-1}, ΔT is the deviation in temperature from 298.15 K in K, and the empirical charge transfer performance β in $\Omega^{-1}\ mol^{-0.5}\ cm^{-0.5}$, and R_m is membrane resistance in $\Omega\ cm^2$. Since conductivity σ changes with concentration c, a procedure is implemented that returns σ as function of c, based on model calculations (Stream Analyzer 2.0, OLI Systems Inc.).

Equations (8.12) through (8.14) show that the charging of the transmission line in time resembles a diffusion process with diffusion constant $1/R_V C_V$ in s^{-1}. This makes sense, since R_V is related to resistance of the solution (chapter 4 and 5) and therefore to the inverse diffusion constant of the ions. So the higher R_V, the slower the diffusion of ions into the TLM. Since C_V is related to the amount of ions that can be stored in the carbon, the higher C_V the slower the carbon will be saturated with ions, and therefore the slower the diffusion of ions into the TLM.

To obtain the change in total charge versus time (dQ/dt) equation (8.12) is integrated over $z = 0$ through $z = l$, as shown in equation (8.19)

$$\frac{dQ}{dt} = \int_0^l \frac{dq}{dt} dz \tag{8.19}$$

Energy loss to heat

The energy loss to heat is defined by the current passing through the resistance elements in the equivalent circuit, times the potential drop over these resistance elements. The current passing through the transmission line as function of position in the transmission line can be obtained using equation (8.7), as shown in equations (8.20) through (8.22).

$$\frac{de}{dz} + iR_V = 0 \tag{8.20}$$

$$i = -\frac{1}{R_V}\frac{de}{dz} \tag{8.21}$$

$$i = \frac{1}{R_V C_V}\frac{dq}{dt} \tag{8.22}$$

Therefore the energy loss to heat du/dt in $J\ cm^{-2}\ s^{-1}$ can be defined according to equation (8.23) with boundary conditions according to equations (8.24) and (8.25), which follow from equations (8.13) and (8.14).

$$\frac{du}{dt} = i^2 R_V \tag{8.23}$$

$$\frac{du}{dz}(z = l) = 0 \tag{8.24}$$

$$\frac{du}{dt}(z = 0) = i^2 R_{ext} \tag{8.25}$$

The total energy loss to heat P_T in $J\ cm^{-2}\ s^{-1}$ can be defined according to equation (8.26).

$$P_T = dU_T/dt = \int_0^l \frac{du}{dt}\, dz \tag{8.26}$$

By integrating equation (8.26) with respect to time, the total energy loss to heat U_T in $J\ cm^{-2}$ is obtained.

8.3.5 Implementation

To implement the model, the presented mass transport, charge transport and energy loss differential equations have to be solved together with their respective boundary conditions, while taking into account that conductivity changes with concentration. To solve these equations, a numerical discrete method is pursued.

Discretization

The discretization of plug flow is a flow through a series of CSTR's. By choosing the number of CSTR's (n_{CSTR}) in series, the behavior of the process can be controlled. When $n_{CSTR} \rightarrow \infty$, ideal plug flow behavior is obtained. For the developed mass transport model, already for $n_{CSTR} \geq 10$ CSTR model behavior was equal to plug flow behavior.

The mass balance for each CSTR is stated in equation (8.27).

$$\frac{dc_n}{dt} - n_{CSTR}\Phi\frac{c_{n,in} - c_n}{Al_s} + \frac{1}{l_s}\frac{dc_{n,A}}{dt} = 0 \tag{8.27}$$

In this equation, dc_n/dt is the change in concentration in CSTR n in $mol\ cm^{-3}\ s^{-1}$, n_{CSTR} is the amount of CSTR's used to model the mass transfer process, $c_{n,in}$ is the influent concentration of each CSTR, which is equal to the effluent concentration of the previous CSTR (c_{n-1} for $n > 1$). For the first CSTR in the model, $c_{1,in}$ is equal to c_{in}.

To model charge transport a separate transmission line model for each CSTR can be used, since modeling of charge transport is independent of position A in the CDI cell. Discretization of the transmission line model is described in section 8.A. For $n_{TLM} \geq 40$ model behavior was equal to continuous transmission line behavior.

Dead volume

Between outlet of the CDI unit and the conductivity meter some dead volume exists, as discussed in chapter 6. To incorporate this effect, one additional CSTR is included in the model after $n = n_{CSTR}$ as shown in equation (8.28).

$$\frac{dc_{dead}}{dt} = \Phi \frac{c_{in} - c_{dead}}{V_{dead}} \tag{8.28}$$

In this equation, c_{in} is the outgoing concentration of the CDI unit ($c(A = A_{cell})$), and V_{dead} in cm^3 is the dead volume of the CDI cell. Furthermore, response of the model in terms of concentration c is delayed by t_{dead} according to equation (8.29).

$$t_{dead} = \frac{V_{dead}}{\Phi} \tag{8.29}$$

The evolution of concentration in the dead volume c_{dead} in $mol\ cm^{-3}$ as function of time t in s can then be compared to experimental data.

8.4 Results and discussion

8.4.1 Used data

For all results the cell design and influent characteristics belonging to the NaCl experiments from section 7 were used. Table 8.1 summarizes the parameters used in the modeling. At these experimental conditions, flow is laminar (Reynolds number ≈ 1) and therefore plug flow behavior can be assumed.

Table 8.1: Parameters used for modeling of the CDI process

Parameter	Value	Obtained
Double-layer surface area S	364 $m^2\ g^{-1}$	Results chapter 5
Charge-transfer performance β	37.5	Results chapter 5
Contact resistance R_0	0.1 Ω	Estimate chapters 4 and 5
Membrane resistance R_m	65 $\Omega\ cm^{-2}$	Estimate chapter 6
Specific penetration depth $\lambda_{c,V}$	2.47 $cm\ g^{-1}\ cm^2$	Results chapter 5
Cell voltage E_{cell}	$1.2V$	Experiment
Effective spacer thickness l_s	0.0090 cm	Cell design
Cell area A_{cell}	133.76 cm^2	Cell design
Dead volume V_{dead}	20 cm^3	Cell design
Carbon weight per unit cell area $\rho_{c,A}$	0.0190 $g\ cm^{-2}$	Cell design
Transmission line model	Linear De Levie	Results chapter 2
Temperature T	295.8 K	Experimental condition
Deionization efficiency Λ	0.83	Results chapter 7
Concentration c_0	10 $\mu mol\ cm^{-3}$	Experimental condition
Flow rate Φ	1.16 $cm^3\ s^{-1}$	Experimental condition

For validating the model with experimental results, two representative experiments were taken, one with membranes (MCDI cell configuration) and one without (CDI

cell configuration). For both experiments the fourth cycle of the experiment was used to compare with the model, to ensure steady-state response. For the experiment with membranes cell voltage of 1.2 V was used, while for the membrane-less experiment a cell voltage of 0.9 V was used to reduce the effect of redox reactions, since these processes are not included in the model.

8.4.2 Time response transmission line model

To investigate TLM kinetics, only the charge transport in the electrode compartment was modeled based on the parameters shown in table 8.1. This means that R_{ext} is not included in the modeling, and the electrolyte concentration is assumed constant in time. This results in a constant capacity of $C_c = 0.356\ F\ cm^{-2}$ at 1.2 V cell voltage, and constant resistance of $R_c = 51.0\ \Omega\ cm^2$, and therefore a time constant τ of 18.2 s. Using this time constant, the time response of the TLM can be compared with the time response of a RC model, as used in chapters 6 and 7. This is shown in figure 8.4.

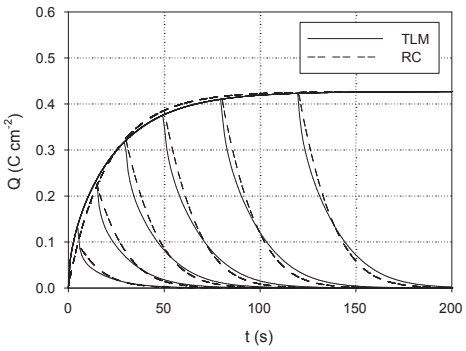

Figure 8.4: Kinetics transmission line model showing charge / discharge curves at various levels of charging, compared to kinetics of RC model

As shown in the figure, TLM charge / discharge kinetics are very similar to RC charge / discharge kinetics. TLM kinetics are initially faster until $Q \approx 0.3\ C\ cm^{-2}$, then RC kinetics are faster. The same trend is seen in the discharge, it takes more time to fully charge or discharge the TLM than it takes to fully charge or discharge the RC model.

To investigate this difference, figure 8.5 shows the distribution of charge q as function of position in the transmission line z [a] during charging between $t = 0\ s$ and

[a]For clarity, electrode thickness d_c is used as total transmission line length, actually the transmission line length is dependent on TLM shape and sample density (see sections 2.3.1 and 4.4.3)

$t = 5\ s$.

At $t = 0\ s$ the TLM is not charged and $q = 0\ Q\ cm^{-3}$ for all values of z. Since the interface between mass transport and charge transport is at $z = 0\ cm$, when charging the TLM ($t > 0$) the initial positions in the TLM are charged rapidly, but final positions ($z = 0.06\ cm$) in the TLM are charged slowly. When charging would continue after $t = 5$ all positions in the TLM would eventually be fully charged.

Figure 8.6 shows the response of discharging at $t = 5\ s$. At $t = 5\ s$ the same situation is obtained as shown in figure 8.5. Since the interface between mass transport and charge transport is at $z = 0\ cm$, when discharging the TLM ($t > 5$) the initial positions in the TLM are discharged rapidly, but final positions ($z = 0.06\ cm$) in the TLM are instead still being charged, denoted by the rightmost arrow. This is since at $t = 5$ charge is concentrated in the initial part of the TLM, therefore during discharge this charge goes two ways; toward the interface at $z = 0$ where it leaves the TLM, or toward the end of the pore at $z = 0.06\ cm$ where it is accumulated.

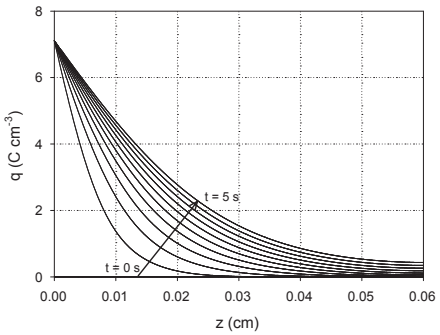

Figure 8.5: Distribution charge q in the transmission line during charge between $t = 0\ s$ and $t = 5\ s$. Arrow indicates change in distribution with time

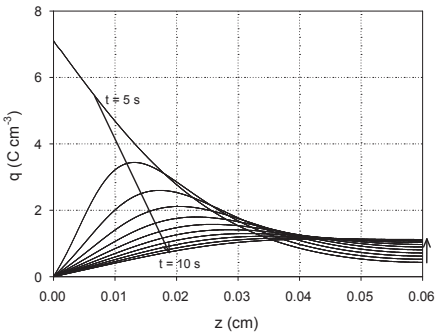

Figure 8.6: Distribution charge q in the transmission line during discharge between $t = 5\ s$ and $t = 10\ s$. Arrows indicate change in distribution with time

This effect makes the kinetics of the TLM initially fast since only the first section of the TLM are used. However, to fully charge or discharge the TLM takes a relatively long amount of time, since charging and discharging of the last section of the TLM is slow. This implies that to optimize deionization rate it can be useful not to fully charge or discharge the electrodes.

8.4.3 Validation

Concentration results

Figure 8.7 shows evolution of concentration c in $\mu mol\ cm^{-3}$ versus time t in s for a MCDI configuration with ion-exchange membranes. In this figure, the experimental data showed a decrease in concentration c closely after charging was initiated ($t = 0\ s$). When discharge was initiated ($t = 900\ s$) an increase in concentration c was observed. The experimental data and the modeled data (shown as "Model" in the graph) agree perfectly during the charge process. During discharge however, the modeled data deviate from experimental data, a more narrow discharge curve is predicted by the model. To obtain good correspondence with experimental data, the resistance during discharge had to be increased by $\approx 65\ \Omega\ cm^{-2}$. This is shown in figure 8.7 as "Corrected model". After correction, also the discharge curve agrees with experimental data. The extra resistance can be attributed to transport limitation from electrode compartment to spacer compartment. This is proved when modeling an experiment without membranes, in figure 8.8 the modeling of an experiment without membranes is shown. For input parameters of the model, the conditions as described in chapter 6 were used, additionally for the CDI configuration without ion-exchange membranes a cell voltage of $E_{cell} = 0.9\ V$ was used.

As shown in figure 8.8, during charging the model deviates from the experimental data, while during discharge a very good agreement of the model with the experimental data can be seen. As discussed in chapter 6, high pressure drops exist over the cell. This can result in electrolyte flowing through the electrode instead of through the spacer, inducing additional mixing. This effect can be modeled by including additional mixing in the spacer compartment during charge, limiting the rate of adsorption. This is incorporated in the model by increasing l_s in equation (8.27) by a factor 2.5, while keeping the resistance due to l_s in equation (8.16) equal. During discharge, the released ions will result in a very high local concentration in the electrodes, and therefore the ions are removed much faster from the cell than as they are being adsorbed.

Mixing is also most likely the reason why the MCDI cell configuration with ion-exchange membranes shows differing charge kinetics from discharge kinetics. During charging, ions are transported from spacer compartment toward electrode compartment. Since in the electrode compartment a flow exists, concentration polarization is not an issue due to mixing. However, during discharge the ions are transported from electrode compartment toward spacer compartment. Since in the electrode compartment no mixing takes place, concentration polarization can be an issue [5]. This will introduce an additional resistance.

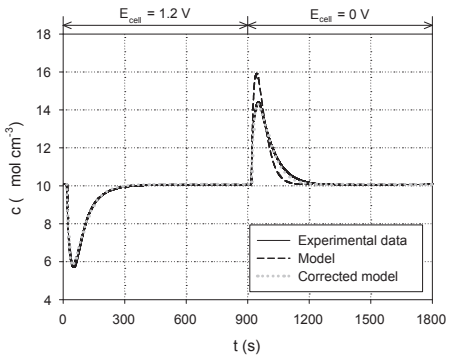

Figure 8.7: Concentration c versus time t for experimental data for MCDI configuration, the constructed model, and the corrected model with increased resistance during discharge. Secondary x-axis shows cell voltage E_{cell} at the specific time

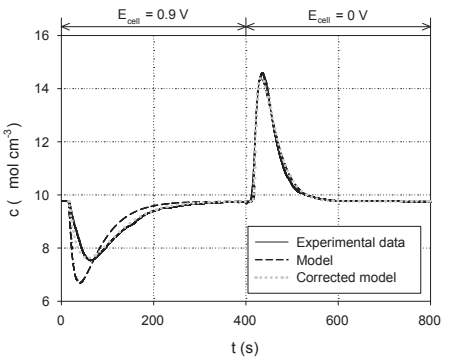

Figure 8.8: Concentration c versus time t for experimental data for CDI configuration, the constructed model and the corrected model. Secondary x-axis shows cell voltage E_{cell} at the specific time

More research on membrane characteristics in MCDI cell configurations is needed to confirm this finding.

Charge results

Figure 8.9 shows evolution of charge Q in C versus time t in s. In this figure, the experimental data shows during charging a fast increase of Q with time. At $t = 300\ s$ the MCDI unit is fully charged, the further linear increase of Q is attributed to redox reactions, as discussed in chapter 6. During discharge kinetics seem slower, at $t = 1200\ s$ the MCDI unit is still discharging. Both models do not fully reproduce the charge kinetics of Q due to the fact that redox reactions are not included in the models.

To further investigate the discharge step, figure 8.10 compares the discharge step of the experimental data with the corrected model. A RC model fit was applied on the discharge step of the experimental data, which is the method to obtain resistance and capacitance from experimental data as described in chapter 6.

As shown in figure 8.10, the corrected model underestimates the total capacitance; the end value for $Q_{discharge}$ is lower than the experimental data. The initial slope of the experimental data does coincide with the corrected model, so therefore resistance results should be more accurate. The RC fit shows good agreement with both model as well as with experimental data.

Results from the RC fit are the integral capacity C_{int} of $0.333 \pm 0.001 F\ cm^{-2}$,

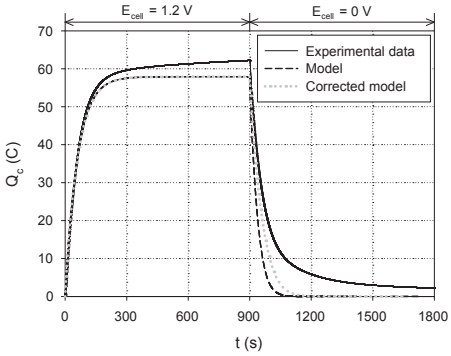

Figure 8.9: Charge Q versus time t for experimental data, the constructed model, and the corrected model with increased resistance during discharge. Secondary x-axis shows cell voltage E_{cell} at the specific time

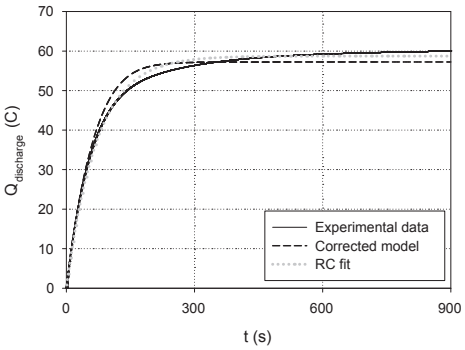

Figure 8.10: Absolute discharge $Q_{discharge}$ versus time t for experimental data and the corrected model, together with a RC model fit on the experimental data

and total resistance R of $213 \pm 1\ \Omega\ cm^{-2}$. C_{int} at the experimental conditions as shown in table 8.1 corresponds with a value for S of 340 $m^2\ g^{-1}$, which is close to the characterization value of 364 $m^2\ g^{-1}$. The resistance of the kinetics model R_{total} during discharge was maximum $254\ \Omega\ cm^{-2}$, and during charge was maximum $189\ \Omega\ cm^{-2}$. This agrees with the RC fit results, therefore the RC fit procedure as proposed in chapter 6 can be used to obtain accurate values for total resistance and total capacitance.

Energy results

Figure 8.11 shows evolution of the electric energy converted to heat U_T in J versus time t in s. Since U_T is directly coupled to the change in charge Q as shown in figure 8.9, the shape of the lines in figure 8.11 is equal to the shape of the lines in figure 8.9. The final value of Q is independent of resistance, both the model and the corrected model reach $U_{T,max} = 68\ J$ at $t = 1800\ s$. When dividing $U_{T,max}$ by Q_{max}, the amount of Joules per coulomb of charge are obtained, $U_{T,max}/Q_{max} = 1.2\ J/C$, which is equal to E_{cell}. This confirms that also for energy loss the cell can be regarded as a RC model, when charging a RC model with constant voltage and discharging at $0\ V$, energy loss per Coulomb is also equal to the voltage.

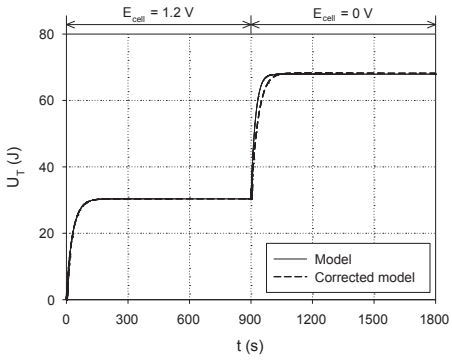

Figure 8.11: Electric energy converted to heat U_T versus time t for the constructed model, and the corrected model with increased resistance during discharge. Secondary x-axis shows cell voltage E_{cell} at the specific time

Effect dead volume

To investigate the effect of dead volume, the response of the cell configuration was modeled as described in table 8.1 for a dead volume $V_{dead} = 2\ cm^3$, and for the original value for V_{dead}, which is 10 times as high. Figure 8.12 shows evolution of concentration c in $\mu mol\ cm^{-3}$ versus time t in s for both models.

As shown in this figure, decreasing the dead volume by a factor 10 will result in more pronounced peaks in concentration, a lower minimum concentration is reached during charge, and a higher maximum concentration is reached during discharge. Furthermore, the peaks are shifted to an earlier point, since the concentration reaches the outlet earlier.

Due to the dead volume, the response of the cell configuration changes from a plug flow response to a CSTR response. This explains why in the work by Biesheuvel et. al. [1] the used CSTR model agrees reasonably well with measurements.

In practical CDI cell configurations it is important to reduce dead volume, to obtain a minimal effluent concentration during charge and to obtain maximal effluent concentration during discharge. In research CDI cell configurations it is important to reduce dead volume, since the actual cell response is of importance, not the response of the dead volume. This can be done by incorporating the conductivity meter in the actual cell.

Effect time response TLM on modeling

To investigate the effect of time time response TLM on modeling, the response of the cell as described in table 8.1 was modeled for the original model with linear TLM,

and for a simplified model where the TLM is treated as a simple RC element, as discussed in chapter 6. However, no difference in response was found, indicating that when using the experimental conditions as shown in table 8.1 TLM response has no effect on the total model. Only when the resistance of the electrodes R_c is sufficiently high as compared to total resistance R_{total} a difference could be seen. Figure 8.13 shows evolution of concentration c in $\mu mol\ cm^{-3}$ versus time t in s when $R_m = 0$ and $R_{c,new} = 10\,R_c$ for the original model with the linear TLM, and for a model where a simple RC element is used to model the TLM.

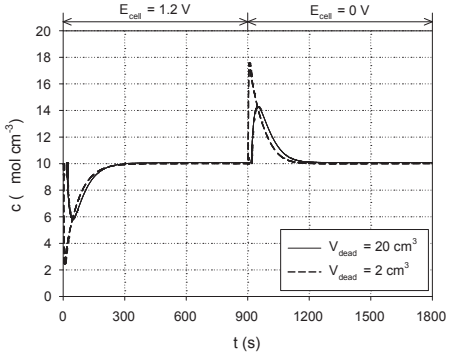

Figure 8.12: Concentration c versus time t for two configurations with different dead volumes V_{dead}. Secondary x-axis shows cell voltage E_{cell} at the specific time

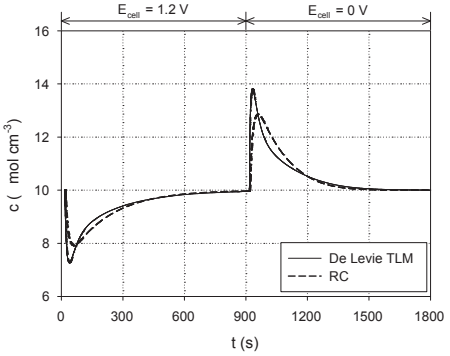

Figure 8.13: Concentration c versus time t when using the linear TLM, or when treating the TLM as a simple RC element. Secondary x-axis shows cell voltage E_{cell} at the specific time

As shown in this figure, the linear TLM very clearly shows the kinetics as discussed in section 8.4.2, during discharge initially a steep peak is shown, which at $t \approx 1000$ shows a distinct bend after which discharge is much slower. This is related to the diffusion of ions which are located far into the carbon material, and take a long time to diffuse out of the carbon material.

8.5 Conclusion

8.5.1 Time response transmission line model

The time response of the transmission line model shows that charge / discharge kinetics are very similar to charge / discharge kinetics of a simple RC model. However, to fully charge or discharge the TLM takes a relatively long amount of time, since charging and discharging of the last section of the TLM is slower than expected from the RC model. This has practical implications, since incomplete discharging will result

in a loss of capacity after many charge / discharge cycles.

When investigating the impact of the transmission line model on the final model, it was found that when dealing with a high electrode resistance the effect of the transmission line model in the results is significant. Otherwise a simple RC model suffices. It is likely that the impact of the transmission line model will become higher when deionizing mixtures of salts. In this case each ion can have a different diffusion profile in the carbon electrode, which cannot be modeled with a simple RC model.

8.5.2 Modeling of (M)CDI cell configurations

By using the theoretical relations found in chapters 3 through 5, a very close fit with experimental data on concentration versus time was obtained. For a cell configuration including membranes, during discharge an extra resistance is present, which is equal to the value for R_m which can be attributed to concentration polarization. For a cell configuration without membranes, during charging a deviation between model and measurements exist that can be attributed to increased volume of the spacer. More research is needed on the relation between cell design and CDI performance to confirm this finding.

Regarding the charge results, a simple RC model can indeed be used to fit the discharge curve of a CDI experiment. Results obtained using the RC fit were close to the theoretical values.

Regarding the energy results, when using constant voltage to charge a CDI cell, and short-circuiting the cell to discharge, the amount of energy lost to heat per coulomb charge is equal to the cell voltage.

Regarding dead volume, by theoretical modeling it was found that dead volume has to be minimized in practical CDI cell configurations to obtain low concentration effluent, and high concentration brine. In research CDI cell configurations the dead volume has to be minimized to measure the actual cell response, and not the effect of dead volume.

8.A Appendix 1: Discretization transmission line model

8.A.1 Discretization

The TLM is discretized with n_{TLM} amount of elements, where each element describes Δz cm of TLM, according to equation (8.30).

$$\Delta z = \frac{l}{n_{TLM}} \tag{8.30}$$

In figure 8.14 a discretized section of the TLM is shown.

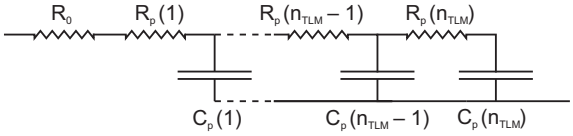

Figure 8.14: Discretized section of the transmission line model

In this figure, n_{TLM} is the total amount of elements in the transmission line. $R_p(n)$ are the discretized resistance elements in the TLM in Ω cm^2, and $C_p(n)$ are the discretized integral capacitance elements of the TLM in F cm^{-2}. Analogy can be made with the derivation of the power law TLM, as discussed in section 2.A.

When dealing with a power-law TLM, the distribution $R_p(n)$ can be constructed from discretizing equation (2.22), as shown in equations (8.31) and (8.32).

$$R_p(z) = n_c K \left(\frac{z}{l}\right)^{n_c-1} \tag{8.31}$$

$$R_p(\Delta z) = K \left(\frac{\Delta z}{l}\right)^{n_c} \tag{8.32}$$

In these equations, K is related to equivalent resistance R_c as derived in section 2.A, and shown in equation (8.33).

$$K = \frac{(n_c+1)(n_c+2)}{2} R_c \tag{8.33}$$

Using equation (8.32) the resistance $R_p(n)$ can be defined for element 1 through element n_{TLM} of the transmission line, according to equation (8.34) through equation (8.37).

$$R_p(1) = K\left(\frac{1}{n_{TLM}}\right)^{n_c} \tag{8.34}$$

$$R_p(2) = K\left(\frac{2}{n_{TLM}}\right)^{n_c} - R_p(1) \tag{8.35}$$

$$R_p(n) = K\left(\frac{n}{n_{TLM}}\right)^{n_c} - R_p(n-1) \tag{8.36}$$

$$R_p(n_{TLM}) = K\,(1)^{n_c} - R_p(n_{TLM}-1) \tag{8.37}$$

When dealing with a linear TLM ($n_c = 1$), each element of R_p is equal, and R_p can be directly related to R_c, the carbon resistance in $\Omega\ cm^2$ according to equation (8.38).

$$R_p = 3\,R_c \tag{8.38}$$

8.A.2 Charge balance

To obtain the charge balance over the TLM, a similar approach is used as in section 8.3.4. The potential drop $E_R(n)$ in V is defined as the potential drop over each resistance element $R_p(n)$ in the transmission line. As can be seen from figure 8.14, each transmission line element $R_p(n) - C_p(n)$ is parallel to $C_p(n-1)$, and therefore the potential drop is equal according to equation (8.39).

$$E_R(n) = E_C(n-1) - E_C(n) \tag{8.39}$$

In case $n = 1$, equation (8.39) becomes equation (8.40) resulting from the boundary conditions as depicted in equations (8.13) and (8.14).

$$E_R(1) = E_{cell} - E_C(1) \tag{8.40}$$

When considering that all elements of $C_p(n)$ are equal, equations (8.30) and (8.49) can be used to obtain the potential drop over each integral capacitance element E_C according to equation (8.41).

$$E_C(n) = e(\frac{q(n)}{\Delta z}, S\rho_{c,A}) \tag{8.41}$$

In this equation, e is the double-layer potential as function of double-layer charge $q(n)$ and specific double-layer area $S\rho_{c,A}$ in m^2 double-layer area per cm^2 cell area, as discussed in section 8.B.

Now that an expression for the potential drop over the resistors is obtained, an expression for the change in charge $dq(n)/dt$ for each integral capacitor $C_p(n)$ can be obtained, according to equation (8.42)

$$\frac{dq(n)}{dt} = \frac{E_R(n)}{R_p(n)} - \frac{E_R(n+1)}{R_p(n+1)} \tag{8.42}$$

In case $n = n_{TLM}$, equation (8.42) becomes (8.43), when $n = 1$ equation (8.42) becomes (8.44), resulting from the boundary conditions as depicted in equations (8.13) and (8.14).

$$\frac{dq(n_{TLM})}{dt} = \frac{E_R(n_{TLM})}{R_p(n_{TLM})} \tag{8.43}$$

$$\frac{dq(1)}{dt} = \frac{E_R(1)}{R_{ext} + R_p(n)} - \frac{E_R(2)}{R_p(2)} \tag{8.44}$$

The total change in charge dQ/dt is the total current that flows through the first resistance element R_p. This is shown in equation (8.45).

$$\frac{dQ}{dt} = \frac{E_R(1)}{R_{ext} + R_p(1)} \tag{8.45}$$

To obtain the rate of electric energy converted into heat $du_T(n)/dt$ in $J\ s^{-1}$, the square of $E_R(n)$ is divided by R_n, as shown in equation (8.46)

$$\frac{du_T(n)}{dt} = \frac{(E_R(n))^2}{R_n} \tag{8.46}$$

In the special case that $n = 1$, equation (8.46) becomes equation (8.47) resulting from the boundary conditions as depicted in equations (8.13) and (8.14).

$$\frac{du_T(1)}{dt} = \frac{(E_R(1))^2}{R_{ext} + R_1} \tag{8.47}$$

The total rate of electric energy converted into heat dU_t/dt is the sum of all elements of $du_T(n)/dt$, as shown in equation (8.48)

$$\frac{dU_T}{dt} = \sum_{n=1}^{n_{TLM}} \frac{du_T(n)}{dt} \tag{8.48}$$

8.B Appendix 2: Calculation double-layer potential based on double-layer charge

For the calculation of the time response of the TLM, the double-layer potential E_C in V when a differential capacitance C_c is charged with q coulombs of charge is needed. For this purpose, the relations found in chapter 3 section 3.3.1 can be used.

First of all equation (3.12) is used to obtain the charge on the double-layer according to equation (8.49).

$$Q_{dl} = \frac{q}{0.5 \cdot 10^4 \, S \, \rho_{c,A}} \tag{8.49}$$

In this equation, Q_{dl} is the double-layer charge, the factor 0.5 is present since two electrodes are present in a CDI configuration and therefore Q_{dl} is divided over two double-layers. S is the amount of double-layer present per weight electrode in $m^2 \ g^{-1}$, and $\rho_{c,A}$ is the carbon loading, the weight of carbon per unit surface cell area in $g \ cm^{-2}$.

The charge in the double-layer Q_{dl} is equal to the charge in the separate layers, and the potential drop over the double-layer is equal to the sum of potential drops over the separate layers, as is shown in equations (8.50) and (8.51).

$$Q_{dl} = Q_h = Q_d \tag{8.50}$$

$$E_{dl} = E_h + E_d \tag{8.51}$$

Equations (8.52) and (8.53) define the charges on the separate double-layers.

$$Q_h = E_h C_h \tag{8.52}$$

$$Q_d = \sinh\left(\frac{zFE_d}{2\,RT}\right)\frac{2\,\epsilon_d\epsilon_0 RT}{\lambda z F} \tag{8.53}$$

Equations (8.52) and (8.53) can be combined with equation (8.50) to obtain double-layer potential as function of double-layer charge, as shown in equations (8.54) and (8.55).

$$E_d = \operatorname{arcsinh}\left(\frac{Q_{dl}\lambda z F}{2\,\epsilon_d\epsilon_0 RT}\right)\frac{2\,RT}{zF} \tag{8.54}$$

$$E_h = \frac{Q_{dl}}{C_h} \tag{8.55}$$

The total potential drop over the two double-layers E_C is twice the sum of E_d and E_h, as shown in equation (8.56).

$$E_C = 2\ (E_d + E_h) \tag{8.56}$$

When following the procedure as presented in this section, E_C can be calculated based on the charge q on the capacitance element, the weight of carbon per unit surface area $\rho_{c,A}$ and the specific double-layer area S.

Bibliography

[1] P. M. Biesheuvel, B. van Limpt, and A. van der Wal. Dynamic adsorption/desorption process model for capacitive deionization. *The Journal of Physical Chemistry C*, 113(14):5636–5640, 2009.

[2] R.B. Bird, W.E. Stewart, and E.N. Lightfoot. *Transport Phenomena*. Wiley, New York, 2nd edition, 2002.

[3] A. M. Johnson and J. Newman. Desalting by means of porous carbon electrodes. *Journal of the Electrochemical Society*, 118(3):510–&, 1971.

[4] R. de Levie. On porous electrodes in electrolyte solutions: IV. *Electrochimica Acta*, 9(9):1231, 1964.

[5] P. Długołęcki, P. Ogonowski, S. Metz, M. Saakes, K. Nymeijer, and M. Wessling. On the resistances of membrane, diffusion boundary layer and double layer in ion exchange membrane transport. *Journal of Membrane Science*, -(-):–, 2009.

Chapter 9

General discussion and conclusion

Performance relations in Capacitive Deionization systems can be obtained by electrochemical characterization. These performance relations can be used to predict deionization performance of a certain CDI configuration. To obtain this prediction of performance, five distinct steps need to be followed:

1. Obtain the electric properties of a CDI configuration (chapters 2 and 6)
2. Link the electric properties to physical processes, and thus performance (chapters 3, 4 and 5)
3. Determine the effect of electrode properties on performance relations (chapter 5)
4. Relate performance in terms of charge to performance in terms of ion adsorption (chapters 6 and 7)
5. Integrate all acquired performance relations in a predictive model (chapter 8)

These steps will be further discussed in the following sections, followed by a general conclusion.

9.1 Electrochemical characteristics of a CDI configuration

Electrochemical impedance spectrometry (EIS) is an extensive method to characterize CDI electrode configurations, as shown in chapter 2. This characterization results in several important electrode characteristics, which are:

- Electrode capacitance C_c; related to the amount of ions that can be stored onto the electrodes
- Electrode resistance R_c; the resistance encountered when ions migrate into the electrode
- System resistance R_s; the electrolyte resistance between the two electrodes plus the contact resistance from CDI cell to potentiostat

- Charge-transfer resistance R_{ct}; related to the transfer of electrons at the interface between current collector and carbon electrode

All these characteristics are of electrochemical nature, meaning that they describe the transport and storage of charge in a CDI electrode configuration. The electrode capacitance and electrode resistance are distributed over the length of the pores in the porous carbon electrode. Therefore resistance and capacitance of the carbon electrode are related by dynamic processes that can be described by a transmission line model (TLM). For carbon powder and carbon aerogel electrodes this distribution can be mimicked by models present in literature. These models describe the distribution of electrode capacitance as function of electrode resistance. For carbon fiber electrodes a custom model is needed, due to a non-standard distribution of resistance and capacitance in the carbon material. This distribution (the power law TLM) is according to a power law relationship, where capacitance is concentrated in the beginning of the distribution. This power law TLM has an unique impedance response:

- At high frequencies the power law TLM resembles the TLM of carbon aerogel electrodes, which is a constant phase angle transmission line model (CPA TLM). It is widely regarded that the CPA TLM is due to surface roughness of the electrode surface.

- The high frequency response of the power law TLM does not correspond with an arbitrary pore geometry with a homogeneous distribution of resistance and capacitance, since this would result in an transmission line angle of 45 degrees at high frequencies.

- At low frequencies the transmission line model resembles an ideal capacitor, which corresponds with an ideally flat surface.

This impedance response indicates that the power law TLM is caused by the unique properties of activated carbon fibers:

- Fibers are round and very constant of dimensions, therefore when ions penetrate into the fibers the accessible surface area declines uniformly. Proof for the uniform penetration of ions into carbon material was found in chapter 5, where a constant specific ion penetration depth was found.

- It is known that the pore structure of carbon fibers can be very complex and likely consisting of spiral-like structures [1], which further complicates the transmission line behavior.

- When grinding the carbon fibers and making an electrode with polyvinylidene fluoride (PVDF) as a matrix, the distribution of resistance and capacitance in the TLM changes. Resistance becomes concentrated in the beginning of the distribution, meaning that capacitance can only be accessed slowly. From SEM pictures it was found that PVDF covers a significant portion of the separate carbon particles, which might have caused this effect.

When only total resistance and total capacitance are of importance, cyclic chronopotentiometry (chapter 2) and amperometry (chapter 6) are a good alternative method to characterize CDI electrode configurations. Both methods can be easily set-up and interpreted, and give equal results as EIS results, as proven in chapters 2 and 8, however at a lower accuracy. When combining amperometry with conductivity measurements as done in chapters 6 and 7, also the relation between charge capacity and ionic capacity can be obtained, which cannot be obtained with EIS.

9.2 Link between electrochemical characteristics and physical processes

Electrode capacitance C_c is represented by the double-layer capacitance of the electrode according to the Gouy-Chapman-Stern theory, as shown in chapter 3. This theory accurately describes the capacitance relations for carbon fiber materials, at various temperatures, concentrations and cell voltages. When applying the theory to carbon powder materials, the relation shows a good agreement. For carbon aerogel electrode materials, results show a very high dependence of capacity on cell voltage, which is not predicted by the Gouy-Chapman-Stern theory. Therefore the Gouy-Chapman-Stern theory cannot be used to describe the capacity relations for carbon aerogel electrode materials.

The link between double-layer capacitance and electrode capacitance is defined by the electrochemical surface area S, which is the amount of double-layer area per electrode weight. This parameter can be used to screen for new high-capacity electrodes, a higher electrochemical surface area means more capacitance can be generated with an equal electrode weight.

Electrode resistance R_c is represented by the electrolyte resistance present in the electrode, plus to a smaller extent the electrical resistance between the various carbon particles, as shown in chapters 4 and 5. The electrolyte resistance is determined by migration of ions into the separate carbon particles, and not by the migration of ions toward the separate carbon particles. Furthermore, the electrical resistance of the carbon electrode only becomes limiting at very high electrolyte conductivities,

meaning that addition of graphite to the electrode to decrease the electrical resistance does not improve the overall electrode resistance.

The link between the electrolyte resistance and the electrode resistance is defined by the specific penetration depth λ_c, which is the distance ions have to migrate into a certain mass of carbon per area electrode surface. This parameter can be used to screen for high-performance electrode configurations. A lower specific penetration depth means capacity can be accessed faster with an equal electrode weight per unit cell area.

System resistance R_s is represented by the electrolyte resistance which is present in the spacer plus a certain constant contact resistance, as shown in chapter 4. This contact resistance is not only the contact resistance between power supply and current collector. Chapter 5 shows that when including a non-activated felt between current collector and carbon electrode, the contact resistance can be significantly reduced. This is since the current collector is a mesh, which does not fully connect with the electrode material. When introducing the non-activated felt, current first is transferred from current collector to non-activated felt, which is a good conductor. This non-activated felt is in full contact with the carbon electrode, reducing contact resistance.

The link between electrolyte resistance and the system resistance is defined by the effective spacer thickness and a contact resistance. The effective spacer thickness can be used to screen for low resistance spacers, a low effective spacer thickness means that capacitance can be accessed faster. The contact resistance can be used to identify possible faulty contacts in the system.

Charge-transfer resistance R_{ct} is represented by a charge-transfer process between current collector and carbon electrode, as shown in chapters 4 and 5. This charge-transfer process is influenced by temperature and electrolyte concentration, and follows an Arrhenius relation. The charge-transfer resistance is only influenced by the electrode properties, not by the current collector properties. Furthermore, it is confirmed that the charge-transfer process is an interface process, since it is not influenced by density or thickness of the used electrode.

The link between electrolyte concentration, electrolyte temperature and charge-transfer resistance is defined by the charge-transfer performance β. This parameter can be used to screen electrode configurations with a low charge-transfer resistance. A higher charge-transfer performance means capacity can be accessed faster.

9.3 Effect electrode properties on performance relations

Three performance parameters for electrode materials were defined in chapters 4 and 5, the electrochemical surface area S, the specific penetration depth λ_c and the charge-transfer performance β. The relation between electrode materials and these performance parameters was investigated in chapter 5.

The electrochemical surface area S is determined by the area of relatively large micropores and relatively small mesopores of a certain carbon. The larger these area's are, the more electrochemical surface area.

The specific penetration depth λ_c is equal for all investigated carbons. This means that migration of ions into carbon pores is not influenced by the pore structure, which is different for all carbons.

The charge-transfer performance β is determined by two factors. The first factor is the structure of the interface between carbon electrode and current collector. When this interface is relatively smooth, as in a carbon cloth, charge transfer performance is high. When this interface is rough and hindered by inert material, as in the ground carbon fiber in PVDF matrix, charge transfer performance is low. The second factor which determines charge-transfer performance β is the BET surface area of the carbon material. A larger BET surface area results in a higher charge-transfer performance.

Most likely the charge-transfer resistance is caused by electron hopping on the interface between current collector and activated carbon, this would mean that a smooth interface will reduce the resistance while a rough interface increases the resistance. This observation is similar to that found in literature [2], by creating a continuous interface between current collector and carbon electrode charge transfer resistance can be greatly decreased. Furthermore, a higher BET surface area also means a higher amount of surface groups, meaning that electrons can more easily "hop" from the current collector to the carbon electrode, since local charge differences can be buffered by the surface groups [3]. This might indicate that the concentration dependency of the charge-transfer resistance is due to a change in activity of functional groups on the surface by a change in electrolyte concentration.

9.4 Relation performance in terms of charge to performance in terms of ion adsorption

The performance parameters defined in chapters 2 through 5 relate operational conditions and electrode configuration to a total electrical capacitance C_c and a total

resistance R_{total} (equal to the sum of all resistance characteristics). Ideally, total resistance and total electrical capacitance can be directly transformed to ion adsorption using Faraday's constant, which relates the buildup of charge on the electrode to the amount of ions that are being adsorbed.

As demonstrated in chapter 6, in practice this does not hold. Two efficiency parameters exist between the electrochemical characteristics and deionization performance. These are the coulombic efficiency CE and the deionization efficiency Λ. The coulombic efficiency is the fraction of electrons lost due to parasitic reactions during the charging process, and the deionization efficiency is the equivalent amount of ions removed per equivalent amount of stored charge.

Coulombic efficiency is less than one since redox reactions can occur, especially at higher cell voltages. This is normally only to a small extent ($<$ 10%), and can be further reduced by employing ion-exchange membranes which block redox shuttles. Deionization efficiency is also below one, since charge on the surface of an electrode can also occur due to co-ion expulsion instead of counter-ion adsorption. This effect reduces with increasing cell voltage, since counter-ion adsorption increases with increasing cell voltage, while co-ion expulsion remains relatively constant. When employing ion-exchange membranes co-ion expulsion can be reduced, resulting in a constant deionization efficiency independent of cell voltage.

It was investigated if the performance relations also hold when deionizing other salts than sodium chloride. This does seem to be the case, performance of other salts show remarkably close performance and efficiency to sodium chloride. This means that in general the proposed double-layer model in chapter 3 can be used to predict deionization capacity of any common salt, and that the resistance relations found in chapter 4 can be used to predict deionization rate of any common salt.

Further research is needed to investigate why the deionization efficiency never becomes larger than about 80%. Perhaps part of the applied charge is stored as pseudo-capacitance due to surface functional groups, or dead pockets exist in the deionization unit which do not participate in the overall deionization process. The effect of surface functional groups can be evaluated by investigating dependence of deionization efficiency on the type of carbon in the electrode. Dead pocket effects can be evaluated by investigating dependence of deionization efficiency on cell geometry.

9.5 Integration of all acquired performance relations in a predictive model

The integration of all acquired performance relations in a predictive model is possible by coupling a plug flow model to a transmission line model, while dead volume of the

setup is also accounted for by incorporating a CSTR model. The plug flow model describes mass transport of ions between two parallel electrodes, and the transmission line model describes charge transport into the electrodes. The input of the model are characterization results of the used electrode (double-layer surface area, charge-transfer performance and specific penetration depth), the cell design, influent characteristics, and the mode of CDI operation. The output of the model is the predicted outlet concentration and the predicted energy use.

As demonstrated in chapter 8, the predictive model shows a good agreement with experimental results. The difference between the model predictions and the actual measurements can be related to processes and phenomena not included in the model:

- For a MCDI cell configuration (with membranes), during discharge an extra resistance has to be included. This extra resistance is attributed to concentration polarization on the surface of the membranes. Further research is needed in understanding the effect of concentration polarization, and in general membrane characteristics, to deionization performance.

- For a CDI cell configuration (without membranes), during charging a deviation between model and measurements exists that is attributed to flow of electrolyte through the electrode. By including additional mixing this effect can be mimicked in the modeling. The mixing effect reduces deionization performance, and is one additional reason to incorporate ion-exchange membranes in CDI design which prevent flow of electrolyte through the electrode.

- The dead volume of the setup has a significant impact on the deionization behavior, when increasing the dead volume a CSTR behavior was found instead of the expected plug flow behavior. It is critical to minimize the dead volume to obtain maximum removal of salts.

- The inclusion of transmission line behavior of the electrode has a limited impact on the deionization behavior; a simple model consisting of a resistor in series with a capacitor (RC model) as proposed in chapter 6 also suffices. However, when dealing with a high electrode resistance, incomplete charging or discharging, the effect of the transmission line model on deionization behavior is significant. It is likely that the impact of the transmission line model becomes higher when deionizing mixtures of salts. In this case each ion has a different diffusion profile in the carbon electrode, which cannot be modeled with a simple RC model.

9.6 General conclusion

The developed approach of linking electrochemical characteristics to deionization performance results in a method that can be used to characterize any element of a (M)CDI system. This element can be the current collector, electrode, spacer, but also the design of the stack. The characterization itself can be relatively fast, only a few experiments are needed to obtain a broad range of performance parameters. The obtained performance parameters are in turn independent of operational parameters such as electrolyte composition, temperature, and cell voltage. These performance parameters can in turn be used for various purposes:

- **Material selection** Materials can be screened for highest performance.
- **Performance prediction** The developed predictive model can be used to predict deionization performance for any operational condition.
- **Bottleneck identification** By comparing the model prediction to actual results, bottlenecks in the operation of the (M)CDI system can be identified and resolved.
- **System design** The obtained performance relations can be used to propose a certain system design for a certain deionization application, since the required deionization rate and deionization capacity can be linked to required stack design. Furthermore, the predictive deionization model can be used in reverse; by using the deionization criteria as an input the required system design to meet these criteria can be obtained. This can be done for example by function minimization.

The key to the used approach was considering a (M)CDI electrode configuration equivalent to a supercapacitor, and therefore describing the kinetics of ion adsorption in terms of charge instead of in terms of ions. In this way, also important differences between supercapacitors and (M)CDI become apparent. These are the high impact of charge-transfer resistance to total resistance and the lack of effect of pore structure on the deionization rate. Both effects are caused by the low electrolyte conductivity used in (M)CDI applications.

Bibliography

[1] K. Kinoshita. *Carbon, Electrochemical and physicochemical properties.* Wiley Interscience, New York, 1st edition, 1987.

[2] C. Portet, P. L. Taberna, P. Simon, and C. Laberty-Robert. Modification of Al current collector surface by sol-gel deposit for carbon-carbon supercapacitor applications. *Electrochimica Acta*, 49(6):905–912, 2004.

[3] Y. R. Nian and H. S. Teng. Influence of surface oxides on the impedance behavior of carbon based electrochemical capacitors. *Journal of Electroanalytical Chemistry*, 540:119–127, 2003.

Summary

Capacitive Deionization (CDI) is a deionization technology based on the temporary storage of ions on an electrically charged surface. In **chapter 1** the history of CDI is discussed, as well as the advantages of CDI over existing deionization techniques such as electrodialysis and reverse osmosis. The advantages of CDI are most apparent for deionization of brackish water, mainly because for this application CDI shows the lowest energy use. Other advantages of CDI are a low susceptibility for scaling, and high water recovery.

To further determine the applicability of CDI, the performance relations of the deionization process have to be better understood. Therefore, the objective of this thesis is to relate the performance of a CDI unit to the design of the unit and the specifications of the influent stream (the electrolyte). This relationship can be used to define performance parameters for each of the elements in the CDI unit. These performance parameters can in turn be used to optimize the CDI unit for a specific application.

The approach to obtain performance relations is by focusing on charge transport, and linking this charge transport to deionization. By focusing on charge transport, a CDI system can be considered as a supercapacitor. A supercapacitor is a device that stores electrical charge and energy by adsorption of ions on a electrically charged surface. Since performance relations for supercapacitors are well known, these can be used as a starting point to understand the performance relations for CDI.

Before performance relations can be obtained, first a method is needed to characterize the CDI system. In **chapter 2** electrochemical methods used for supercapacitor characterization were reviewed for application to CDI. Two electrochemical characterization methods were selected, electrochemical impedance spectroscopy (EIS) and cyclic chronopotentiometry. These methods were applied to CDI electrode configurations comprising of two electrodes clamped between two current collectors and separated by a porous spacer. Three different electrode materials were tested, electrodes made from carbon powders, carbon fibers and carbon aerogel.

From the characterization it can be concluded that EIS is best suited for characterization of CDI systems. Characteristics that can be obtained are capacitance and resistance distribution in the carbon electrodes, charge transfer resistance between carbon electrode and current collector, and the system resistance comprising the contact resistances and the spacer resistance. These electrochemical characteristics can be directly related to deionization performance, capacitance relates to the amount of ions that can be adsorbed, and resistance relates to the rate at which these ions are

adsorbed.

Dynamics of transport and adsorption of ions in the porous carbon electrodes is determined by the distribution of capacity and resistance in the carbon electrode. For electrodes made out of carbon powder this distribution is homogeneous, while for electrodes made out of carbon aerogel it follows a constant phase angle model. For electrodes made out of carbon fiber, a new model had to be developed to describe the transport and adsorption dynamics. This new model is based on a power law distribution of resistance over capacitance in the electrode, and was successfully applied to model the ion transport in carbon fiber electrodes. The results of the EIS characterization could be verified by using cyclic chronopotentiometry, which gave equal results for total capacitance and total resistance of the CDI system.

The obtained electrochemical characteristics are only valid for the conditions at which the experiments are performed. To obtain independent performance relations, in chapters 3 and 4 the characterization method was used to determine the relation between the electrochemical characteristics and operational parameters. The operational parameters investigated were the temperature and concentration of the electrolyte, and the applied voltage. Using this relation, performance parameters can be defined that are independent of these operational parameters.

In **chapter 3** the relation between electrode capacitance and the operational parameters was investigated. The theoretical relation between electrode capacitance and operational parameters is defined by a double-layer model, which describes the accumulation of charge on surfaces. The Gouy-Chapman-Stern double-layer model has been chosen as the most appropriate model to describe this relation; this model is complex enough to account for all variations in operational parameters, while it is simple enough to only allow for two unknown model parameters. These two unknown model parameters are the Helmholtz layer capacitance, which describes the double-layer capacitance close to the surface, and the temperature dependency of the Helmholtz layer capacitance. By relating the model to the experimental data, the double-layer area per weight of carbon electrode for the used carbon could be obtained. This double-layer area is an independent performance parameter for the electrical capacity of the carbon electrodes. It was found that the double-layer model is able to accurately describe the capacity of the CDI electrodes. Furthermore, the obtained value for the Helmholtz layer capacitance was found to be similar to values found in literature, and the temperature dependence of this capacitance was found to be similar to the temperature dependence of the diffuse double-layer capacitance.

In **chapter 4** the relation between resistance and operational parameters was investigated. These resistances are system resistance, charge-transfer resistance and electrode resistance.

System resistance is the resistance of the porous spacer plus any possible contact resistances between power supply and current collectors. The resistance of the porous spacer is linearly related to absolute electrolyte resistivity, and results in the definition of a performance parameter which is equal to the effective thickness of the porous spacer. The effective spacer thickness was found to be larger than the actual spacer thickness. The contact resistance can be obtained by extrapolation to an effective thickness of zero, this resistance is equal to the measured contact resistance

Electrode resistance is the resistance encountered when ions penetrate into the porous electrode. It is proportionally related to the absolute electrolyte resistivity. This was confirmed by the experiments and resulted in a performance parameter which is equal to the penetration depth of ions into the carbon electrode. This penetration depth is in the same order as the thickness of the electrode.

Charge-transfer resistance is the resistance encountered when electrons are transferred from the current collector to the carbon electrode. It is unsure what the theoretical basis is for this resistance, the consensus is that it is a charge-transfer process, and therefore should follow an Arrhenius-like temperature dependency. This was confirmed by the experiments. However, the exact process for the charge-transfer could not be determined. Therefore an empirical approach was used to describe the relation between operational parameters and the charge-transfer resistance, which resulted in an empirical performance parameter which relates to the rate of charge-transfer on the interface between current collector and carbon electrode.

Chapters 3 and 4 form a framework that can be used to test different electrodes, spacers, current collectors and system designs, since each obtained performance parameter relates to one of these elements. The performance parameter for electrodes is further investigated in chapter 5, since the electrodes are most crucial in determining the performance of a CDI system.

In **chapter 5** the effect of electrode composition on electrode performance was determined. This was done by investigating different types of electrode materials, carbon fibers and carbon powder. A wide range of materials from different manufacturers with different surface characteristics were selected. Of each of the carbon materials, surface area measurements were performed to obtain surface characteristics. A novel production process was used to produce electrodes from carbon powders, where the carbon powder was mixed with a polyvinylidenefluoride(PVDF) solution in n-methylpyrrolidone (NMP). This mixture was cast on a glass plate, where the

NMP solvent was phase exchanged with water. This resulted in electrodes with a very consistent composition.

All electrodes were tested using the procedure developed in chapter 2, and performance parameters were obtained using the framework developed in chapters 3 and 4. From the relation between carbon surface characteristics and specific double-layer area, it can be concluded that most of the ions are contained in micropores and small mesopores. Charge transfer on the interface between current collector and activated carbon is proportionally related to the specific pore area of the activated carbon; a higher specific pore area will therefore enhance charge transfer. Resistance of the carbon electrode was found to be limited by migration of ions into the separate carbon particles, and to be determined by the weight of carbon per unit area. This resulted in the definition of the specific penetration depth of ions into the carbon material, which was found to be equal for all investigated carbons.

Chapters 2 through 5 relate performance to accumulation of charge only. In **chapter 6** the relation between performance in terms of charge (electrochemical performance) and performance in terms of ions (deionization performance) was investigated.

The theoretical relation between charge accumulation and ion removal is defined in the constant of Faraday, one mole of charge is needed to adsorb one mole of a monovalent binary salt. Two processes can disrupt this relationship. The first process is the loss of charge due to electrochemical reactions on the surface of the electrode. This process is defined as the Coulombic efficiency, which is the fraction of applied electrons that are eventually stored on the electrode. The second process is the loss of ion removal when during charging of the electrodes co-ions are expelled from the electrode, at the cost of the adsorption of counter-ions. This process is defined as the deionization efficiency, The imbalance between stored charge and removed ions is defined in the deionization efficiency, which is the fraction of stored charge that is used to remove ions from the electrolyte.

To investigate these two efficiency parameters, two different CDI configurations were investigated, a “standard” CDI configuration comprising carbon electrodes separated by an electrically insulating spacer, and a configuration where between the spacer and the electrodes ion-exchange membranes are placed. This configuration is called MCDI, for membrane capacitive deionization.

Experiments showed that electrochemical reactions on the surface of the electrode do occur to a small extent, especially at applied voltages higher than 1.2 V. At higher applied voltages up to 10 % of the applied current is used for these unwanted reactions, resulting in a Coulombic efficiency of only 90 %. These side reactions can be reduced by employing ion-exchange membranes, which resulted in a constant Coulombic effi-

ciency of about 95 %, also at applied voltages higher than 1.2 V. Experiments also showed that during charging of the electrodes co-ions are expelled from the electrode; at low applied voltages only 40 % of the stored charge is used to remove ions from the electrolyte. When using ion-exchange membranes the deionization efficiency becomes constant at 75 % for all applied voltages.

The efficiency advantages of MCDI resulted in an increase of the deionization rate by 25 % as compared to a CDI configuration. Furthermore, the MCDI configuration yields a factor 10 higher deionization rate, a 36 % higher adsorption capacity and reduced redox reactions as compared to state-of-the-art carbon aerogel electrode systems as reported in literature.

The final investigated performance relation is the effect of the ionic species comprising the electrolyte. This is investigated in **chapter 7**, where deionization performance was obtained with a broad range of electrolytes. These performances were compared to the deionization performance with a sodium chloride electrolyte. When taking into account the valence and the specific conductivity of the ionic species comprising the electrolyte, most electrolytes give an equal deionization performance. For electrolytes containing only monovalent ions, anode charge capacity is limiting, and for electrolytes containing bivalent ions, cathode charge capacity is limiting.

The obtained performance relations result in a good understanding of the entire CDI process, which was translated into a mathematical model in **chapter 8**. This was done by coupling the obtained performance relations to a mass and charge transport model. This model takes as an input the construction of a certain CDI unit, the characteristics of the influent and the mode of operation of the CDI unit. CDI deionization and regeneration behavior closely matched experimental data, for both MCDI units (with ion-exchange membranes) as well as for CDI units (without membranes). The difference between model and data can be related to mass transport limitation resulting from system design and membrane characteristics.

In **chapter 9** a general discussion is given on the approach as followed in this thesis. This includes the unique properties of the power law transmission line model as developed in chapter 2, which is suspected to be caused by the cylindrical structure of the carbon fibers. Furthermore, the origin of the charge-transfer resistance as determined in chapters 4 and 5 is discussed, which is caused by the resistance encountered when electrons are transferred between current collector and carbon electrode. A final discussion point is why the deionization efficiency is never higher than 75 %, as found in chapters 6 and 7. This is most likely caused by dead pockets in the system where

no deionization takes place, or by surface functional groups that generate capacity but do not act in the deionization, so-called pseudocapacitance.

The conclusion of this thesis is that the developed approach of linking electrochemical characteristics to deionization performance results in a method that can be used to characterize any element of a (M)CDI system. This element can be the current collector, electrode, spacer, but also the design of the stack. The characterization itself can be relatively fast, only a few experiments are needed to obtain a broad range of performance parameters. The obtained performance parameters are in turn independent of operational parameters such as electrolyte composition, temperature, and applied voltage. These performance parameters can in turn be used for various purposes:

- **Material selection** Materials can be screened for highest performance.
- **Performance prediction** The developed predictive model can be used to predict deionization performance for any operational condition.
- **Bottleneck identification** By comparing the model prediction to actual results, bottlenecks in the operation of the (M)CDI system can be identified and resolved.
- **System design** The obtained performance relations can be used to propose a certain system design for a certain deionization application, since the required deionization rate and deionization capacity can be linked to required stack design.

As a final note, the approach of using the parallels between (M)CDI and supercapacitors has proven to be crucial in obtaining the performance relations, where the most important parallel is clearly the description of deionization in terms of electrical charge instead of ions.

Samenvatting

Capacitieve Deionisatie (CDI) is een ontzoutingtechnologie gebaseerd op de tijdelijke opslag van ionen op een elektrisch geladen oppervlak. **Hoofdstuk 1** behandeld de geschiedenis van CDI, en de voordelen van CDI over bestaande ontzoutingtechnologieën zoals elektrodialyse en omgekeerde osmose. De voordelen van CDI zijn vooral duidelijk bij de ontzouting van brak water, omdat in deze toepassing CDI het laagste energieverbruik toont ten opzichte van concurrerende ontzoutingtechnologieën. Andere voordelen van CDI zijn de lage kans op vervuiling door kalkaanslag en een hoge water efficiëntie.

Om de toepassingen van CDI in beeld te brengen is het van belang te achterhalen hoe de prestatievan CDI te relateren is aan het ontwerp. Het doel van dit proefschrift is dan ook om de prestatie van een CDI systeem te relateren aan het ontwerp van dit systeem en de specificaties van het te behandelen water (het elektrolyt). Deze relatie kan dan gebruikt worden om prestatieparameters te definiëren voor elk van de elementen in een CDI systeem. Deze prestatieparameters kunnen gebruikt worden om een CDI systeem te optimaliseren voor een specifieke toepassing.

De gebruikte aanpak om tot prestatieparameters te komen, wordt tot stand gebracht door te concentreren op ladingstransport en dit ladingstransport te koppelen aan ontzouting. Door te concentreren op ladingstransport kan een CDI systeem gezien worden als een supercapacitor. Een supercapacitor is een type condensator welke elektrische lading en energie kan opslaan door adsorptie van ionen op een elektrisch geladen oppervlak. Omdat prestatierelaties voor supercapacitors bekend zijn, kunnen deze gebruikt worden als uitgangspunt om prestatieparameters voor CDI systemen op te zetten.

Voordat prestatieparameters kunnen worden achterhaald, moet er eerst een methode bestaan om CDI systemen te karakteriseren. In **hoofdstuk 2** worden elektrochemische methoden geïnventariseerd om CDI systemen te kunnen karakteriseren. Twee elektrochemische karakterisatiemethoden zijn hieruit geselecteerd; elektrochemische impedantie spectroscopie (EIS) en cyclische chronopotentiometrie. Deze methoden zijn toegepast op een CDI systeem, bestaande uit twee elektroden ingeklemd tussen stroomontvangers en gescheiden door een poreuze afstandhouder. Drie verschillende elektrode typen zijn getest, elektroden gemaakt van koolstof poeders, koolstof vezels en van koolstof aerogel.

Uit de karakterisatie kan geconcludeerd worden dat EIS het meest geschikt is om CDI systemen te karakteriseren. Uit deze karakterisatie kunnen de capaciteit en weerstandsdistributie van de koolstof elektroden worden gehaald en ook de lading-

overdrachtsweerstand tussen koolstof elektrode en stroom ontvanger en de systeemweerstand. De systeemweerstand bestaat uit contactweerstanden plus de weerstand van de poreuze afstandhouder. Deze elektrochemische karakteristieken kunnen direct gerelateerd worden aan ontzoutingskarakteristieken. Capaciteit is gerelateerd aan de hoeveelheid ionen die kunnen worden geadsorbeerd en weerstand relateert aan de snelheid waarmee ionen kunnen worden geadsorbeerd.

De transport- en adsorptiedynamiek van ionen in de poreuze koolstof elektroden is bepaald door de distributie van capaciteit en weerstand in deze koolstof elektroden. Voor elektroden gemaakt van koolstof poeder is deze distributie homogeen, terwijl voor elektroden gemaakt van koolstof aerogel kan de distributie beschreven worden door een constante fase hoek model. Voor elektroden gemaakt van koolstof vezels moest een nieuw model gemaakt worden om de transport- en adsorptiedynamiek te kunnen beschrijven. Dit nieuwe model is gebaseerd op een machtsverband tussen capaciteit en weerstand in de koolstof elektrode. Dit model is succesvol toegepast om het ion transport in koolstof vezel elektroden te modelleren. De resultaten van de EIS karakterisatie konden geverifieerd worden door cyclische chronopotentiometrie toe te passen, welke dezelfde resultaten opleverde voor totale capaciteit en totale weerstand van het CDI systeem.

De verkregen elektrochemische karakteristieken zijn alleen geldig onder de condities waarbij de experimenten uitgevoerd zijn. Om onafhankelijke prestatierelaties te verkrijgen zijn in hoofdstukken 3 en 4 de relatie tussen de elektrochemische karakteristieken en operationele parameters onderzocht. De operationele parameters waren de temperatuur en concentratie van het gebruikte elektrolyt en het gebruikte voltage. De gevonden relatie kan gebruikt worden om prestatieparameters te definiëren die onafhankelijk zijn van de operationele parameters.

In **hoofdstuk 3** is de relatie tussen elektrodecapaciteit en de operationele parameters onderzocht. De theoretische relatie tussen de elektrodecapaciteit en de operationele parameters is gedefinieerd door een dubbellaag model, welke de opslag van lading op oppervlakken beschrijft. Het Gouy-Chapman-Stern dubbellaag model is gekozen als het meest geschikte model om deze relatie te beschrijven voor CDI systemen; dit model is complex genoeg om alle variaties in operationele parameters te beschrijven en eenvoudig genoeg doordat het model maar twee onbekende parameters heeft. Deze twee onbekende parameters zijn de capaciteit van de Helmholtz laag, welke de dubbellaag capaciteit beschrijft dichtbij het elektrodeoppervlak en de temperatuurafhankelijkheid van deze capaciteit. Door het model te relateren aan experimentele data kan het dubbellaagoppervlak per gewicht van de gebruikte elektrode worden bepaald. Dit oppervlak is een onafhankelijke prestatieparameter voor de elektrische capaciteit

van de koolstof elektroden. De gevonden resultaten laten zien dat het dubbellaagmodel een precieze voorspelling kan geven van de capaciteit van CDI elektroden. Verder is de gevonden waarde voor de Helmholtz laag capaciteit soortgelijk aan waarden zoals gevonden in de literatuur en de temperatuurafhankelijkheid van deze capaciteit is soortgelijk aan de temperatuurafhankelijkheid van de diffuse dubbellaag capaciteit.

In **hoofdstuk 4** is de relatie tussen weerstand en de operationele parameters onderzocht. De onderzochte weerstanden zijn systeemweerstand, ladingsoverdrachtweerstand en elektrodeweerstand.

De systeemweerstand is de weerstand van de poreuze afstandhouder plus de contactweerstand tussen stroombron en de stroom ontvangers. De weerstand van de poreuze afstandhouder is lineair gerelateerd aan de absolute weerstand van het elektrolyt. Deze relatie resulteert in de definitie van een prestatieparameter welke gelijk is aan de effectieve dikte van de poreuze afstandhouder. De effectieve dikte is altijd groter dan de gemeten dikte van de poreuze afstandhouder.

Elektrodeweerstand is de ondervonden weerstand wanneer ionen in een poreuze elektrode penetreren. Deze weerstand is proportioneel gerelateerd aan de absolute weerstand van het elektrolyt. Deze relatie is experimenteel bevestigd en resulteert in de definitie van een prestatieparameter welke gelijk is aan de penetratiediepte van ionen in een poreuze elektrode. Deze penetratiediepte is in dezelfde orde als de dikte van de elektrode.

Ladingsoverdrachtweerstand is de weerstand ondervonden wanneer elektronen worden overgedragen van de stroomontvanger naar de koolstof elektrode. Het is niet geheel duidelijk wat de precieze theoretische basis voor dit proces is. De consensus is dat het proces een ladingsoverdrachtproces is, en daardoor moet het proces een Arrheniusachtige temperatuurrelatie volgen. Dit is geverifieerd in de experimenten. Echter, het exacte proces dat verantwoordelijk is voor de ladingsoverdracht kon niet worden achterhaald. Daardoor is gekozen voor een empirische beschrijving van de relatie tussen de operationele parameters en de ladingsoverdrachtweerstand. Deze beschrijving resulteert in de definitie van een empirische prestatieparameter welke relateert aan de snelheid van ladingsoverdracht tussen de stroomontvanger en de koolstof elektrode.

Hoofdstukken 3 en 4 vormen een theoretisch kader welke gebruikt kan worden om verschillende elektroden, afstandshouders, stroom ontvangers en systeemontwerpen te testen, aangezien elke prestatieparameter aan een van deze elementen te relateren is. De prestatieparameter voor elektroden wordt verder uitgewerkt in hoofdstuk 5, aangezien de elektroden het belangrijkste element zijn in de bepaling van de prestatie van een CDI systeem.

In **hoofdstuk 5** is het effect van elektrodeopbouw op elektrodeprestatie onderzocht. Dit is gedaan door verschillende elektrodematerialen te onderzoeken, bestaande uit een brede selectie van verschillende koolstof vezels en koolstof poeders, afkomstig van verschillende producenten en met verschillende oppervlakte karakteristieken. Van elk elektrodemateriaal zijn oppervlakte metingen gedaan om oppervlakte karakteristieken te bepalen. Om van koolstof poeder elektroden te maken is een nieuw elektrodeproductieproces ontwikkeld. Hierbij wordt het koolstof poeder gemengd met een polyvinylidenefluoride (PVDF) oplossing in n-methylpyrrolidone (NMP). Door dit mengsel uit te strijken over een glasplaat en het NMP uit te wassen met water, kan een elektrode met een zeer consistente opbouw gemaakt worden.

Alle elektroden zijn getest aan de hand van de procedure zoals beschreven in hoofdstuk 2 en door gebruik te maken van de prestatierelaties in hoofdstuk 3 en 4 konden prestatieparameters bepaald worden. Door deze prestatieparameters te relateren aan de oppervlaktekarakteristieken van de gebruikte koolstoffen, kunnen zeer specifieke prestatierelaties bepaald worden. Deze relaties laten zien dat de meeste dubbellaagcapacteit gegenereerd wordt in de microporiën en in de kleine mesoporiën. Verder is de snelheid van ladingoverdracht van het elektrische contactoppervlak van een elektrode proportioneel gerelateerd aan het specifieke porieoppervlak van de gebruikte koolstof, een hogere specifieke porieoppervlak zorgt voor een snellere ladingoverdracht. De weerstand van de elektrode blijkt gelimiteerd te worden door de migratie van ionen in de koolstofdeeltjes en bepaald door de massa koolstof per oppervlakte eenheid elektrodeoppervlak. Dit resulteerde in de definitie van de specifieke penetratiediepte van ionen in de koolstof, welke gelijk is voor alle onderzochte koolstoffen.

Hoofdstukken 2 tot en met 5 bespreken prestaties alleen in termen van lading. In **hoofdstuk 6** is de relatie onderzocht tussen prestaties (elektrochemische prestaties) in termen van lading en prestaties in termen van ionen (ontzoutings prestaties).

De theoretische relatie tussen ladingopbouw en ionverwijdering is gedefineerd in de constante van Faraday, één mol lading is nodig om één mol monovalent binair zout te adsorberen. Twee processen kunnen deze relatie verstoren. Het eerste proces is het verlies van lading door elektrochemische reacties aan het oppervlakte van de elektroden. Dit proces is gedefinieerd als de Coulombische efficiëntie, ofwel de fractie aangebrachte lading die daadwerkelijk wordt opgeslagen op de elektroden. Het tweede proces is het verlies aan ionverwijdering doordat tijdens oplading van de elektroden ionen worden afgestoten uit de elektrode. Deze uitstoot van ionen doet een deel van de ion adsorptie teniet. Dit proces is gedefineerd als de ontzoutingefficiëntie, ofwel de fractie opgeslagen lading die daadwerkelijk gebruikt wordt om ionen vanuit het elektrolyt te verwijderen.

Twee CDI configuraties zijn gebruikt om deze twee efficiëntieparameters te onderzoeken, een "standaard" CDI systeem, bestaande uit koolstof elektroden gescheiden door een poreuze maar elektrisch isolerende afstandhouder en een configuratie waarbij tussen de poreuze afstandhouder en de koolstof elektroden ion-selectieve membranen zijn geplaatst. Deze laatste configuratie wordt Membraan Capacitieve Deionisatie (MCDI) genoemd.

Uit de experimenten blijkt dat elektrochemische reacties plaatsvinden op het oppervlak van de elektroden, vooral bij voltages hoger dan 1.2 V. Bij hogere voltages wordt tot 10 % van de aangebrachte stroom verloren aan deze ongewenste elektrochemische reacties, resulterend in een Coulombische efficiëntie van 90 %. Deze reacties kunnen verminderd worden door toepassing van ion-selectieve membranen. Hierbij is de Coulombische efficiëntie relatief constant op 95 %, ook bij voltages hoger dan 1.2 V. Verder blijkt dat tijdens oplading van de elektroden daadwerkelijk ionen worden afgestoten uit de elektrode; vooral bij lagere voltages wordt maar 40 % van de opgeslagen lading daadwerkelijk gebruikt om ionen vanuit het elektrolyt te verwijderen. Bij gebruik van ion-selectieve membranen is deze ontzouting efficiëntie veel hoger; voor alle voltages is deze 75 %.

De toename in efficiëntieparameters bij gebruikmaking van ion-selectieve membranen in een MCDI systeem zorgen voor een toename in ontzoutingsnelheid van 25 % ten opzichte van een "standaard" CDI systeem. Verder geeft een MCDI systeem een factor 10 hogere ontzoutingsnelheid, een 36 % hogere adsorptiecapaciteit en een verhoogde Coulombische efficiëntie ten opzichte van state-of-the-art koolstof aerogel CDI systemen.

De laatste prestatierelatie is die tussen de verschillende typen ionen waaruit het elektrolyt opgebouwd kan zijn. Dit is onderzocht in **hoofdstuk 7**, waarbij ontzoutingsprestaties zijn bepaald voor verschillende types elektrolyten. Deze ontzoutingsprestaties zijn daarna vergeleken met de ontzoutingsprestaties voor een natrium chloride elektrolyt, welke het gebruikte elektrolyt is in alle overige hoofdstukken. Hieruit blijkt dat wanneer rekening wordt gehouden met de valentie en de specifieke geleidbaarheid van de verschillende elektrolyten, de meeste elektrolyten vrijwel dezelfde ontzoutingsprestatie geven. Als het elektrolyt volledig uit monovalente ionen bestaat, is de adsorptie van anionen limiterend voor de totale capaciteit. Als het elektrolyt bestaat uit een combinate van een bivalent ion en twee monovalente tegenionen, of uit twee bivalente ionen, is de adsorptie van cationen limiterend voor de totale capaciteit.

De behaalde prestatierelaties resulteren in een goed begrip van het gehele CDI proces, wat vertaald is in een mathematisch model in **hoofdstuk 8**. Dit is gedaan door

de behaalde prestatierelaties te koppelen aan een massa- en ladingstransportmodel. Dit model neemt als input de constructie van een bepaald CDI systeem, de samenstelling van het influent en de wijze hoe de CDI unit wordt geopereerd. Na vergelijking van het model met experimentele waarnemingen blijkt dat het model goed in staat is om ontzoutingskarakteristieken te modelleren, zowel voor CDI systemen (zonder ion-selectieve membranen) als voor MCDI systemen (met ion-selectieve membranen). Het verschil tussen experimentele data en modelvoorspelling kan gerelateerd worden aan massa transport limitatie. Deze limitatie wordt veroorzaakt door systeemontwerp en membraankarakteristieken.

Als laatste wordt in **hoofdstuk 9** een algemene discussie gegeven over de aanpak zoals gevolgd in dit proefschrift. Verder worden de unieke eigenschappen van de machtsverband transmissie lijn model besproken, zoals ontwikkeld in hoofdstuk 2. Deze eigenschappen worden waarschijnlijk veroorzaakt door de cilindrische vorm van de koolstof vezels. Ook wordt de ladingsoverdrachtweerstand zoals gevonden in hoofdstukken 4 en 5 besproken. Deze ladingsoverdrachtweerstand wordt hoogstwaarschijnlijk veroorzaakt door elektronen die het grensvlak tussen koolstof elektrode en stroom ontvanger moeten passeren. Een laatste discussiepunt is het feit dat de gevonden ontzoutingefficientie nooit hoger is dan 75 %. Dit wordt hoogstwaarschijnlijk veroorzaakt door een dode zone in het systeem waar geen ontzouting plaatsvindt, of door oppervlaktegroepen welke wel capaciteit genereren, maar niet meedoen in de ontzouting, zogenaamde pseudo-capaciteit.

De conclusie van dit proefschrift is dat de ontwikkelde aanpak van het koppelen van elektrochemische eigenschappen aan ontzoutingsprestatie resulteert in een methode die gebruikt kan worden om elk element in een (M)CDI systeem te karakteriseren. Dit element kan een stroom ontvanger zijn, elektrode, afstandhouder, maar ook het ontwerp van een systeem. De karakterisatie zelf kan relatief snel gebeuren, er zijn maar enkele experimenten nodig om een grote hoeveelheid prestatieparameters te achterhalen. De behaalde prestatieparameters zijn onafhankelijk van operationele parameters zoals elektrolyt samenstelling, temperatuur en toegepast voltage. Deze prestatieparameters kunnen verder gebruikt worden voor verschillende toepassingen:

- **Materiaal selectie** Materialen kunnen geselecteerd worden op de beste prestaties
- **Ontzoutingvoorspelling** Het ontwikkelde ontzoutingsmodel kan gebruikt worden om te voorspellen in hoeverre een bepaald CDI systeem een bepaald water zal ontzouten
- **Knelpunt identificatie** Door de voorspellingen van het ontzoutingsmodel te

vergelijken met ontzoutingsresultaten kunnen knelpunten in het (M)CDI systeem worden opgespoord en verholpen

- **Systeem ontwerp** De gevonden prestatierelaties kunnen gebruikt worden om bij een bepaald ontzoutingsvraagstuk een bepaald systeem te adviseren, aangezien de benodigde ontzoutingssnelheid en ontzoutingscapaciteit kunnen worden gerelateerd aan het systeemontwerp.

Als laatste kan gezegd worden dat in de gebruikte aanpak de parallelen tussen (M)CDI en supercapacitors cruciaal zijn geweest in het verkrijgen van prestatierelaties, waarbij het beschrijven van ontzouting in termen van elektrische lading in plaats van in termen van ionen de belangrijkste parallel is geweest.

Acknowledgements / dankwoord

Het proefschrift wat nu voor je ligt is niet alleen een samenvatting van 4 jaar onderzoek, het is het ook het sluitstuk op een ontzettend leuke tijd in Friesland. Dit is vooral te danken aan jou Cathrina, onze trouwerij en de geboorte van onze dochter Susan behoren tot de mooiste momenten. Ook jouw steun in de afgelopen twee jaar heeft veel voor me betekend, ik heb me flink vergist in de tijd die het kost om "even" een proefschrift af te maken.

Voor de inhoud van het proefschrift heb ik veel te danken aan mijn begeleiding vanuit Wageningen. Harry, bedankt dat je me hebt laten zien dat elegante algebra en statistiek te verkiezen zijn boven "brute force" numerieke methoden, en bedankt voor je constante overtuiging dat de gevolgde aanpak de juiste is. Wim, ook al heb je als mijn professor wat meer aan de zijlijn gestaan, heb ik veel geleerd van je commentaar op mijn hoofdstukken. Verder ben ik voor de inhoud van dit proefschrift dank verschuldigd aan verschillende mensen vanuit Wetsus. Sybrand, we zijn het niet altijd eens geweest in de afgelopen jaren, maar je input in verschillende hoofdstukken is zeer zeker gewaardeerd. Michel, bedankt voor je hulp op het begrijpen en beschrijven van alle elektrochemische processen. Maarten, bedankt voor je input rond de beschrijving van de dubbellaag, en natuurlijk voor de (soms enigzins verhitte) discussies rond het mechanisme van Capacitieve Deionisatie.

De basis voor dit proefschrift zijn vele honderden experimenten. Deze zijn vooral gedaan door studenten. Wieger, Melanie, Julien, Ivo, Romain and Arjan, thanks for helping me out with conducting these experiments, and for being part of the "Carbon Team"!

Voor het uitvoeren van de experimenten heb ik veel hulp gehad van het labteam van Wetsus. Harry, Wim en Harm, bedankt voor het upgraden van mijn houtjetouwtje knutselwerkjes naar volwaardige setups. Janneke, Arie en Jelmer, bedankt voor de hulp met de analyses en de SEM-foto's. Nogmaals excuses voor alle zwarte vegen op de apparatuur. Verder natuurlijk mijn dank aan iedereen binnen de vakgroep Milietechologie in Wageningen, ik kwam dan wel niet zo vaak langs, maar ik heb altijd het gevoel gehad dat ik er toch wel bij hoorde.

Natuurlijk is er behalve hard gewerkt ook veel lol gemaakt, wat denk ik vooral komt door het unieke karakter van Wetsus. Cees en Johannes, jullie idee van een breed opgezet water onderzoeks omgeving is, behalve dat er vernieuwend onderzoek gedaan wordt, ook een uniek sociaal experiment. Verschillende mensen van verschillend pluimage komen bijeen, bemoeien zich met alles en iedereen, en proberen een stempel te drukken op Wetsus. Ik heb genoten van alle discussies rond pre-conventional water treatment en waterbruggen (Cees Kamp / Elmar / Maarten), de aanschaf van Mat-

lab, high speed camera's en Raman lasers (Bob / Kamuran / Luewton / Gert-Jan / Elmar), stemrecht voor de AIO (Paula / Natasja / MT meetings), het nut van modelleren (Sybrand / Ingo), en zo kan ik nog wel even door gaan.

Dit sociale experiment zette zich ook voort buiten kantooruren, op dinsdagavond de Pubquiz, op donderdag Irish Pub, en vaak in het weekend wel ergens een feestje. Bedankt Perry, Loes, Tom, Marthe, Kamuran, Hellen, Philipp, Tim, Petra, Aleid, Urania, Lucía, en natuurlijk alle andere Wetsians. Maxime, thanks for all the discussions on (Irish) beer, the meaning of (PhD) life, photography and Spiderpig. Ingo, thanks for being a fellow nerd, being my paranymph and coping with my not-so-funny jokes about Germans. Paula, bedankt dat je mijn paranimf bent, voor de gedeelde inzichten op het sociale experiment Wetsus, en voor het zijn van een goede buur.

Een ander onderdeel van het unieke karakter van Wetsus is ook de intensieve interactie met bedrijven welke onderdeel zijn van het "thema team". Ik wil alle partners van het thema "zout" bedanken voor de discussies tijdens de vele thema team bijeenkomsten, met in het bijzonder Bert van der Wal en Hank Reinhoudt van Voltea. Bert: vooral jouw kritische commentaar heeft me geholpen om de interpretaties van de resultaten helder te krijgen.

Het onderzoek naar Capacitieve Deionisatie stopt niet met dit proefschrift. Dankzij werk binnen Wetsus door Philipp, Bruno, Maarten, Ran en Slawomir worden vele nieuwe invalshoeken op Capacitieve Deionisatie geopend. Verder wil ik Voltea bedanken voor mij de kans te bieden om het werk dat ik binnen Wetsus gedaan heb nu verder te kunnen zetten in een commerciële setting. Piotr, my eternal research neighbor: thanks for joining me at Voltea.

Als laatste wil ik iedereen bedanken (vooral ons moeder) die in de afgelopen tijd me gevraagd heeft wanneer dat dat proefschrift nu eens eindelijk af komt. Het antwoord op deze vraag ligt nu voor je.

About the author

Bart van Limpt was born on the 30$^{\text{th}}$ August 1979 in Eindhoven, The Netherlands. After finishing secondary education at the Pius X College in Bladel, he started his Bachelor education Environmental Sciences at the Hogeschool Brabant in Etten-Leur, where he did two traineeships on environmental fate modeling, one at CSIR in Pretoria, South Africa, and one at Arcadis Heidemij Realisatie. After obtaining his Bachelor degree in 2000 he started his Master education Environmental Technology at the University of Wageningen, where he did his Master thesis on process modeling of zinc sulfide precipitation under supervision of prof. dr. Piet Lens. After obtaining his Master degree in 2004 he started his PhD project at the Sub-department Environmental Technology of Wageningen University, stationed at Wetsus, Centre of Excellence for Sustainable Water Technology, in Leeuwarden. Since January 2009 he works at Voltea as manager R&D to further develop Capacitive Deionization for commercial use.

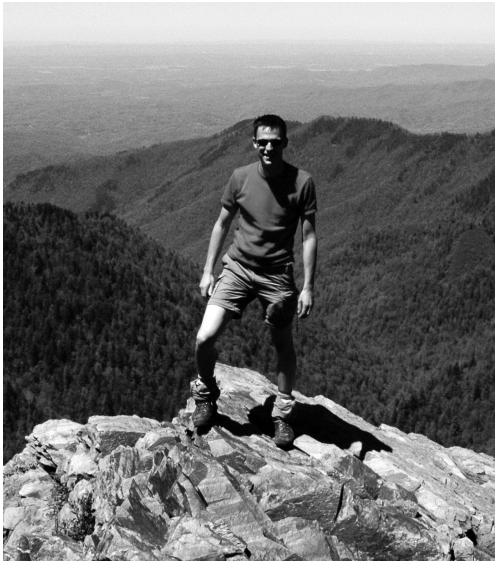

Netherlands Research School for the
Socio-Economic and Natural Sciences of the Environment

C E R T I F I C A T E

The Netherlands Research School for the
Socio-Economic and Natural Sciences of the Environment
(SENSE), declares that

Bart van Limpt

born on 30 August 1979 in Eindhoven, The Netherlands

has successfully fulfilled all requirements of the
Educational Programme of SENSE.

Leeuwarden, 2 November 2010

the Chairman of the SENSE board

Prof. dr. Rik Leemans

the SENSE Director of Education

Dr. Ad van Dommelen

The SENSE Research School has been accredited by the Royal Netherlands Academy of Arts and Sciences (KNAW)

KONINKLIJKE NEDERLANDSE
AKADEMIE VAN WETENSCHAPPEN

The SENSE Research School declares that **Mr. Bart van Limpt** has successfully fulfilled all requirements of the Educational PhD Programme of SENSE with a work load of 30 ECTS, including the following activities:

SENSE PhD courses

- Environmental Research in Context
- Research Context Activity: Co-organizing Wetsus Water Challenge (Leeuwarden, 21-22 June 2007)
- Physical modelling
- Basic and Advanced statistics

Other PhD and MSc courses

- Techniques for Writing and Presenting Scientific Papers
- PhD Competence assessment
- Project and Time management
- Instrumental methods in electrochemistry

Oral Presentations

- Sense symposium: Sensible water technology, 13 April 2007, Leeuwarden, The Netherlands
- Annual Netherlands Process Technology Symposium, 29 October 2007, Veldhoven, The Netherlands
- 6th ISE Spring meeting, 17 March 2008, Foz do Iguacu, Brazil
- Science cafe Eindhoven, 12 May 2009, Eindhoven, The Netherlands

SENSE Coordinator PhD Education and Research

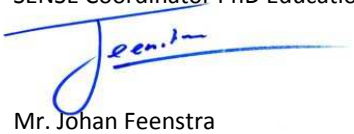

Mr. Johan Feenstra

This work was performed in the TTIW-cooperation framework of Wetsus, Centre of Excellence for Sustainable Water Technology (www.wetsus.nl). Wetsus is funded by the Dutch Ministry of Economic Affairs, the European Union Regional Development Fund, the Province of Fryslân, the City of Leeuwarden and the EZ/Kompas program of the "Samenwerkingsverband Noord-Nederland". Funding was also provided by the participants of the research themes "Salt" and "Capacitive Deionization".